ISSN number 0971 - 9709

IGU
Promoting Earth System Sciences

The Journal of Indian Geophysical Union

A SCI Journal

Impact Factor (2025) 0.2

AN OPEN ACCESS BIMONTHLY JOURNAL OF IGU

VOLUME 30, ISSUE 2, MAR. 2026

The Journal of Indian Geophysical Union (JIGU)
Editorial Board

Chief Editor
O.P. Pandey (Geosciences), Hyderabad

Associate Editors
N. V. Chalapathi Rao (Geological Sciences), Thiruvananthapuram
D. Srinivasa Sarma (Geology, Geochemistry), Hyderabad
D. Shashidhar (Seismology), Hyderabad
S. P. Sharma (Exploration Geophysics), Kharagpur
P.S. Sunil (Seismology, Marine sciences), Kochi
Anand K. Pandey (Himalayan geology, Geodynamics) , Hyderabad

Editorial Board
Solid Earth Geosciences:
Zhigang Peng (Seismology, Remote sensing), Atlanta, USA
Maurizio Fedi (Geodesy, Geophysics), Naples, Italy
Jiancang Zhuan (Statistical modelling, Seismicity), Tokyo, Japan
Ravi P. Srivastava (Exploratioin Geophysics), Bergen, Norway
Kalachand Sain (Seismic, Seismology, Gas hydrate), Hyderabad
Muppidi. Ravi Kumar (Potential field), Hyderabad
Priyeshu Srivastava (Magnetism, Geochemistry), Mumbai
Bhaskar Kundu (Tectonic geodesy), Rourkela
Satish Maurya (Seismology), Mumbai
K. Madhusudhana Rao (Seismology), Gandhinagar
Praful K. Singh (Hydrogeology, Geospatial technology), Gaya
Priyadarshi Chinmoy Kumar (Machine Learning, Hydrocarbon), Dehradun
S. Lasitha (Seismotectonics, Geology), Pondicherry
Bikram Bali (Tectonics, Geology), Srinagar
Dhruv Sen Singh (Sedimentology, Quat. Geology), Lucknow
Himanshu Mittal (Seismology), New Delhi
P.V. Nagmani (Ocean sciences), Hyderabad
Abhishek Saha (Geology, Oceanography), Goa
Abhishek Kumar Rai (Hydrogeology, Geothermal), Kharagpur
Labani Ray (Geothermal), Hyderabad
Saurabh Dutta Gupta (Seismic, Hydrocarbon), Dhanbad

Marine Geosciences and Atmospheric and Space Sciences:
Jayashree Bulusu (Space sciences), Mumbai
B. V. Laxmi (Paleomagnetism), Mumbai
R. Bhatla (Meteorology), Varanasi
Monika J. Kulshrestha (Atmospheric Sciences), New Delhi
Firoz Kadar Badesab (Marine Geophysics), Goa
P. Mahesh (Seismology, Ocean Science), Goa
Rahul Mohan (Ocean science), Goa
R. S. Mahendra (Geoinformatics, Oceanography), Hyderabad
D. Rajan (Atmospheric Science, Monsoon), Coimbatore

Managing Editor:
ASSSRS Prasad (Exploration Geophysics), Hyderabad

Indian Geophysical Union (IGU)
Executive Council

President
Dr.M. Ravichandran, Secretary,
Ministry of Earth Sciences, New Delhi

Vice Presidents
Dr.Prakash Kumar, Director, CSIR-NGRI, Hyderabad
Dr.A.P. Dimri, Director, IIG, Mumbai
Ms. Sushma Rawat, Director (Exploration)-(Retd), ONGC, New Delhi
Dr. T. Srinivas Kumar, Hyderabad

Honorary Secretary
Dr. Abhey Ram Bansal, CSIR-NGRI, Hyderabad

Joint Secretary
Prof. M Radhakrishna, IITM, Mumbai

Org. Secretary
Dr. ASSSRS Prasad, CSIR-NGRI(Retd.), Hyderabad

Treasurer
Mr. Md. Rafique Attar, CSIR-NGRI, Hyderabad

Executive Members
Prof. P.Rajendra Prasad, Andhra University, Vishakhapatnam
Prof. Devesh Walia, NIHU, Shillong
Prof. Rajiv Bhatla, BHU, Varanasi
Dr. Naresh Kumar, WIHG, Dehradun
Dr. A. Vasanthi, CSIR-NGRI, Hyderabad
Dr. P. S. Sunil, CUSAT, Kochi
Dr. Manisha Sandhu, Kurukshetra University, Kurukshetra
Dr. Uday Laxmi, Osmania University, Hyderabad
Prof. Y. Srinivas, MS University, Tirunelveli
Dr. Sumer Chopra, ISR, Gandhinagar
Prof. Bikram Bali, Srinagar University, Srinagar
Prof. Sanjit Kumar Pal, IIT (ISM), Dhanbad

PUBLISHED BY
Indian Geophysical Union, NGRI Campus, Uppal Road, Hyderabad- 500 007
Telephone: 91-4027012739, 27012332; Telefax:+91-04-27171564
Email: jigu1963@gmail.com, website: http://iguonline.in/journal/

The Journal with six issues in a year publishes articles covering
Solid Earth Geosciences; Marine Geosciences; and Atmospheric, Space and Planetary Sciences.

The Journal is supported by CSIR-NGRI & MoES, Govt. of India

Annual Subscription
Individual Rs -1000/- per issue and Institutional Rs- 5000/- for six issues
Payments should be sent by DD drawn in favour of "The Treasurer, Indian Geophysical Union", payable at Hyderabad,
Money Transfer/NEFT/RTGS (Inter-Bank Transfer), Treasurer, Indian Geophysical Union, State Bank of India, Habsiguda Branch,
Habsiguda, Uppal Road, Hyderabad- 500 007
A/C: 52191021424, IFSC Code: SBIN0020087, MICR Code: 500002318, SWIFT Code: SBININBBHO9.
For correspondence, please contact, Hon. Secretary, Indian Geophysical Union, NGRI Campus, Uppal Road,
Hyderabad - 500 007, India; Email: igu123@gmail.com; Ph: 040 27012332

ISSN: 0257-7968 (Clarivate Analytics)
ISSN: 0971-9709 (NISCAIR)
Approved as bimonthly ESCI journal by Clarivate Analytics
Cited in Indian Citation Index (ICI), New Delhi
Evaluated by NISCAIR, New Delhi
UGC Approved Journal

CONTENTS

Editorial

Research Articles

J. Ind. Geophys. Union, 30(2) (2026), 86-88
https://doi.org/10.71122/JIGU.30(2)2026.009

EDITORIAL

Underground energy storage in India: A geoscientific imperative for energy security and the net-zero transition

"The success of underground energy storage in India will depend on geophysicists, working alongside geologists and engineers, leading to site characterization, monitoring, and induced-seismicity risk assessment, while also shaping science-based regulatory frameworks. By developing indigenous subsurface datasets, analytical tools, and skilled manpower, the geophysical community can enable safe, scalable, and nationally self-reliant energy storage solutions."

India's pledge to achieve net-zero emissions by 2070, alongside rapidly rising energy demand and large-scale renewable integration, makes long-duration and seasonal energy storage indispensable. While electrochemical batteries and surface pumped hydro systems remain important, their scalability, duration limits, and land footprint, constrain their ability to support a deeply decarbonised energy system. In contrast, Underground Energy Storage (UES), including geological storage of hydrogen, natural gas, compressed air, and carbon dioxide, offers unparalleled capacity, duration, and strategic flexibility. Critically, UES is not a conventional infrastructure problem. It is a *geoscientific systems challenge*, requiring reliable reservoir containment over decades, cap-rock integrity under cyclic pressure, fault stability, groundwater protection, and continuous monitoring. India's geological endowment, mature sedimentary basins, extensive basalt provinces, and the abandoned mining infrastructure, could provide a strong foundation, but only if developed through rigorous geophysical science and sustained research investment.

Carbon Capture, Utilisation and Storage as India's subsurface energy architecture

The Government of India's Union Budget allocation of ₹20,000 crore over five years for Carbon Capture, Utilisation and Storage (CCUS), represents a pivotal recognition of the role of the subsurface in India's climate and energy strategy. Geological CO_2 storage underpins industrial decarbonisation, but its significance extends well beyond emissions reduction. CCUS establishes the technical, institutional, and regulatory backbone, necessary for all forms of underground energy storage. The scientific principles governing CO_2 storage in geological formations e.g., reservoir characterization, seal integrity, injection well design, pressure management, plume tracking, and long-term risk mitigation, are fundamentally the same for hydrogen, synthetic gas, or compressed air storage. National assessments indicate that India's geological CO_2 storage capacity spans across deep saline aquifers, depleted hydrocarbon reservoirs, and continental flood basalts, that would amount to several hundred million tonnes. These formations, subject to appropriate geochemical and geomechanical evaluation, can also host other energy vectors, reinforcing the need for an integrated subsurface storage framework rather than siloed projects. Moreover, CCUS deployment accelerates shared infrastructure development like pipelines, compressors, injection wells, monitoring networks, and crucially, regulatory processes for underground injection and long-term liability. International experience demonstrates that these frameworks are largely technology-agnostic and transferable across different gases. India's emerging CCUS roadmap therefore, offers a timely opportunity to mainstream underground energy storage within national energy planning.

Geological and geophysical scenario for UES in India

India's sedimentary basins contain depleted oil and gas fields and deep saline formations suitable in principle for underground energy storage. Depleted reservoirs are particularly attractive due to their proven trapping mechanisms, known pressure histories, and existing subsurface datasets. In comparison, hydrogen storage, however, introduces additional geoscientific complexity. Hydrogen's small molecular size, high diffusivity, and potential for geochemical and microbial reactions, demand exceptionally robust cap rocks, careful pressure cycling, and high-resolution fault characterization. Basin-scale studies suggest large theoretical storage potential, but safe deployment hinges on advanced subsurface imaging, rock physics analysis, reactive transport modelling and precise monitoring. Mechanical storage concepts such as, underground pumped hydro and gravity-based systems, further expand India's UES portfolio. These options reduce surface land conflicts, but rely heavily on geophysical and geotechnical assessment of rock-mass stability, seepage pathways, and long-term deformation behaviour.

Role of the Indian geophysical community

The success of underground energy storage in India would depend highly on the capabilities of the geophysical community across academia, national laboratories, industry, and professional bodies such as the *Indian Geophysical Union (IGU).* Geophysicists have a decisive role in,

(i) *Basin-scale screening and site selection*, using seismic, gravity, magnetic, and other geophysical data for integrated basin modelling to rank candidate formations.

(ii) *Reservoir, basement, overburden and seal characterization*, including assessment of heterogeneity, fracture networks, and cap-rock integrity in entire storage complex through advanced imaging techniques and rock physics.

(iii) *Monitoring, verification and risk mitigation*, employing time-lapse geophysical data, microseismicity, and surface deformation measurements.

(iv) *Induced seismicity and geomechanics*, defining safe operating pressure envelopes and informing regulatory thresholds.

(v) *Integrated modelling and uncertainty analysis*, combining geophysical, geological, geochemical, and engineering datasets.

Without sustained leadership from the geophysical community, UES projects risk being under-characterized, over-engineered, or socially contested.

Indigenous innovation: Avoiding the technology dependence trap

The ultimate impact of underground energy storage should not depend on imported solutions, but on indigenous innovations and sustained research. As Arindam Goswami has argued in his Times of India article, India's industrial ecosystem has too often prioritised *importing deep technology over building it*, stunting domestic R&D capability. A cautionary example cited was shelving of lithium-battery initiatives by a major Indian firm due to unavailable foreign technology, while a small Finland - US start up, successfully demonstrated solid-state batteries through close academia-industry collaboration and patient investment.

UES research will demand the same ingredients: *long-horizon funding, tolerance for early failure, and deep integration between universities, national laboratories, and industry*. Research on injected gas (hydrogen)-rock interactions, cap-rock integrity, multiphase flow, and monitoring technologies, etc will inevitably encounter setbacks at laboratory or pilot scale, but these must be treated as learning milestones, not failures. As Goswami notes, India must cultivate the belief that *real research can happen here, by us*.

Academia, workforce development and national partnerships

Academia should be central to building India's UES capability. Earth scientists and engineers must lead curriculum development and research programs, covering subsurface energy storage, reservoir simulation, geochemical monitoring, induced seismicity, and risk assessment. Recent Indian experience underscores this need. The NTPC-IIT Bombay CO_2 storage initiative, involving India's first CO_2 injection test well, required detailed mapping of coal-bed reservoirs, high-pressure well design, seismic monitoring, and stress-testing of the injection protocols. Experts associated with the project, emphasise indigenous technology development, careful monitoring of underground conditions, injection pressures, well integrity, and seismic response are essential for success of such a project. It is required to have a national storage atlas and structured feasibility and risk assessments, which can provide a blueprint for future UES initiatives in India. As a first step extending such collaborations by linking NTPC, GAIL, ONGC, Oil India, Coal India and other public-sector entities with universities and national laboratories, will be vital for building both technical expertise and managerial capacity in underground storage.

Regulation, governance and the role of geoscience

Regulation must evolve in parallel with technology. Clear, transparent rules for siting, permitting, monitoring, and long-term liability are essential to avoid project delays and public opposition. Experience from CCUS globally, shows that uncertainty in permitting and liability, can stall even well-designed projects. India's CCUS roadmap and emerging regulatory frameworks, should explicitly accommodate *multiple gases and storage modes.* Therefore, geoscientific survey agencies, groundwater authorities, mining regulators and other stakeholders, must be engaged early. *Geoscientists must be integral to these discussions, ensuring that geohazard risks like seismicity, aquifer connectivity, and material compatibility are addressed proactively rather than retrofitted.*

Concluding remarks

Underground energy storage is a *scientific and strategic imperative* for India's clean-energy future. It directly links climate mitigation with energy security. Realising this potential, however, requires far more than hardware deployment.

It demands sustained investment in subsurface R&D, geophysical capacity building, and regulatory frameworks grounded in Indian geology. The geophysical community has a pivotal role to play in mapping storage resources, quantifying uncertainty, monitoring performance, and shaping evidence-based regulation. By leading multidisciplinary efforts across science, industry, and policy, Indian geoscience can ensure that energy is stored where it belongs, "*underground*", and that India's energy transition is secure, resilient, and self-reliant.

Nimisha Vedanti
Chief Scientist
CSIR-National Geophysical Research Institute
Uppal Road, Hyderabad-500007, India
Email: nimisha.ngri@csir.res.in

J. Ind. Geophys. Union, 30(2) (2026), 89-101
https://doi.org/10.71122/JIGU.30(2)2026.0010

Seismic quiescence and spatio-temporal b-value variation in the Himalayan region for enhanced hazard analysis

Ashisan Dhodray and S. Lasitha*
Pondicherry University, Puducherry- 605014, India
*Corresponding author: lasitha_s@yahoo.com

ABSTRACT

This study presents an integrated spatial–temporal analysis of the Gutenberg–Richter b-value to evaluate the stress distribution and seismic potential along the Himalayan arc using earthquake catalogue spanning 1964–2025. The spatial distribution of b-values (0.5–1.2), exhibits marked heterogeneity, reflecting the complex tectonic architecture and variable stress conditions across the major thrust systems, including the Main Central Thrust (MCT), Main Boundary Thrust (MBT), and Main Frontal Thrust (MFT). Low b-values (<1.0) dominate along the MCT and MBT zones, denoting regions of elevated stress accumulation. In contrast, higher b-values (1.0–1.2) occur north of the MCT and along the MFT, representing relatively relaxed zones. A decreasing trend in b-value from west (0.8–1.0) to east (0.5–0.7), indicates increasing stress concentration in the eastern Himalaya.Temporal b-value variations reveals a cyclic pattern of seismic activity, with alternating phases of quiescence and activation. A recurring sequence of seismic quiescence, followed by a decline in b-value (Δb = 0.1–0.4), consistently precedes moderate-to-large earthquakes (Mb ≥ 6.0) signifying progressive stress build-up prior to rupture. Longer quiescent intervals (≥5 years) tend to precede major earthquakes (Mb ≥ 6.5), while shorter intervals (1–3 years) are associated with moderate events (Mb 5.7–6.1). The observed decline in b-value, following quiescent phases, may serve as a potential short-term precursor to large earthquakes offering valuable insights for seismic hazard assessment and forecasting in the Himalayan region. The increase in frequency of major earthquakes highlights a potential escalation of seismic energy release in the region.

Keywords: b-value, Spatial b-value variation, Temporal b-value variation, Seismic quiescence, Earthquake precursor, Himalayan region

INTRODUCTION

The seismicity of the Himalayan region is deeply influenced by the subduction of the Indian plate beneath the Eurasian plate and the gradual accumulation of stress along the active faults along the plate boundary. This accumulated stress is periodically released in the form of earthquakes. The devastating 2015 Gorkha earthquake, with a magnitude of 7.8 (Mw), stands as strong evidence of the seismic vulnerability of the region (Hayes and Briggs, 2017). The 2025 earthquake (M 7.1) in the Nepal-Tibet region, further highlights the persistent tectonic instability of this region.

While the convergence between the Indian and Eurasian plates is conventionally regarded as normal in the central Himalayan region, it becomes increasingly oblique towards the west relative to the structural trend and the Himalayan Frontal Thrust (HFT). The primary driver of substantial deformation within the Himalayan and Southern Tibet region is the oblique convergence (Styron et al., 2011; Murphy et al., 2014). Kundu et al. (2015) suggested the convergence velocity between India and Southern Tibet, exhibits a relatively consistent pattern, hovering at approximately 18 mm/yr along the arc. The GPS measurements showed a higher convergence rate of 18–20 ± 1 mm/yr in the eastern Himalayan region (Bilham et al., 1997; Avouac, 2003; Banerjee et al., 2008), decreasing westward to approximately 13.4 ± 5 mm/yr in western Nepal (Bettinelli et al., 2006).

The seismic hazard analysis can be approached in two ways: Deterministic Seismic Hazard Analysis (DSHA) and Probabilistic Seismic Hazard Analysis (PSHA). DSHA is a site-specific hazard analysis incorporating information about known active faults, their characteristics, and associated historical seismic events. However, PSHA takes a statistical approach to seismic hazard assessment considering a range of potential earthquake sources, magnitudes, and ground shaking intensities, providing a probability distribution of ground motion rather than a deterministic value. PSHA explicitly accounts for uncertainties associated with seismic hazard assessment, and it consider multiple seismic sources, including known faults, background seismicity, and seismicity from potential but unidentified sources. This allows for a holistic evaluation of seismic hazards, considering local and regional seismic activity.

In this study, we adopt a statistical framework to evaluate earthquake characteristics, with emphasis on the Gutenberg–Richter b-value. This approach allows us to investigate spatial and temporal variations in seismicity, analogous to how PSHA statistically models earthquake occurrence. The variation in the spatial and temporal b-value indicates the variation in the stress regime and accounts for the overall seismic hazard analysis of the study area. A lower b-value has been found to be associated with the high-stress region where the likelihood of a near-future major Earthquake, while a higher b-value seems to be associated with a lower stress regime. This study, therefore, aims to: (1) map the detailed spatio-temporal b-value variations across the central-eastern Himalayas using a comprehensive catalog from 1964-2022; (2) develop and apply a systematic, quantitative framework for identifying seismic cycles and associated quiescence phases; and (3) test the hypothesis that periods of seismic quiescence and low b-values are reliable indicators of heightened seismic hazard, using recent major

earthquakes as a validation of the proposed methodology. Figure 1 provides a visual representation of the seismic distribution of the study area, which is geographically located between 26° N- 31° N and 79° E- 92° E. The region is vulnerable due to urbanization and an increasing population in recent years, which necessitates a seismic hazard analysis to tackle and mitigate the losses caused by earthquake events.

TECTONIC SETTING OF THE STUDY AREA

The Himalayan region is a highly active and complex geotectonic zone, primarily formed due to the collision between the Indian Plate and the Eurasian Plate. This ongoing continental collision has resulted in significant crustal convergence, uplift, and the formation of the Himalayan Mountain range, which stretches across approximately 2400 kilometers. This collision has also led to the formation of several major thrust faults, which segment the region into distinct geotectonic zones (Auden and Gansser, 1967; Singh et al., 2022). The key tectonic features responsible for the dynamic geology and seismicity of the Himalayas include, the Main Central Thrust (MCT), Main Boundary Thrust (MBT), and Frontal Himalayan Thrust (HFT), as shown in Figure 2. The major structural divisions of the Himalaya include the Indus–Yarlung Tsangpo suture zone, the Tethyan Himalaya sedimentary units, the Greater Himalaya Sequence (GHS) metamorphic rocks, the Lesser Himalaya fold-and-thrust belt, and the Sub-Himalaya Siwalik molasse basin. These divisions are present along the entire length of the Himalaya (Searle et al., 2008).

The Main Central Thrust (MCT) separates the Higher Himalayan Crystalline (HHC) zone from the Lesser Himalayan (LH) domain. It plays a crucial role in the uplift and deformation of the region. The rocks in the LH are highly folded and fractured, with the MCT dipping northward at angles of about 40° to 50° (Le Fort, 1975; Valdiya, 1976, 2002). This thrust marks the boundary between younger sedimentary rocks and older metamorphic rocks, contributing to the seismic activity in the region. Most large earthquake epicenters are located along or near the MCT, highlighting its importance in Himalayan tectonics. To the south of the MCT lies the Main Boundary Thrust (MBT), which divides the Lesser Himalaya from the Sub-Himalaya (Siwalik). The MBT is responsible for much of the crustal shortening and uplift observed in the Sub-Himalaya, which consists of folded and faulted Miocene and younger sediments. These movements along the MBT continue to shape the landscape, developing low-lying hills and ridges in the southern part of the Himalayas (Thakur, 1991).

Similarly, the Himalayan Frontal Thrust (HFT) is located at the southernmost edge of the Himalayan wedge and represents the boundary between the Sub-Himalaya and the Indo-Gangetic Plains. This thrust is where the Indian plate is actively underthrusting beneath the Eurasian plate and is responsible for accommodating a large portion of the convergence between the two plates. The uplift of the Siwalik Hills and the folding of sediments along the HFT indicate the ongoing tectonic deformation in the region . Beneath all these surface thrusts lies the Main Himalayan Thrust (MHT), a gently northward-dipping fault underlying the entire Himalayan range. The MHT acts as a décollement, linking the deeper parts of the underthrusting Indian Plate with the overlying Himalayan structures. This fault accommodates much of the convergence between the Indian and Eurasian plates, driving the uplift of the mountains and the seismic activity throughout the region (Elliott et al., 2016). Large earthquakes, such as the 2015 Gorkha earthquake in Nepal, are often associated with sudden slip along the MHT, releasing strain built up over centuries. The spatial and temporal variations in seismic activity along these faults, like MCT, MBT, HFT and MHT, highlight the complexity of the geodynamic system, which continues to pose significant seismic hazards for the region.

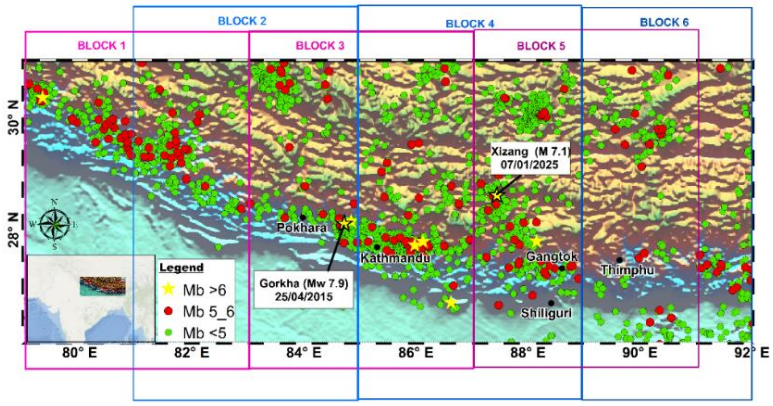

Figure 1. The seismicity map of the study area displaying earthquake distribution and epicentral blocks 1-6 considered for the present study. The yellow stars represents large earthquakes. The recent major events on April 25, 2015 and January 7, 2025 are also marked.

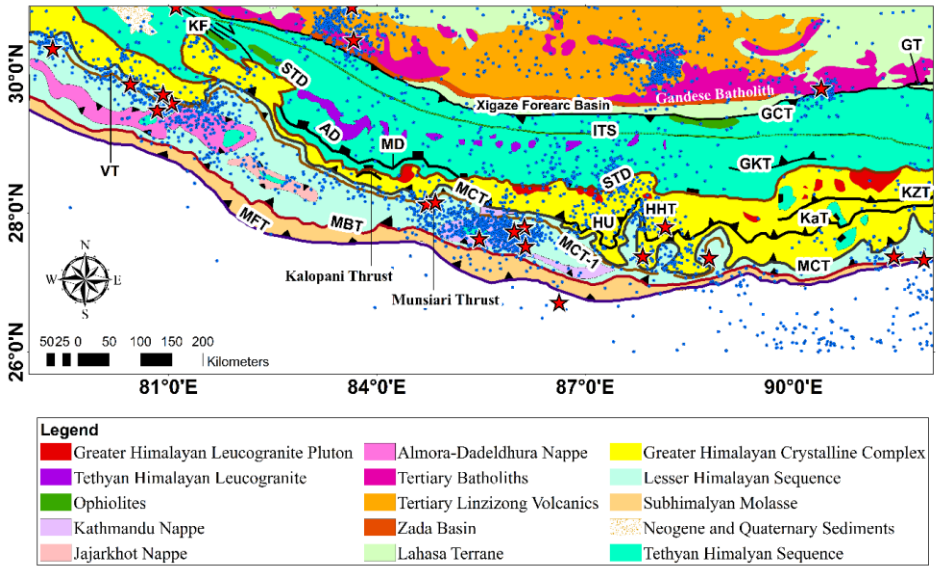

Figure 2. A tectonic map of the study area showing the major faults and the earthquake distribution. The demarcated faults included in this figure are AD= Annapurna Detachment, GCT= Great Counter Thrust, GKT= Gyirong- Kangmar Thrust, GT= Gandese Thrust, HHT= High Himal Thrust, HU = Himalayan Unconformity, ITS= Indo-Tsangpo Suture, KaT = Kakthang Thrust, KZT= Kakhtang-Zimithang Thrust, KF= Karakoram Fault (Extension), MBT= Main Boundary Thrust, MCT= Main Central Thrust, MCT-1= Extensional fault system associated with MCT, MD= Machapuchare Detachment, MFT= Main Frontal Thrust, STD= South Tibet Detachment, VT= Vaikrita Thrust. The blue dots indicates earthquakes of Mb<6, while the red stars indicate that of Mb≥6.

PREVIOUS SEISMIC HAZARD ANALYSIS ATTEMPTS

Several seminal studies, including those of Molnar and Lyon-Caent (1989) and Ambraseys and Bilham (2003) have provided crucial insights into the tectonic setting and seismic activity of the Himalayan region. The b-value, a fundamental parameter in earthquake magnitude-frequency distribution, has evolved as a key metric in seismic research (Wyss et al., 1999; Kundu et al., 2014, 2015; Chingtham et al., 2017). Researchers explored the temporal evolution of b-values, shedding light on changes in seismicity patterns over time. Additionally, Kumar and Sharma (2019) and Li et al. (2021) have delved into spatial variations, offering insights into the distribution of seismic stress along major fault lines. Scholz (1968) established its validity in laboratory experiments. Schorlemmer and Wiemer (2005) confirmed its relevance in diverse field settings, from mines to various tectonic regimes like subduction slabs, fault zones, and plutons. Kagan (1999) also emphasized this universality of b-value for earthquakes.

The spatial distribution of b-values in the Himalayan region indicates stress heterogeneity. Singh (2016) and Pudi et al. (2018) underscored the need for comprehensive catalogs to analyze seismic potential. Differential stress influences b-value, with normal faulting exhibiting high values and thrusting showing low values (Wu et al., 2018). This stress dependence of b-value, as explained by Wiemer et al. (2005) is crucial in earthquake size distribution across different stress regimes. Scholz (1968) and Smith (1981) proposed b-value as an earthquake precursor, indicating larger earthquakes in high-stress environments. Amitrano (2003) emphasized the role of confining pressure in seismicity, highlighting the brittle-ductile transition. Recently Kothyari et al. (2024) used advanced techniques to analyze surface deformation and b-value variations, offering insights into stress buildups in the Kumaon Himalayan region and the Central Himalayan region using Persistent Scatterer Interferometric Synthetic Aperture Radar (PSInSAR). Hence, the spatio-temporal variation of b-value in seismic studies plays a critical role in understanding earthquake hazards. From laboratory experiments to field studies, b-value remains a universally accepted parameter, guiding seismic risk assessment and earthquake prediction efforts.

EARTHQUAKE DATABASE

The seismic events analyzed in this research were sourced from the International Seismological Centre (ISC, 2022, https://doi.org/10.31905/D808B830). The dataset utilized in this study incorporates earthquake occurrences with the Magnitude type Mb. The study includes a total of 3162 seismic events recorded during the period spanning 1964 to 2022. The dataset is visually represented in Figure 1. To improve the reliability of hypocenters and magnitude station geometry, we applied quality control filters in accordance with standard seismological practices (Wiemer and Wyss, 1997; Wiemer et al., 2005). The network coverage of our dataset is spatially uneven, which restricts strict quality thresholds (azimuthal GAP≤ 180°, number of reporting stations (Nsta) ≥ 5, root-

mean-square residual (RMS) ≤ 1.0 s), mentioned in the studies conducted for precise epicentral location (Engdahl, 2006; Fuggi et al., 2024; Colavitti et al., 2025). By applying the threshold, the data was reduced to 912 events which is insufficient for robust statistical inference of seismic quiescence and tracking of large magnitude trends. To counter this challenge, we tested alternative thresholds of GAP ≤ 190°, ≤ 200°, and ≤ 203°. The latter threshold (GAP ≤ 203°, number of reporting stations (Nsta) ≥ 7, root-mean-square residual (RMS) ≤ 4.0 s), which proved a balanced yet well-constrained earthquake dataset. The resulting 2916 events are included in the statistical analyses for the b-value estimation and stress interpretation.The topographic data were taken from the Global Seafloor Topography dataset (Sandwell and Smith, 1997).

METHODOLOGY

Declustering

Aki (1965) and Knopoff et al. (1964) asserted that, in general, earthquake catalogs do not conform to a Poisson distribution and do not show a correlation between earthquakes. The declustering of earthquake catalogs is employed to address this deviation. This method helps distinguish independent earthquake events from dependent ones. Independent events encompass mainshocks and earthquake swarms (background), while dependent events comprise foreshocks and aftershocks. Consequently, declustering the earthquake catalog enables potential mainshocks to be treated as independent events, free from the influence of nearby foreshocks and aftershocks.

Gardner and Knopoff (1974) put forward a computationally simple method for declustering, which uses an algorithm that defines each event with a fixed time-space window depending on the magnitude. Any smaller events occurring within the window of a bigger event, the method assumes it as an aftershock/foreshock and removes it from the independent catalog. This process resulted in 1722 background and mainshock events, which include 117 isolated mainshocks, while 1077 events were classified as part of foreshock and aftershock clusters. The dataset before declustering, versus the remaining events after the declustering process, is shown in Figure 3. We used the declustered dataset that represents the mainshocks and background seismicity, which is crucial for reliable b-value estimation, as it provides a Poissonian distribution of independent events and avoids bias introduced due to temporal clustering.

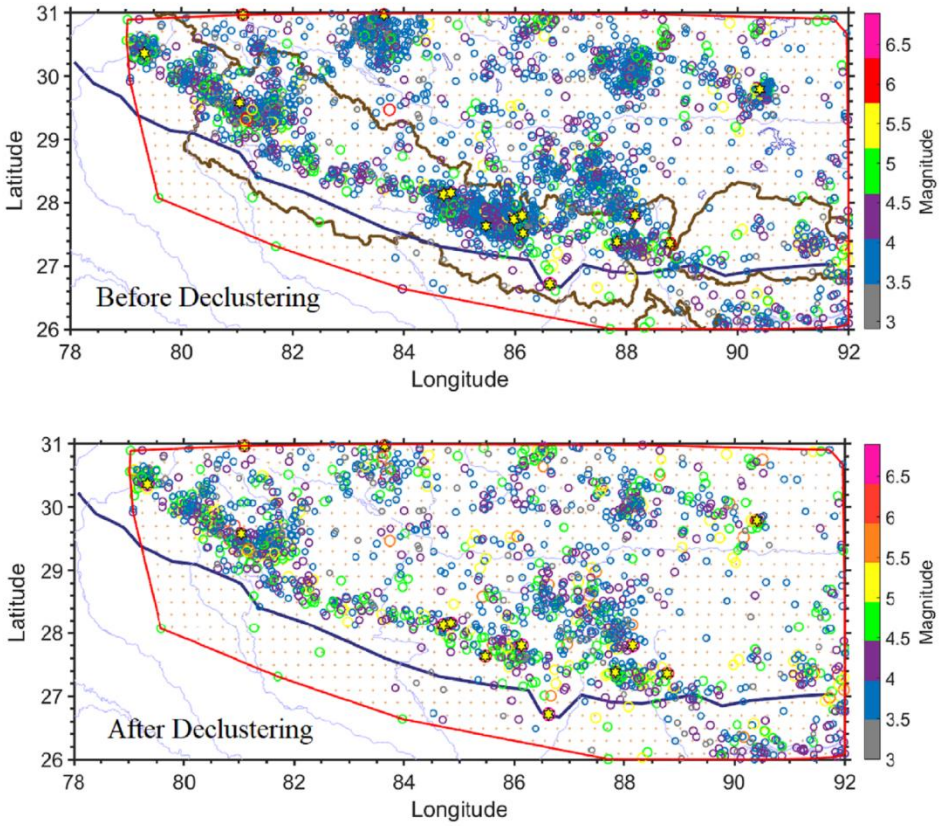

Figure 3. The earthquake events before and after the Gardner and Knopoff declustering method. The magnitude is color-coded, and the yellow star indicates large magnitude (Mb≥6) earthquakes. The 2916 events are declustered, and the 1722 remaining events is further used for b-value estimation.

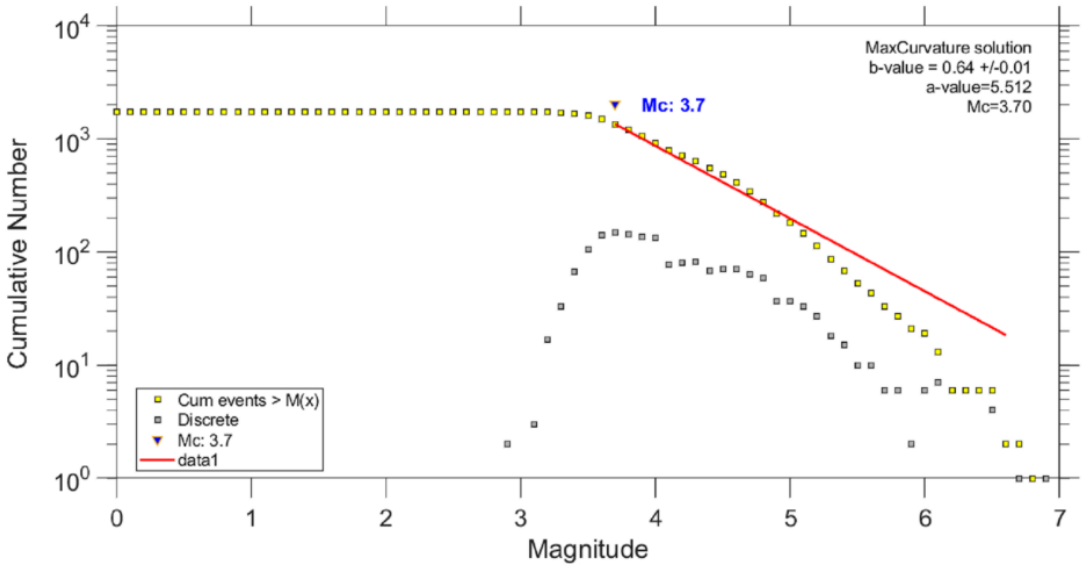

Figure 4. Frequency Magnitude Distribution (FMD) curve, where Magnitude Completeness (Mc) is denoted as 3.7.

Completeness of the catalog

Determining the magnitude of completeness (Mc) is another crucial step in seismic analysis, as it helps identify the threshold magnitude below which smaller earthquakes may not be reliably detected or recorded. The magnitude of completeness is essentially the minimum magnitude at which earthquakes can be consistently observed in a given seismic catalog (Wiemer and Wyss 1997). The necessity for calculating the magnitude of completeness lies in the fact that the accurate seismic hazard assessment depends on complete representative data.

To test the robustness of our results, we evaluated the sensitivity of the magnitude of completeness (Mc) and b-value estimates using the repeated filtering procedure with alternative gap cutoffs of 180° and 203°. The stability of Mc and b-value estimates across a subset of azimuthal gap thresholds indicates that our catalog is sufficiently complete and that the b-value variations reported in this study are robust by adopting a GAP ≤ 203°.

The ZMAP software uses different algorithms to calculate the magnitude of completeness. We employed the MaxC method to estimate Mc, as it works better with our small to moderate dataset, given that our window consideration is ≥200 events per window. The MaxC method analyzes the curvature of the frequency-magnitude distribution (FMD) curve and identifies the point of maximum curvature. The calculated Mc value for the study area is 3.7, below which the earthquake data that has not been included in further analysis. The FMD curve obtained using the MaxC method, denoting the Mc value for the declustered catalog, is shown in Figure 4.

Estimation of spatial and temporal b-value variation

The b-value indicates the relative proportion of small earthquakes over the large earthquakes. b-value is derived from the following equation,

$$\log_{10} N = a - bM$$

Though the b-value is close to 1 overall (Kagan, 1999), variation has been observed significantly. A high b-value shows a larger proportion of smaller earthquakes, whereas a low b-value depicts a larger proportion of large-magnitude earthquake events. b-value as an indicator of stress has been validated in laboratory experiments (Scholz, 1968) and the field (Schorlemmer and Wiemer 2005). The dependency of the b-value on differential stress indicated the lowering of b-value towards the end of the seismic cycle (Scholz, 1968; Smith, 1981). The earthquake grows larger in the higher stress regime (Wiemer et al., 2005).

For calculating b-value using the ZMAP tool, the relation used is of Maximum Likelihood Estimation (Aki, 1965; Utsu, 1974), which uses the following relation,

$$b = \frac{1}{\ln(10)*(M_{mean}-M_c)}$$

From the above equation, M_{mean} represents the average magnitude and M_c indicates the Magnitude of Completeness, which means the minimum threshold magnitude. The estimation of the standard deviation (δb) of b-value was obtained using the formula modified by Shi and Bolt (1982).

$$\delta b = 2.3b^2 \sqrt{\frac{\sum_i^N (M_i - M_a)^2}{n_s(n_s-1)}}$$

The M_i denote the individual magnitudes of the earthquake; M_a is the average magnitude of all the earthquakes considered; and n_s refers to the total number of earthquake samples used in the calculation.

The spatial and temporal b-value was calculated separately by dividing the study area into six epicentral blocks (Figure 1) with 50% overlapping to make it more reliable for understanding the seismic sequence over time and space. A 0.2° x 0.2° grid was selected for final b-value mapping, as it ensures independent sampling and minimizes repetitive nodes and the grid spacing provides a balance between the spatial detail and statistical reliability of the data after declustering. The spatial b-value mapping was attempted using an adaptive nearest-event approach, where we incorporated the 150 nearest earthquakes with a minimum of 50 events above Mc, calculated automatically using the Maximum Curvature (MaxC) method in each node. The correction factor of "±0.2" was applied to reduce the potential underestimate of b-value. A sensitivity test was conducted using both 100 and 150 nearest events per grid node. The 150 nearest event setup yielded more uniform node coverage and statistically robust b-values. Therefore, we have used 150 nearest events parameters for the final b-value mapping.

Seismic Quiescence

The seismic quiescence study has been adopted to understand the accuracy of temporal b-value variation, which is estimated using a time window based on the number of events (N) and maximum magnitude (Mmax) in each epicentral block. The identification of the seismic cycle phases in this study is based on the conceptual framework proposed by Scholz (1988). The major shock is usually followed by an aftershock sequence, after which a post-seismic quiescence (Q1) is observed. Q1 occupies 50-70% of the recurrence period. This is followed by an increase in background seismicity. This is again followed by the intermediate seismic quiescence (Q2), which can last for several years. The short-term quiescence (Q3) is observed several hours or a few days prior to the mainshock. The distinct quiescence phases are defined based on the deviation in the annual rate from the long-term baseline. The baseline Seismic rate (R_o) for each epicentral block was determined as the median annual earthquake occurrence over the entire study period. The post-seismic quiescence (Q1) was identified as a period after the mainshock during which the annual rate remained below the baseline seismicity for at least one year. The intermediate seismic quiescence (Q2) is identified as the period during which a significant reduction in annual seismicity, below 50% of the R_o, is sustained for two or more years, indicating stress accumulation prior to the major event. The immediate short-term quiescence (Q3) represents a sharp decline in seismicity below 25% of the R_o within the final six months prior to the mainshock, indicating temporary locking of the fault zone prior to the mainshock.

RESULTS

2,916 events from 1964 to 2022 were analyzed, and the cumulative number of events over time is illustrated in Figure 5. The graph shows the temporal distribution of earthquakes. The total number of earthquakes has shown a gradual increase through the decades, with a noticeably steeper rise after 2000. This trend may indicate either an actual increase in seismic activity or improvements in detection capabilities over time. Yellow stars in the figure denote major earthquakes (Mb ≥ 6), revealing that significant events that have occurred consistently, with a distinct clustering after 2000. The sharper slope of the cumulative curve in the post-2000 period may suggest a higher rate of seismic activity in recent years.

The study also used a histogram in addition to the cumulative rate to extract additional insights from the catalog. The analysis based on histogram was done for depth, time, magnitude, and hour (Hr). The depth histogram (Figure 6A) indicates that most earthquake events are confined to shallow depth, as the tectonic boundary is a continental collision boundary. The focal depth of the events ranges from 5 km to 105 km, with a notable concentration of events around 35–40 km, suggesting crust–mantle interaction at the slab interface. The magnitude histogram (Figure 6B) shows the number of earthquakes with magnitudes ranging from 3 to 6.9, whereas the maximum number of earthquakes falls within the magnitude 3.7-3.8 Mb for ~371 events. The mainshock magnitude ranges from 6.0 to 6.9. The time (year) histogram (Figure 6C) highlights the variation in the number of earthquakes over successive years. Prominent peaks are observed in 2008 and 2015, with the year 2015 recording about 85 events (Mb > 3.7), including the mainshock of magnitude Mb 6.9. This indicates that earthquake activity is more during 2015. The Hr histogram (Figure 6D) indicated the consistency in data acquisition throughout the day, implying that temporal biases in event recording are minimal and have a negligible effect on the dataset.

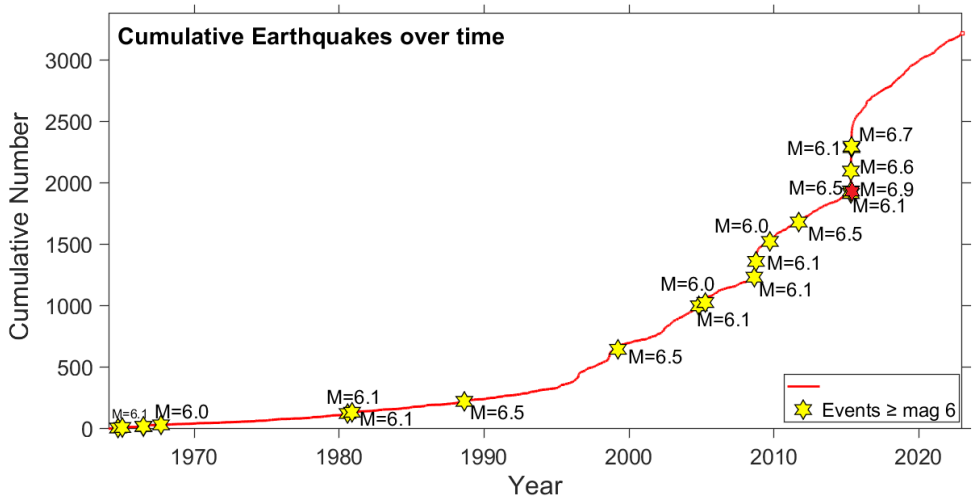

Figure 5. The cumulative event rate with respect to time. The earthquakes with a magnitude of Mb ≥ 6 have been indicated by the yellow star. The red star (Mb = 6.9) marks the major Gorkha earthquake that occurred on 25 April 2015.

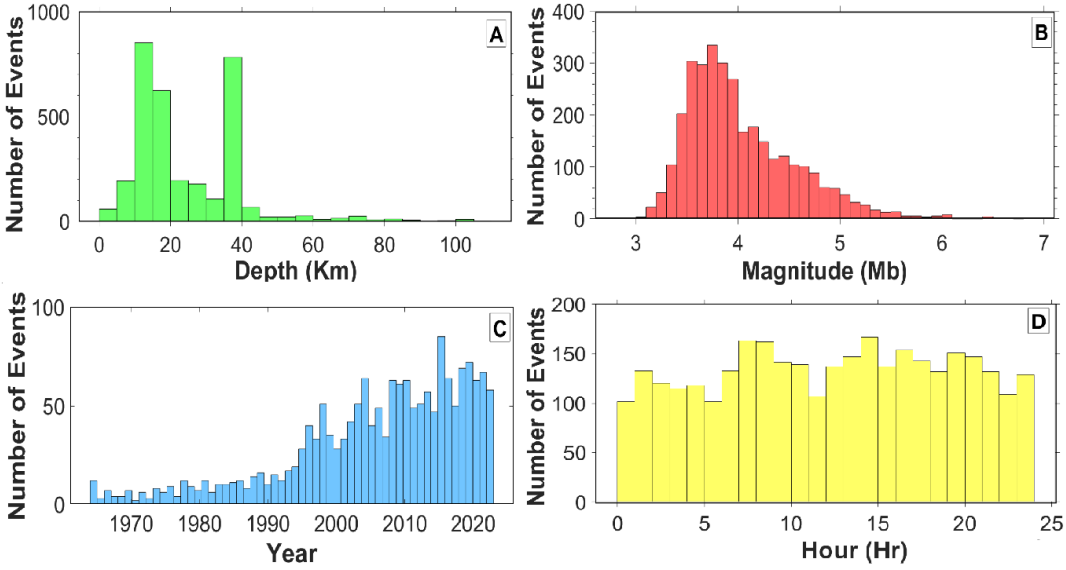

Figure 6. Statistical distribution of earthquake parameters used in the present study. **(A)** Depth distribution showing that most events are confined to shallow crustal levels (<40 km). **(B)** Magnitude distribution indicating dominance of moderate-sized earthquakes (Mb 3.0–4.5). **(C)** Temporal distribution depicting improved seismic network coverage and event detection after 1990. **(D)** Diurnal variation of seismicity shows a relatively uniform distribution across different hours of the day

Spatial variation of b-value

The study area was subdivided into 6 epicentral blocks of 4° each, with a 2° overlap between consecutive blocks (segments shown in Figure 1). The six epicentral blocks are carefully analyzed, and the b-values are estimated for the considered time window. The spatial distribution of b-value for the declustered earthquakes has been generated (Figure 7B**).** We adopted the nearest -neighbor approach with 150 events per node, minimum of 50 events above Mc, and a correction factor of '+0.2' The resulting b-value ranges from 0.5 to 1.2. The corresponding standard deviation (δb), calculated from 100 bootstrap resamples, shows that most nodes exhibit δb ≤ 0.10, confirming that the spatial b-values estimated are statistically stable and well-constrained. However, slightly higher uncertainties (δb ≥ 0.11) are observed locally in the northern and southwestern parts of the map (Figure 7C), likely due to sparse earthquake density or larger sampling radii in those regions. The spatial distribution of Mc ranges between 3.7 and 4.5 (Figure 7a), which reflects differences in both seismic network sensitivity as well as data density. The higher Mc value is observed around the regions of poorer seismic activity. The Mc map shows a relatively uniform pattern across most of the study area, which supports the reliability of the estimated b-values.

The Epicentral block 1 (Figure 1) contains a dense cluster of earthquakes, suggesting that this area is a zone of stress accumulation. The b-value in this block ranges from 0.55 to 0.9 (±0.01). Several major fault systems contribute to the seismic activity here, including the Main Central Thrust (MCT), South Tibet Detachment System (STDS), Indus-Tsangpo Suture Zone (ITSZ) and Vaikrita Thrust (VT). Most earthquakes in this area are small, with magnitudes below 5 Mb, although moderate events between 5 and 6 Mb also occur. The lower b-values observed in the western part of the block are mainly linked to faults like the MCT and STDS, where most of the larger earthquakes (>6 Mb) are observed. For epicentral block 2, the number of events increases, and the b-value drops to 0.65–0.7, suggesting higher stress accumulation. Between 83°E and 84°E, the b-value rises to 0.9–1.0, indicating a relatively quiet zone where no major earthquakes have been recorded. The seismic activity in this block is mainly controlled by the Main Central Thrust (MCT) and its extensional detachments, including the Annapurna Detachment (AD) and Machapuchare Detachment (MD). Toward the northern tip, the b-value decreases further to 0.6–0.7. This area is influenced by the Gangdese Thrust (GT) and its associated extensional faults. The presence of several minor faults in this region adds to its seismic complexity. In the epicentral block 3, the b-value ranges from 0.6-0.8. The area between 84° E- 87° E has reported significant earthquakes, including the 2015 Gorkha earthquake. This region indicated the initiation of the high compressional zone as the major seismogenic faults, such as MCT, STDS, and their extensional detachments, crumble up wiggly, resulting in stress accumulation. In comparision, epicentral blocks 4 and 5 are the most seismically active regions in the study area, contributing significantly to the overall earthquake occurrences. The complex, wiggly pattern of faults in this zone suggests intense tectonic deformation and interaction between multiple fault systems. The Main Central Thrust (MCT) and South Tibet Detachment System (STDS) are the dominant structural features and thrusts such as the Kakthang Thrust (KaT), High Himal Thrust (HHT), and Gyirong–Kangmar Thrust (GKT) play a crucial role in accommodating strain within the crust.The presence of structural extensions like the Himalayan Unconformity (HU) indicates past episodes of uplift and crustal reactivation. The b-values in this area range from 0.6 to 0.7 (±0.01), reflecting a high-stress environment capable of generating large earthquakes. Such persistently low b-values near major thrust systems typically signify increased stress accumulation and a higher probability of large-magnitude events. This interpretation aligns with the occurrence of the January 7, 2025, earthquake (M 7.1), which likely resulted from the release of long-term accumulated strain along the MCT–STDS fault network. The spatial pattern of b-values and fault complexity in blocks 4 and 5 highlights this area as a critical seismic hazard zone within the central Himalaya. The b-value in epicentral block 6 varies from 0.6 to 0.9. The block witnesses fewer earthquakes compared to the other blocks. Along the outer margins of the block, a few major earthquakes have occurred, primarily associated with the Main Central Thrust (MCT) and the High Himal Thrust (HHT), both of which are key seismogenic structures in the region. Toward the central part of the block, the b-value decreases noticeably, suggesting localized stress accumulation. Interestingly, this zone has not experienced any major earthquakes so far, implying that it may represent a potential seismic gap. Such areas often act as stress reservoirs that could generate significant future earthquakes once the accumulated strain is released. Hence, continuous monitoring of this region is crucial for understanding its evolving seismic potential and for assessing possible future seismic hazards.

Temporal b-value variation

The temporal variation of the b-value was analyzed using a moving time window containing a minimum of 50 events per bin. The results reveal a noticeable decline in the b-value prior to the mainshock, indicating a period of increased stress accumulation (Figure 8). Between 1964 and 1990, the b-value shows moderate fluctuations, likely due to the limited number of recorded events during this period. After 1990, significant variations in b-value (~0.35–1.0) are evident, reflecting alternating phases of stress accumulation and release within the region. For example, a sharp decline in b-value prior to the 28 March 1999 earthquake (Mw 5.9), which reached 0.42, indicates progressive stress build-up preceding the mainshock. Following 2000, the b-value shows frequent and abrupt changes, signifying a highly dynamic seismogenic environment. The estimated b-values for the mainshocks of 26 October 2004 (Mw 6.1) and 25 August 2008 (Mw 6.1) are 0.55 and 0.45, respectively. A pronounced minimum in b-value (~0.35) was recorded around 2015, coinciding with the 25 April 2015 Gorkha (Nepal) earthquake. This distinct low b-value prior to the event signifies intense stress accumulation and nucleation processes leading up to fault rupture.

The temporal variation in seismicity across the six epicentral blocks exhibits cyclic phases of quiescence (Q1–Q3), background activity, and mainshock occurrences, accompanied by corresponding fluctuations in b-value. The computation of b-values and the characterization of these seismic cycle phases for each epicentral block over various time windows are shown in the Table 1. During the early catalog period (1964–1994), no clear cyclic pattern was evident, likely due to limited instrumental data. After 1994, however, the b-value shows marked temporal fluctuations (~1), corresponding to distinct seismic cycle windows. These cycles encompass periods of increased activity during mainshock sequences (including foreshocks and aftershocks) and intervening phases of seismic quiescence (Q1, Q2, Q3).

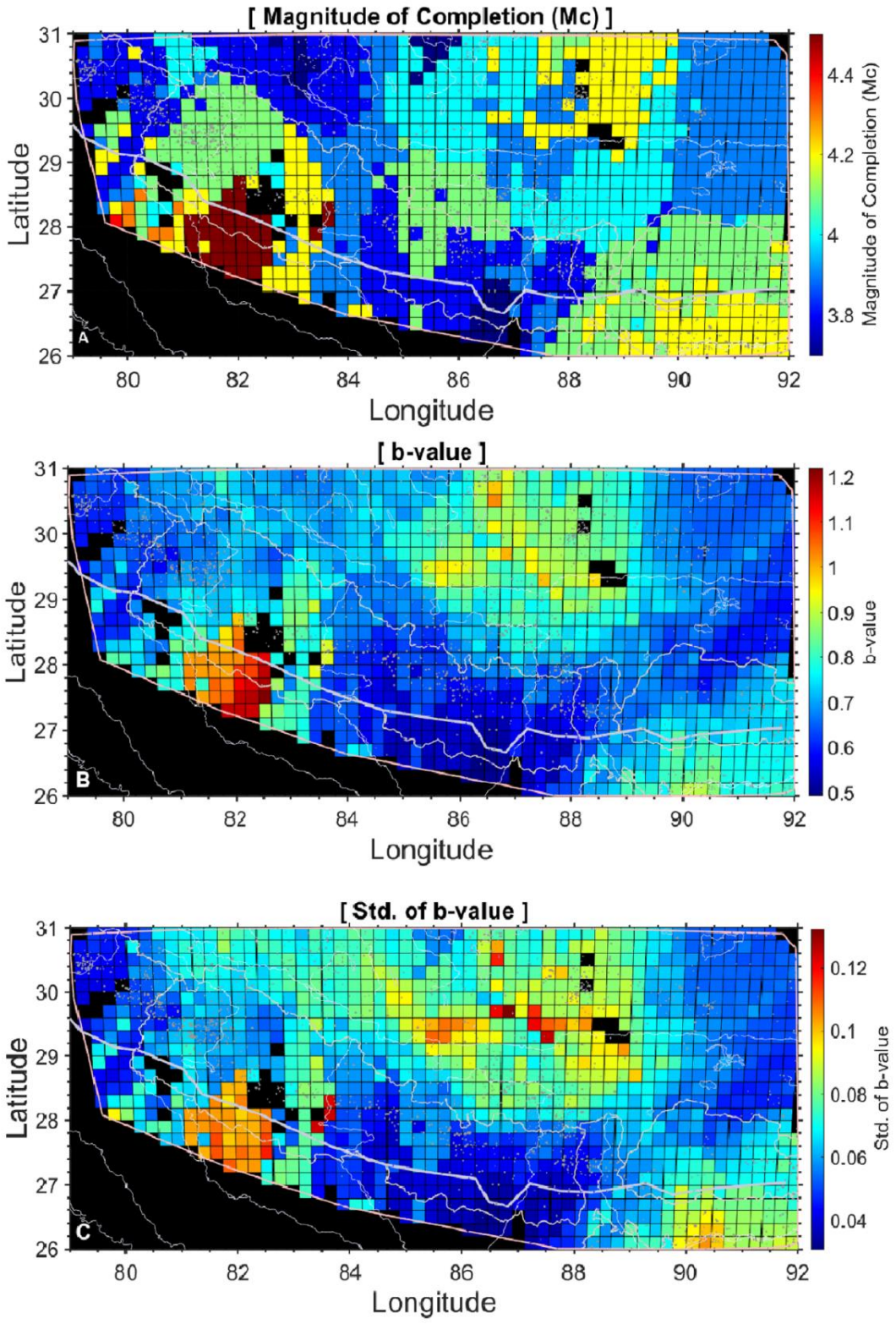

Figure 7. Spatial distribution maps showing **(A)** Magnitude of completeness (Mc), **(B)** b-value, and **(C)** standard deviation of b-value for the central Himalaya region. The white lines denote major tectonic boundaries, and the color scales indicate spatial variability in seismic parameters, highlighting regions of differing stress and seismicity characteristics.

The decline in b-value observed before major earthquakes aligns with the pre-mainshock stage of the seismic cycle, highlighting its potential as a stress indicator and possible short-term precursor.

The temporal analysis across six epicentral blocks consistently reveals a reduction in b-value preceding large earthquakes, reflecting progressive stress accumulation (Table 1). The duration of the preceding quiescent phases (Q2 + Q3) varies from 1 to 7 years, indicating spatial heterogeneity in stress buildup rates. In most cases, the pre-shock b-value is lower than the background level, with δb b ranging from 0.1 to 0.4, particularly evident before events such as those on 27 July 1980 (Mb 6.1), 29 July 1980 (Mb 6.1), 23 March 1999 (Mb 6.5), 26 October 2004 (Mb 6.1), 6 October 2008 (Mb 6.9), and 25 April 2015. These reductions in b-value suggest increased differential stress and fault strengthening prior to rupture. Conversely, a few events, for example, 19 November 1980, 22 February 1986, and 9 December 1991, exhibit minor increases in b-value before the mainshock, possibly due to local stress relaxation, complex fault interactions, or inclusion of smaller events that obscure the stress buildup signature.

The magnitude of the mainshock often correlates with the duration of the preceding quiescence. Longer quiescence intervals (≥5 years) tend to produce larger events (Mb ≥ 6.5), implying sustained stress accumulation before rupture, whereas shorter intervals (1–3 years) are associated with moderate events (Mb 5.7–6.1), reflecting faster stress release or repeated fault activation.

DISCUSSION

The spatial variation of b-values across the Himalayan region reflects the complex tectonic framework of the orogen, where intricate fault systems and heterogeneous stress regimes govern seismic behavior. Major structural elements, including the Main Central Thrust (MCT), its subsidiary MCT1, the South Tibetan Detachment (STD), the Main Boundary Thrust (MBT), and the Main Frontal Thrust (MFT), play crucial roles in shaping the regional seismotectonics. Clusters of earthquakes are predominantly associated with the MCT and MCT1, where notable spatial variations in b-value are evident. North of the MCT, relatively higher b-values are recorded, indicating lower stress accumulation, whereas the southern margin, influenced by the MBT and MFT, exhibits lower b-values (<1.0), indicating higher stress concentration and greater seismic potential. GPS measurements further corroborate this spatial variability, revealing a higher convergence rate of 18–20 ± 1 mm/yr in the eastern Himalaya (Bilham et al., 1997; Avouac, 2003; Banerjee et al., 2008), decreasing westward to approximately 13.4 ± 5 mm/yr in western Nepal (Bettinelli et al., 2006). This gradient in convergence rate aligns with the observed east–west variation in b-values along the MCT.

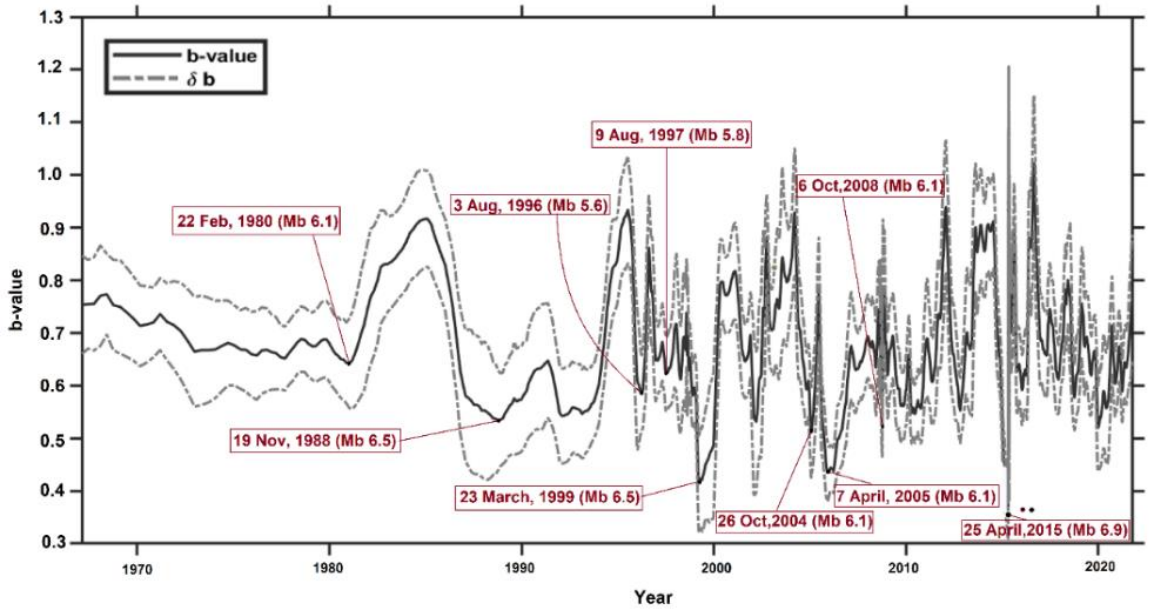

Figure 8. Temporal variation of b-value (solid line) and its standard deviation (δb; dashed line) for the central Himalaya during 1965–2020. Major earthquakes (Mb ≥ 5.5) are marked with their occurrence dates and magnitudes. Noticeable drops in b-value preceding several mainshocks indicate periods of increased stress accumulation and potential seismic quiescence before large events.

Table 1. Synthesis of seismic cycle parameters for mainshocks (Mb≥5.7)

Block	Mainshock date	Mainshock mag (Mb)	Preceding quiescence (Q2+Q3) Duration (Years)	Background b-value (± unc.)	Pre-shock b-value (± unc.)	b-value drop (Δb)
1	27-07-1980	6.1	~ 3.0	0.448	0.322	0.126
	09-12-1991	5.7	~6.0	0.452	0.488	-0.036
	23-03-1999	6.5	~2.0	0.924	0.668	0.256
	26-10-2004	6.1	~1.9	1.086	0.924	0.162
2	29-07-1980	6.1	~2.5	0.668	0.265	0.403
	09-08-1997	5.8	~2.5	0.477	0.395	0.082
	26-10-2004	6.1	~5.7	1.01	0.965	0.045
	07-04-2005	6				
	25-08-2008	6.1				
	25-04-2015	6.9	~1.5	1.059	0.835	0.224
3	24-03-1974	5.7	~1.3	0.543	0.244	0.299
	20-08-1988	6.5	~7	0.457	0.304	0.153
	11-07-2004	5.8	~3.6	1.034	1.01	0.024
	07-04-2005	6				
	25-08-2008	6.1				
	25-04-2015	6.9	~1	0.965	0.762	0.203
4	19-11-1980	6.1	~3	0.395	0.402	-0.007
	20-08-1988	6.5				
	08-09-2011	6.5	~3	1.059	0.886	0.173
	24-04-2015	6.6				
	12-05-2015	6.7				
5	22-02-1986	6.1	~3	0.356	0.381	-0.025
	30-07-1992	5.9	~1.7	0.499	0.43	0.069
	06-10-2008	6.1	~9	0.944	0.905	0.039
	18-09-2011	6.5				
6	07-01-1985	5.7	~4	0.467	0.345	0.122
	30-07-1992	5.9	~2.7	0.712	0.462	0.25
	06-10-2008	6.1	~7.0	1.206	0.905	0.301
	21-09-2009	6				

The estimated b-values in epicentral blocks 1 and 2 (western and central sectors) range between 0.6–0.8 ± 0.03, while a decline to around 0.5 ± 0.03 is observed in blocks 4 and 5 toward the eastern Himalaya. In contrast, comparatively higher b-values (1.0–1.2) are observed around the MBT and MFT, where seismic activity is less frequent, reflecting zones of lower stress accumulation. The pronounced drop in b-value (~0.5 ± 0.03) along epicentral blocks 3 and 4 (84–88.5°E) coincides with regions of high stress buildup and seismic hazard (Shanker and Sharma, 1998; Yadav et al., 2009; Raghukanth, 2010; Chingtham et al., 2017; Kumar and Sharma, 2019). These blocks 3 and 4 have experienced several major earthquakes (Mb ≥ 6), including the devastating 2015 Gorkha earthquake and the recent 2025 Nepal event.

Seismicity is concentrated between the MCT–STD system to the north and the MBT–MFT to the south. A distinct pattern is observed along the STD, where earthquakes at depths greater than 45 km exhibit lower b-values (0.7–0.9), a feature not evident in other segments. These deeper events suggest downward-propagating thrust faulting and crustal deformation, indicative of continued stress accumulation between the MCT and STD. Pudi et al. (2018) reported an increase in b-value following the 2015 earthquake, consistent with post-seismic stress release, while Jena et al. (2021) noted significant event clustering in the Nepal Himalaya. Shanker and Sharma (1998) also documented a west-to-east variation in b-value from 0.63 to 0.94, supporting the regional-scale pattern identified in the present study.

The temporal variation of b-value offers further insights. After 1994, the b-value shows marked temporal fluctuations (~1), corresponding to distinct seismic cycle windows. These cycles encompass periods of increased activity during mainshock sequences and intervening phases of seismic quiescence (Q1, Q2, Q3). The decline in b-value observed before major

earthquakes aligns with the pre-mainshock stage of the seismic cycle, highlighting its potential as a stress indicator and possible short-term precursor. A pronounced minimum in b-value (~0.35) was recorded around 2015, coinciding with the 25 April 2015 Gorkha (Nepal) earthquake. This distinct low b-value prior to the event signifies intense stress accumulation and nucleation processes leading up to fault rupture.

CONCLUSIONS

The spatial and temporal variations in b-value across the Himalayan region reveal a highly heterogeneous stress regime closely linked to its complex tectonic architecture. The low b-values (<0.8) concentrated along the MCT and MCT1, correspond to zones of elevated stress accumulation and frequent large-magnitude events, including the 2015 Gorkha and 2025 Nepal earthquakes. In contrast, higher b-values (1.0–1.2) along the MBT and MFT mark relatively stable regions of reduced stress buildup. The observed west–east decline in b-value (from 0.8 to 0.5) parallels the decrease in plate convergence rate from ~20 ± 1 mm/yr in the east to ~13 ± 5 mm/yr in the west, indicating a strong kinematic control on regional stress distribution. Temporally, successive seismic cycle windows exhibit a recurring pattern of quiescence followed by a sharp drop in b-value (δb = 0.1–0.4) preceding major earthquakes, signifying progressive stress loading and fault strengthening before rupture. Longer quiescence periods (≥5 years) consistently precede higher-magnitude events (Mb ≥ 6.5), reflecting time-dependent stress accumulation along locked fault segments. The spatial pattern of b-values and fault complexity in blocks 4 and 5 (85°-89° E) highlights this area as a critical seismic hazard zone within the central Himalaya. The area falling between 89°-92° E showing lower b-values and interestingly the area has not experienced any major earthquakes so far, implying that it may represent a potential seismic gap. Continuous monitoring of this region is crucial for understanding its evolving seismic potential and for assessing possible future seismic hazards.

Acknowledgements

We gratefully acknowledge the Department of Earth Sciences, Pondicherry University, for their support in facilitating this research. We would also like to thank Dr. Stefan Wiemer, of the Swiss Seismological Service, Institute of Geophysics, Swiss Federal Institute of Technology Zurich for ZMAP software (Wiemer, 2001). The author, Ashisan Dhodray, gratefully acknowledges the financial support provided by the National Fellowship for Scheduled Tribes (202223-NFST-JHA-01247), awarded by the Ministry of Tribal Affairs, Government of India. We sincerely acknowledge Dr. Anil Earnest, Principal Scientist, CSIR–Fourth Paradigm Institute, Dr. O. P. Pandey, Chief Editor of JIGU, and the anonymous reviewer for their valuable comments and constructive suggestions that significantly improved the quality of this manuscript..

Author credit statement

Ashisan Dhodray : Visualization, investigation, formal analysis, writing the initial draft; S. Lasitha: Conceptualization, methodology, supervision, data curation, validation, writing, review and editing.

Data availability

Data can be made available by corresponding author on a reasonable request

Compliance with ethical standards

The authors declare that they have no known competing financial interests or personal relationships that could have appeared to influence the work reported in this paper. They adhere to copyright norms

References

Aki, K., 1965. Maximum likelihood estimate of b in the formula log10N = a – bm and its confidence limits. Bull. Earthq. Res. Inst., 43, 237–239.

Ambraseys, N. and Bilham, R., 2003. Earthquakes and associated deformation in northern Baluchistan 1892–2001. Bull. Seismol. Soc. Am., 93, 1573–1605.

Amitrano, D., 2003. Brittle–ductile transition and associated seismicity: Experimental and numerical studies and relationship with the b value. J. Geophys. Res. Solid Earth, 108, 2044.

Auden, J.B. and Gansser, A., 1967. Geology of the Himalayas. Geogr. J., 133, 84–85.

Avouac, J.P., 2003. Mountain building, erosion, and the seismic cycle in the Nepal Himalaya. Adv. Geophys., 46, 1–80.

Banerjee, P., Bürgmann, R., Nagarajan, B. and Apel, E., 2008. Intraplate deformation of the Indian subcontinent. Geophys. Res. Lett., 35, L18301.

Bettinelli, P., Avouac, J.P., Flouzat, M., Jouanne, F., Bollinger, L., Willis, P. and Chitrakar, G.R., 2006. Plate motion of India and interseismic strain in the Nepal Himalaya from GPS and DORIS measurements. J. Geod., 80, 567–589.

Bilham, R., Larson, K. and Freymueller, J., 1997. GPS measurements of present-day convergence across the Nepal Himalaya. Nature, 386, 61–64.

Chingtham, P., Prajapati, S.K., Gahalaut, V.K., Chopra, S. and Singha Roy, P., 2017. Forecasting seismicity rate in the north-west Himalaya using rate and state dependent friction law. Geomatics Nat. Hazards Risk, 8, 1643–1661.

Colavitti, L., Bindi, D., Tarchini, G., Scafidi, D., Picozzi, M. and Spallarossa, D., 2025. A high-quality data set for seismological studies in the East Anatolian Fault Zone, Türkiye. Earth Syst. Sci. Data, 17, 3089–3108.

Elliott, J.R., Jolivet, R., Gonzalez, P.J., Avouac, J.P., Hollingsworth, J., Searle, M.P. and Stevens, V.L., 2016. Himalayan megathrust geometry and relation to topography revealed by the Gorkha earthquake. Nat. Geosci., 9, 174–180.

Engdahl, E.R., 2006. Application of an improved algorithm to high precision relocation of ISC test events. Phys. Earth Planet. Int., 158, 14-18.

Fuggi, A., Re, S., Tango, G., Del Gaudio, S., Brovelli, A. and Cassiani, G., 2024. Assessment of earthquake location uncertainties for the design of local seismic networks. Earthq. Sci., 37, 415–433.

Gardner, J.K. and Knopoff, L., 1974. Is the sequence of earthquakes in Southern California, with aftershocks removed, Poissonian? Bull. Seismol. Soc. Am., 64, 1363–1367.

Hayes, G.P. and Briggs, R.W., 2017. Introduction to the special issue on the 25 April 2015 Mw 7.8 Gorkha (Nepal) earthquake. Tectonophysics. 714-715, 1-3.

Jena, R., Pradhan, B., Naik, S.P. and Alamri, A.M., 2021. Earthquake risk assessment in NE India using deep learning and geospatial analysis. Geosci. Front., 12, 101110.

Kagan, Y.Y., 1999. Universality of the seismic moment–frequency relation. Pure Appl. Geophys., 155, 537–573.

Knopoff, L., Aki, K., Archambeau, C.B., Ben-Menahem, A. and Hudson, J.A., 1964. Attenuation of dispersed waves. J. Geophys. Res., 69, 1655–1657.

Kothyari, H.C., Kothyari, G.C., Joshi, R.C., Gururani, K., Nandy, S. and Patidar, A.K., 2024. Assessment of fluvial response to landslide susceptibility and tectonic activity in the upper Alaknanda River basin, Uttarakhand Himalaya, India. Quat. Sci. Adv., 15, 100221.

Kumar, S. and Sharma, N., 2019. The seismicity of central and north-east Himalayan region. Contrib. Geophys. Geod., 49, 265–281.

Kundu, B., Yadav, R.K., Bali, B.S., Chowdhury, S. and Gahalaut, V.K., 2014. Oblique convergence and slip partitioning in the NW Himalaya: implications from GPS measurements. Tectonics, 33, 2013-2024.

Kundu, B., Vissa, N.K. and Gahalaut, V.K., 2015. Influence of anthropogenic groundwater unloading in the Indo-Gangetic plains on the 25 April 2015 Mw 7.8 Gorkha, Nepal earthquake. Geophys. Res. Lett., 42, 10607–10613.

Li, L., Shen, W., Sui, S., Yao, H. and Bao, Z., 2021. Crustal thickness beneath the Tanlu Fault Zone and its tectonic significance based on two-layer H–κ stacking. Earthq. Sci., 34, 47–63.

Le Fort, P., 1975. Himalayas: the collided range, present knowledge of the continental arc. Am. J. Sci., 275A, 1-44.

Molnar, P. and Lyon-Caent, H., 1989. Fault plane solutions of earthquakes and active tectonics of the Tibetan Plateau and its margins. Geophys. J. Int., 99, 123–153.

Murphy, M.A., Taylor, M.H., Gosse, J., Silver, C.R.P., Whipp, D.M. and Beaumont, C., 2014. Limit of strain partitioning in the Himalaya marked by large earthquakes in western Nepal. Nat. Geosci., 7, 38–42.

Pudi, R., Roy, P., Martha, T.R., Kumar, K.V. and Rao, P.R., 2018. Spatial potential analysis of earthquakes in the western Himalayas using b-value and thrust association. J. Geol. Soc. India, 91, 664–670.

Raghukanth, S.T.G., 2010. Estimation of seismicity parameters for India. Seismol. Res. Lett., 81, 207–217.

Sandwell, D.T. and Smith, W.H.F., 1997. Marine gravity anomaly from Geosat and ERS-1 satellite altimetry. J. Geophys. Res. Solid Earth, 102, 10039–10054.

Scholz, C.H., 1968. Mechanism of creep in brittle rock. J. Geophys. Res., 73, 3295–3302.

Schorlemmer, D. and Wiemer, S., 2005. Microseismicity data forecast rupture area. Nature, 434, 1086.

Searle, M.P., Law, R.D., Godin, L., Larson, K.P., Streule, M.J., Cottle, J.M. and Jessup, M.J., 2008. Defining the Himalayan Main Central Thrust in Nepal. J. Geol. Soc., 165, 523–534.

Shanker, D. and Sharma, M.L., 1998. Estimation of seismic hazard parameters for the Himalayas and its vicinity from complete data files. Pure Appl. Geophys., 152, 267–279.

Shi, Y. and Bolt, B.A., 1982. The standard error of the magnitude–frequency b value. Bull. Seismol. Soc. Am., 72, 1677–1687.

Singh, C., 2016. Spatial variation of seismic b-values across the NW Himalaya. Geomatics Nat. Hazards Risk, 7, 522–530.

Singh, A.K., Chung, S.L. and Somerville, I.D., 2022. Geodynamic evolution of eastern Himalaya and Indo-Myanmar orogenic belts: advances through interdisciplinary studies. Geol. J., 57, 476-481.

Smith, W.D., 1981. The b-value as an earthquake precursor. Nature, 289, 136–139.

Styron, R.H., Taylor, M.H. and Murphy, M.A., 2011. Oblique convergence, arc-parallel extension, and the role of strike-slip faulting in the High Himalaya. Geosphere, 7, 582–596.

Thakur, V.C., 1991. Regional framework and tectonics of the Yarlung Zangbo suture in southern Tibet. Phys. Chem. Earth, 18, 221–235.

Utsu, T., 1974. A three-parameter formula for magnitude distribution of earthquakes. J. Phys. Earth, 22, 71–85.

Valdiya, K.S., 1976. Himalayan transverse faults and folds and their parallelism with subsurface structures of North Indian plains. Tectonophysics, 32, 353–386.

Valdiya, K.S., 2002. Emergence and evolution of Himalaya: reconstructing history in the light of recent studies. Prog. Phys. Geogr. Earth Environ., 26, 360–399.

Wiemer, S. and Wyss, M., 1997. Mapping the frequency–magnitude distribution in asperities: an improved technique to calculate recurrence times? J. Geophys. Res. Solid Earth, 102, 15115-15128.

Wiemer, S., Yoshida, A., Hosono, K., Noguchi, S.I. and Takayama, H., 2005. Correlating seismicity parameters and subsidence in the Tokai region, central Japan. J. Geophys. Res. Solid Earth, 110, B10303.

Wu, Y.M., Chen, S.K., Huang, T.C., Huang, H.H., Chao, W.A. and Koulakov, I., 2018. Relationship between earthquake b-values and crustal stresses in a young orogenic belt. Geophys. Res. Lett., 45, 1832–1837.

Wyss, M., Shimazaki, K. and Ito, A., 1999. Seismicity patterns, their statistical significance and physical meaning. Pure Appl. Geophys., 155, 203–205.

Yadav, R.B.S., Bormann, P., Rastogi, B.K., Das, M.C. and Chopra, S., 2009. A homogeneous and complete earthquake catalog for northeast India and the adjoining region. Seismol. Res. Lett., 80, 609–627.

Received on: 17-1-2025; Revised on: 9-1-2026; Accepted on: 10-1-2026

J. Ind. Geophys. Union, 30(2) (2026), 102-113
https://doi.org/10.71122/JIGU.30(2)2026.0011

Laser Raman characterization and 3D mapping of chromite crystal from Asurabandha mines of Bhuban ultramafic complex, Odisha (India)

Ashish Gupta and Dinesh Pandit*
Department of Geology, Institute of Science, Banaras Hindu University, Varanasi - 221005, India,
Corresponding author: dpandit@hotmail.com

ABSTRACT

The Asurabandha chromite deposits are hosted in the Bhuban Ultramafic Complex (BUC), which is located in the Dhenkanal district of Odisha. The BUC forms part of the transition domain between the Singhbhum Craton and the Eastern Ghats Mobile Belt (EGMB). Highly altered chromitite rocks are found as isolated, irregular and sporadic orebodies located on the southern side of the Sukinda Ultramafic Complex (SUC) accompanied by the granite-charnockite association. Petrographic studies inferred the existence of heteradcumulate texture in the chromitite rock, which indicates early crystallization during the cooling of an ultramafic magma. Chromite begins to crystallize at a high temperature and accumulates to growth of crystal framework, subsequently crystallizing to form silicate minerals (olivine or pyroxene), that later altered to serpentine. Occurrences of euhedral chromite crystal indicates inherent crystal growth during the crystallization of magma. The Laser Raman Micro Spectroscopy (LRMS) analysis, displays four characteristics Raman Shift at 454, 559, 736 and 1437 cm^{-1} for chromite and five diagnostic Raman Shift at 127, 206, 397, 465 and 1166 cm^{-1} for serpentine. Laser Raman-SNOM scanning, 2D and 3D mapping of euhedral hexagonal chromite crystal, suggests its heterogenous internal crystal structure in the ultramafic rocks. In the chromite crystal, internal heterogeneity may appear because of trace element substitution during the magmatic crystallization or secondary alteration processes like serpentinization and carbonation. The Asurabandha chromite deposits are characterized by metasomatic alteration, serpentinization and carbonation, where original silicate minerals have been replaced by serpentine, presenting challenges for mineral exploration due to the extent beyond lateritic overburden.

Keywords: Laser Raman, Chromite, Serpentine, Ultramafic Rocks, Asurabandha, Bhuban Ultramafic Complex, Singhbhum craton.

INTRODUCTION

The Laser Raman Micro Spectroscopy (LRMS) is an in-situ scientific technique that uses inelastic scattering of light from a laser to provide a chemical 'fingerprint' of a sample's vibrational, rotational, and other low-frequency vibrational modes (Raman, 1922; Hope et al., 2001). By measuring the Raman Shift (the difference in frequency between the scattered and incident light), one can identify molecules, analyse their structure, and determine their composition in various forms, including solids, liquids, and gases (Raman, 1923). The technique requires a laser beam for excitation, a sample interface, and a spectrometer to disperse and detect the scattered light (Raman, 1942, 1947). The LRMS technique is applied to identify minerals by analysing light scattering, which creates a unique "spectral fingerprint" from a mineral's atomic vibrations (McMillan, 1989; Keresztury, 2006). This non-destructive method requires little to minimum sample preparation, complementing other techniques like Scanning Electron Microscopy (SEM) and X-ray Diffraction (XRD) to provide detailed chemical and structural information. This Laser Raman technique is valuable for fieldwork and identifying difficult-to-discern minerals like light-coloured silicates. A mineral sample is exposed to a monochromatic light beam, usually a laser. The light interacts with the mineral's chemical bonds, causing some of the light to scatter inelastically (Raman, 1927, 1928; Raman and Krishnan, 1928). The scattered light has a unique energy shift or Raman Shift depending on the mineral's crystal structure, atomic masses, bond-lengths, and bond-angles (Raman, 1929, 1945). A spectrometer captures this scattered light and analyses the energy shifts to produce a unique spectrum or Raman Shift or "fingerprint," for that mineral.

The LRMS's ability to provide rapid identification of mineral phases is beneficial for exploration, especially for minerals that are hard to identify optically using a polarising microscope (Rodgers, 1993; Bersani and Lottici, 2016). This method helps to differentiate between minerals with similar appearance but different chemical compositions, such as various silicate, sulphide and carbonate groups (Pandit, 2024). It is also useful for identifying opaque or weathered grains that are difficult to analyse with traditional optical microscopy (Singh and Pandit, 2025). This is a non-destructive technique and does not alter or destroy the sample. Minimal sample preparation is required for the LRMS studies, which means samples often require no specific preparation. It can be used on a wide variety of sample types and sizes, from small powders to large piece of samples. The LRMS is a valuable tool when simultaneously used with microscopy and X-ray diffraction to identify minerals.

The objective of this study is emphases on phase recognition in the mineralized ultramafic rocks by analysing a mineral's physical and optical properties, crystalline structure, size, shape, and textural position to identify their petrogenetic implications. The characterization of mineral phases in the ultramafic rock involving the LRMS technique with the help of 532 nm wavelength excitation. In general, the essential minerals found in ultramafic rocks are olivine and pyroxene, with smaller amounts of garnet and spinel. Chromite is an important economic mineral found predominantly in ultramafic rocks, which include peridotite, dunite, and serpentinite.

Characterization of mineral phases in ultramafic rocks will help to understand the origin of chromite crystals in the orebody of the Asurabandha deposits, located in the Dhenkanal district of Odisha.

REGIONAL GEOLOGY

The Singhbhum Craton is an ancient geological terrain in the Jharkhand and Odisha states of India, characterized by its >3.5 Ga old Archean granite and greenstone belts. The Singhbhum Craton is enormously rich in mineral resources, particularly iron and copper, with a geological history including Archean metamorphic rocks, volcano-sedimentary sequences, and sedimentary layers, providing crucial insights into continental crustal development and the Archean Earth processes. It features a central granitic batholith surrounded by greenstone belts that contain various types of volcanic and sedimentary rocks. The Singhbhum Craton located in Peninsular India, hosts significant ultramafic complexes, such as the Sukinda and Baula-Nuasahi complex, which are important for their hosted chromite and PGE deposits. These layered ultramafic bodies, consisting of rocks like dunite, pyroxenite, gabbro and serpentinite, that are found within the Archaean Iron Ore Group (IOG) of volcano-sedimentary successions. The southern marginal zone of the Singhbhum Craton boarders with EGMB, encompassing chromite hosted layered ultramafic bodies (Figure 1a). Apart from the prominent ultramafic complexes like the Baula-Nuasahi Ultramafic Complex (BNUC) and the Sukinda Ultramafic Complex (SUC), there is some recently identified ultramafic complex, like the Bhuban Ultramafic Complex (BUC) in the Dhenkanal district of Odisha (Tripathy et al., 2014). The BUC forms part of the transition zone between the Singhbhum Craton and the EGMB, which exposes rocks belonging to cratonic fringe as well as the granulites (Figure 1b). The northern margin of EGMB against the Singhbhum Craton, distinctly considered as a strike-slip fault or exposing the deeper crustal segment of the Archean crust through oblique transpression, represents a complex geological setting (Mishra and Gupta, 2013).

A number of small chromiferous ultramafic bodies occur towards southeast of the SUC within the granulite terrains north of the Maulabhanja Parbat towards the west and Asurabandh towards the east (Banerjee et al., 1972). Another small chromiferous ultramafic body occurs further east of Asurabandha nearby Bhuban. All these three dismembered chromiferous ultramafic units are clubbed together and here after called as the Bhuban Ultramafic Complex (BUC). The stratigraphic corelation between BUC with respect to the SUC and the BNUC remains speculative. Asurabandha area is characterized by ultramafic bodies containing chromite, which are found within the less-understood granulite tracts near the SUC (Figure 1b). These ultramafic rocks are partially covered by a thick laterite overburden. Geological studies have utilized gravity and magnetic surveys to investigate the concealed chromite mineral potential of the Asurabandha - Bhuban area (Arasada et al., 2020). The BUC is characterized by the emplacement of a number of lensoidal bodies of chromiferous ultramafic rocks. Layered mafic-ultramafic rocks represented by dunite, peridotite, and gabbro occurs as lenses within granite-charnockite association along the transition domain between the Singhbhum Craton and the EGMB. In the study area, lensoidal chromite bearing rocks are highly prone to alteration and weathering as well as extend beyond lateritic overburden. The Bhuban-Asurabandha area is represented by low physiographic terrain. A number of old working pits are located in this area around three different localities nearby Chandar, Bhuban and Maulabhanja Parbat areas (Tripathy et al., 2014).

In Asurabandha area, the ultramafic complex has experienced widespread lateritization and serpentinization to several stages of hydrothermal alterations. Apart from the chromite-bearing weathered peridotite, the other ultramafic or mafic rocks include gabbro, pyroxenite, anorthosite and gabbroic-anorthosite (Figure 2a). In spite of restricted exposures, they form essential components of a magmatic suite of rocks. The ultramafic body occurred in the form of chromite-bearing weathered peridotite, gradually transit close to gabbro and anorthositic-gabbro. The compositional variation is observed only in a few metres wide exposed outcrops. These bodies are circular to semi-circular or elliptical in nature. The ultramafic rocks like dunite, peridotite, serpentinite and silicified serpentinite bodies with chert and chromite occurs as discrete isolated bodies in the granitic-charnockite terrain. They do not show any regularity, either in distribution pattern or in concentration of chromite. Chromite is found in irregular form and in small dimensions with massive, spotted and banded varieties (Figure 2b). The silica veins traversing serpentinite are quite frequently observed in this area. At several places, the ultramafic rocks have been altered to chrysotile asbestos, which is green colour, hard compact and light in weight. Relatively, fresh samples of peridotites consist of olivine and enstatite with magnetite, chromite, and apatite as accessories. The dunite is altered to a felted mass of talc-serpentine.

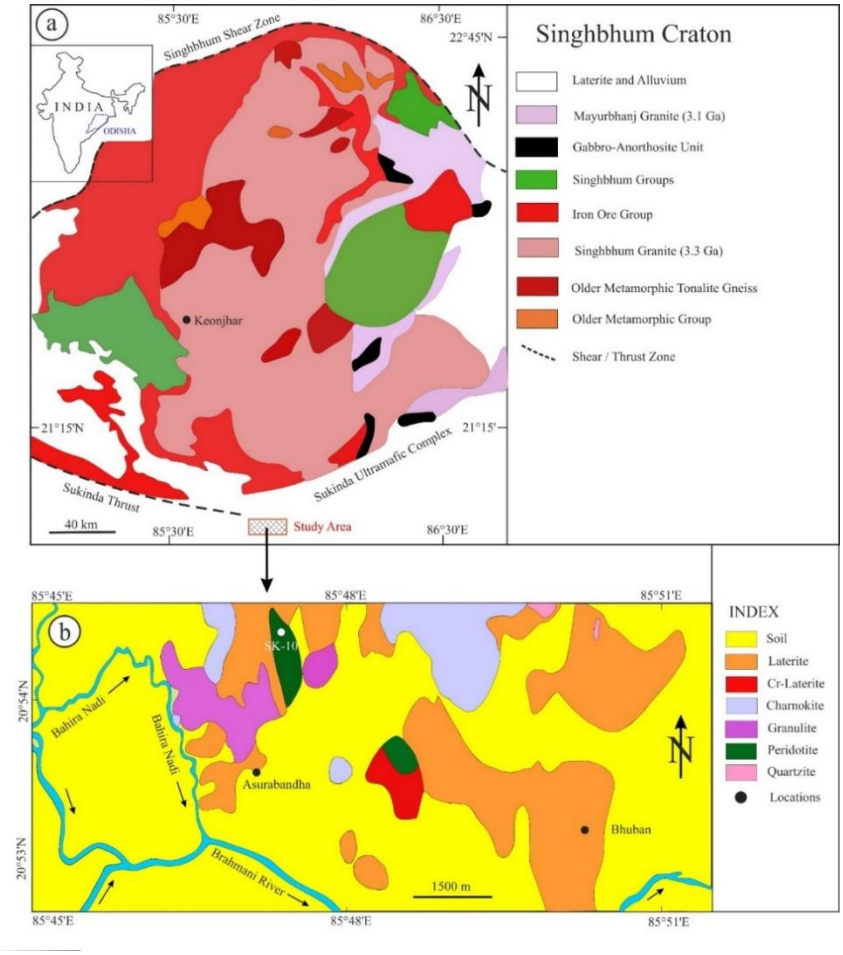

Figure 1. (a) Generalised geological map of the Singhbhum Craton (after Saha, 1994) and its adjacent areas with an inset of map of India displaying study area in Odisha. The cross-hatched red colour box is shown to represents the study area of the Bhuban Ultramafic Complex (BUC). **(b)** Geological map of Asurabandha chromite deposits of the BUC in Dhenkanal district of Odisha (modified after Sahoo, 2014; Tripathy et al., 2014; Arasada et al., 2020; Behera and Nayak, 2023).

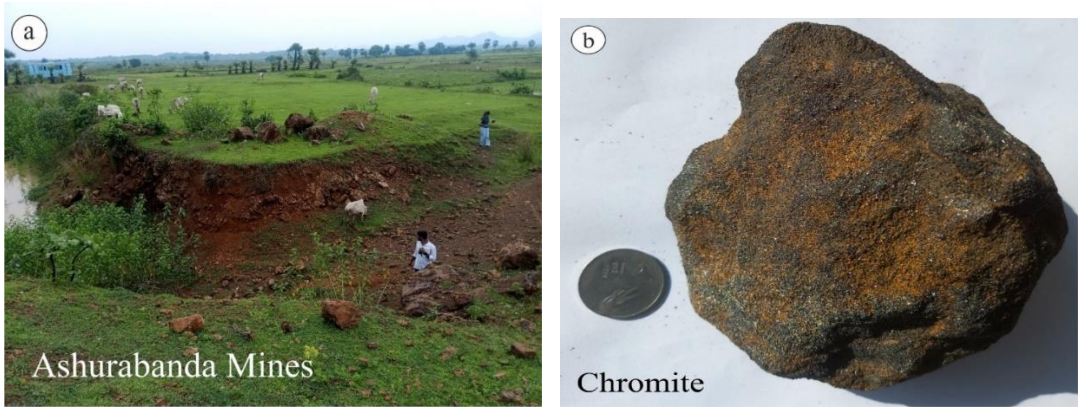

Figure 2. (a) Field photograph showing exposed area of the Asurabandha Chromite Mines. **(b)** Hand specimen of chromite sample from the Asurabandha Mines in Dhenkanal district of Odisha. The metallic lustre with well-developed granular texture is a diagnostic feature of magmatic chromite ore. The chromite ore exhibits secondary alteration features of serpentine and goethite.

SAMPLE PREPARATION

A small piece of rock is cut, ground to a smooth surface, and then pasted to a glass slide. The mounted rock slice is then ground down to a very thin layer using progressively finer abrasive grits and water, often with the aid of specialized grinding machines. This step continues until the desired thickness of approximately 30 micrometers is achieved. Excess

material is removed to create a thin slice, allowing light to pass through. Grinding of the sample to a precise thickness of about 30 micrometers is done using progressively finer abrasives, and then by systematic polishing. The sample surface is then polished to a smooth and flat appearance. The prepared thin section is used for petrographic study under a polarized-light microscope to identify its constituent minerals, texture, and structure. Microscopic study of the thin section is performed in the Department of Geology, Institute of Science, Banaras Hindu University, India. Mineral identification by rotating the polarizing filters attached with the microscope, that can identify individual minerals based on their unique optical properties, such as colour, birefringence, and crystal shape. Texture and fabric analysis consists of the arrangement, shape, and size of mineral grains, as well as any cracks or other structural features.

PETROGRAPHY

The chromite ores from the Asurabandha area are examined under thin section using a petrological microscope. These samples show cumulus texture formed by 70 to 90% euhedral chromite grains in an altered and silicified matrix comprising of serpentine group of minerals. In plane polarized transmitted light (PPTL) mode, chromite (opaque grains) in ultramafic rocks display massive, disseminated, or granular textures, with grains often exhibiting euhedral to subhedral shapes and intergrown with interstitial serpentine (pale yellow colour) or olivine's remnant (Figure 3a). Grains may form compact mosaics, chains, or clots. In cross polarized transmitted light (XPTL) mode, chromite appears as opaque grains surrounded by interstitial silicate matrix of serpentine typically appearing as an anisotropic mineral with low first-order interference colours (Figure 3b). Serpentine displays black, white, and grey hues with sweeping undulose extinction. Under plane polarised reflected light (PPRL) mode, the chromite grains show fractures, filled up with secondary silicate matrix (Figure 3c). The chromite grains contain very fine inclusions of silicate matrix. The shape of the chromite grains varies from hexagonal, euhedral to subhedral and size varies from 10 to 500 µm recognised as heteradcumulate texture. It shows heterogeneous distribution of the chromite crystal aggregates in the ultramafic rocks of the Asurabandha chromite deposit. A heteradcumulate texture represents euhedral to subhedral chromite grains that are surrounded by inter-cumulus minerals, such as serpentine or olivine (Wager et al., 1960; Campbell, 1978). The dunite is altered to talc-serpentine rock, often preserving ghost heteradcumulate texture, formed by hexagonal pseudomorphs of chromite having rims of released iron rich secondary mineral phases (Figure 4a**).** In XPTL mode, the chromite grains, although opaque phase, are interpreted on the basis of hexagonal shape and surrounding silicate matrix of serpentine (Figure 4b). In PPRL mode, chromite grains are appearing as perfect hexagonal crystallized grains with white colour interstitial spaced filled by silicate matrix of serpentine (Figure 4c). There are some secondary mineral phases filled in the fractures that facilitated alteration displayed as pale-green colour hues most probably goethite. Altered peridotite with preserved pyroxene and chromite cumulates are sometimes observed under XPTL mode with imprints of metasomatism and post alteration patterns of serpentinization and carbonation. This alteration process, recognized as serpentinization or hydrothermal alteration, involves the interaction of the hot, mineral-laden fluids with the chromite, causing the chromium to become incorporated into new carbonate minerals (Kraemer et al., 2021). Hydrothermal alteration, prevalent in serpentinization and low to mid-amphibolite facies metamorphism, results in the breakdown of the primary chromite structure and the redistribution of Mg and Al, ultimately changing the chromite's chemical composition and creating zoned alteration rims (Barnes, 2000; Santti et al., 2006). Carbonation of chromite is a dissolution-precipitation process, where metals in chromite react with carbon dioxide (CO_2) in presence of mineralising fluids to form carbonate minerals (Ashwal and Cairncross, 1997).

LASER RAMAN MICRO SPECTROSCOPY: THEORY AND METHODOLOGY

The Raman effect is a phenomenon where monochromatic light (like laser light) interacts with a substance, causing a small fraction of the light to be scattered at a different frequency, or wavelength (Raman, 1922, 1923). The Raman scattering is the inelastic scattering of photons by a molecule, where the radiation or photon's energy is either gained or lost by the molecule or crystals, resulting in a scattered photon with a different energy (frequency) than the incident radiation or photon (Raman, 1928, 1929). This process occurs when incident monochromatic light (like from a laser) interacts with a molecule, exciting it to a temporary virtual energy state, and then the molecule relaxes back to a vibrational state, releasing a radiation or photon (Raman, 1942, 1943). A laser beam shines onto the sample, exciting molecules into a virtual energy state, the molecules relax, most photons are scattered elastically (Rayleigh scattering) with the same energy. However, a small fraction undergoes inelastic scattering (Raman scattering), where the scattered photon's energy (and thus its frequency) is shifted up or down (Raman, 1945, 1947). The variance in energy amongst the incident and scattered photons, provides a unique "fingerprint" of the molecule's vibrational modes, which can be used for material identification and characterization (Neuville et al., 2014). The variance in frequency amongst the incident and scattered light is recognized as the Raman Shift, which factor is measured in cm^{-1} unit. A spectrometer analyses the intensity of these scattered photons at different Raman Shifts, producing a unique spectrum that acts as a "fingerprint" for the sample.

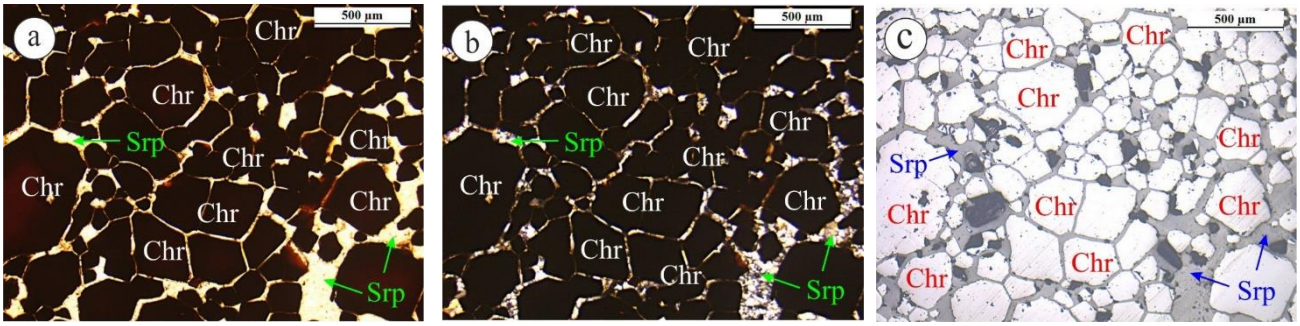

Figure 3. Photomicrograph (5X magnification) of chromite in ultramafic rock from the Asurabandha Mines in Dhenkanal district of Odisha. In ultramafic rock, euhedral and subhedral chromite grains are commonly displays heteradcumulate textures, with silicate minerals (serpentine) filling the interspaces between the grains**. (a)** In plane polarized transmitted light (PPTL) mode, chromite-serpentine matrix is shown as serpentine colourless whereas chromite appears as black under**. (b)** In cross polarized transmitted light (XPTL) mode, chromite shows black colour and serpentine exhibits grey colour. **(c)** In plane polarized reflected light (PPRL) mode, chromite crystals show white colour and serpentine-silicate matrix displays grey-black colour. Chr - chromite, Srp - serpentine.

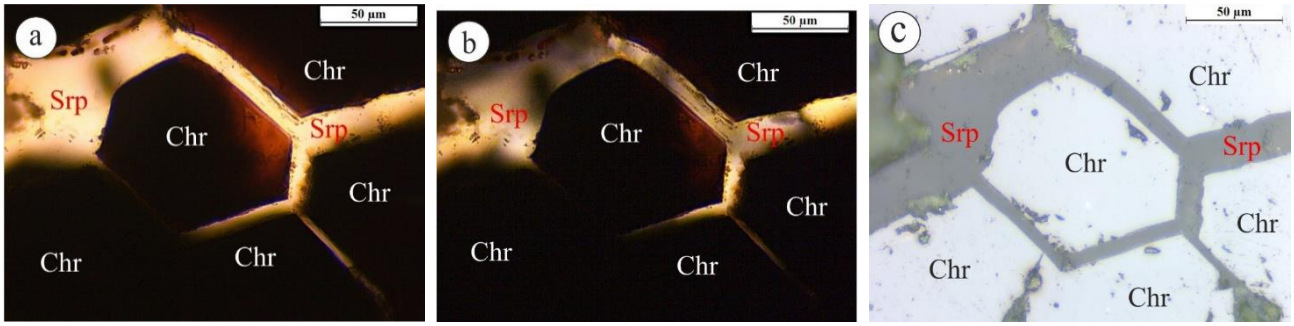

Figure 4. Photomicrograph (50X magnification) of chromite in ultramafic rock from the Asurabandha Mines in Dhenkanal district of Odisha. Serpentine occurs as packing the interspaces between the chromite grains**. (a)** Under PPTL mode, chromite appears as opaque with euhedral, hexagonal shape crystals and serpentine exhibits pale-yellow to colourless. **(b)** Under XPTL mode, serpentine exhibits pale-yellow colour and chromite is opaque**. (c)** Under PPRL mode, chromite appears as white colour, euhedral hexagonal shape crystals, serpentine displays grey colour and secondary minerals (goethite) show green colour along the interspaces between chromite crystals. Chr - chromite, Srp - serpentine.

The LRMS is a non-destructive technique that uses a laser and microscope to analyse the vibrational spectrum of a sample's molecules, providing a chemical "fingerprint" with high spatial resolution (around 1 µm). It works by analysing inelastic (Raman) light scattering, where the energy of the light changes due to interactions with the sample's molecular vibrations. The LRMS combine with a Scanning Near-field Optical Microscopy (SNOM) instrument is to circumvent the diffraction limit of conventional light microscopy by using a subwavelength-sized aperture or tip to probe the near-field of the sample (Vandenabeele, 2013). This integration permits for the acquisition of topographic and chemical information on the surface characterization of minerals at the nanoscale investigations (>100 nm). By scanning Raman-SNOM probe across a sample surface at a close distance, the technique collects optical information, such as transmitted, reflected, or fluorescent light, by exploiting evanescent waves or tip-scattered light. This allows for the simultaneous imaging of topography and optical properties with high spatial resolution, making it useful in fields like nanotechnology, geology, and materials science. The detail procedure of mineral characterization using the Raman-SNOM probe is performed at the Central Discovery Centre (CDC), Banaras Hindu University, India (Pandit, 2024). Raman spectral mapping is a hyperspectral imaging technique that provides detailed chemical and structural information by acquiring a full Raman spectrum at every pixel of an image. Using Laser Raman 2D and 3D mapping distinctions in these spectra. This technique creates false-colour images that reveal the spatial distribution of different chemical components within a sample, allowing for the visualization of features invisible to standard optical microscopy. The RRUFF database contains Raman spectra, and chemistry data of minerals, offering a powerful tool for their identification (Lafuente et al., 2015). This software assists in analysing and identifying minerals by comparing collected spectra to those available in the RRUFF website (https://rruff.info/).

RESULTS

The Laser Raman-SNOM system (MakeWITec, GmbH, model: alpha 300-RAS) attached with 532 nm wavelength laser beam using a solid state Nd:YAG crystal operated through output power 0.3 to 1 mW. The analytical resolution of Raman-SNOM instrument can range from 2 to 4 cm^{-1} for routine data

acquisition, covering full spectral range from 100 to 3500 cm^{-1} with an accuracy of ±5cm^{-1} or even higher. The Raman spectra were acquired from chromite crystal and surrounding silicate phase or matrix, using 532 nm wavelength excitation laser which is focused on polished thin sections of ultramafic rock sample (Figure 5a).

The grey colour silicate matrix of serpentine is recognized by five indicative Raman Shifts at around 127, 206, 397, 465 and 1166 cm^{-1} (Figure 5b). Serpentine is a Mg-Fe-rich layered silicate mineral group [nominally $(Mg,Fe)_3Si_2O_5(OH)_4$] with three distinct polymorphs such as antigorite, chrysotile and lizardite (Aspiotis et al., 2023). The Raman Band or Shift at ~128 cm^{-1} is attributed to the doubly degenerate vibration E-mode and Raman Shift at ~206 cm^{-1} attributed to the Raman active symmetric A1-mode stretching style vibration of the SiO_4-tetrahedra crystal structure of four membered framework rings (Liu et al., 1997; Li et al., 2025). A Raman Shift at ~397 cm^{-1} in serpentine suggests the presence of the lizardite polymorph, which exhibits a characteristic peak in the silicate matrix (Bahram et al., 2019). The strong Raman Shift at ~465 cm^{-1} in silicate matrix is a characteristic vibrational mode resulting from the symmetric Si-O-Si stretching-bending within the silica ring structures (SiO_4-tetrahedra framework), indicating the presence of quartz crystal (Gillet et al., 1990). A weak Raman Shift at ~1166 cm^{-1} in the silicate structure can be accredited to the symmetric stretching vibration of (Si-O-Si) silicon-oxygen bonds, specifically from a non-bridging oxygen of silicate tetrahedra within a glass or silicate framework (McMillan, 1984). While prominent Si-O-Si stretching bands are typically in the 850–1150 cm^{-1} range, a peak at this specific wavenumber suggests a particular configuration of the silicate network structure (White and Minser, 1984).

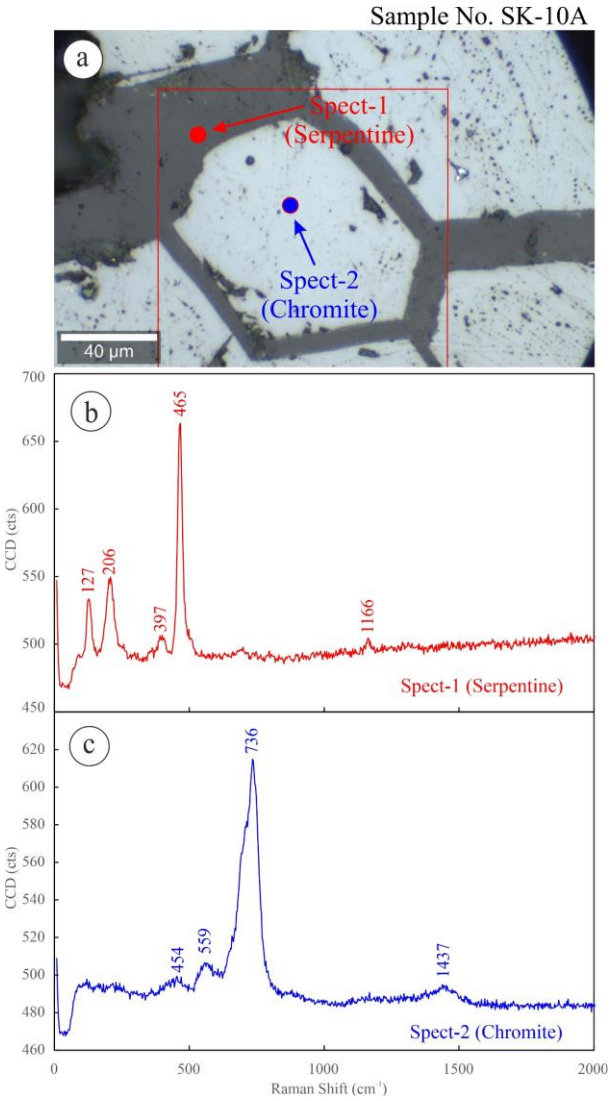

Figure 5. (a) Representative photomicrograph display chromite grain in the silicate phases or matrix of ultramafic rock. Characteristic Raman spectra of **(b)** silicate matrix (serpentine), and **(c)** chromite crystals in the silicate matrix of the ultramafic rock from the Asurabandha Chromite Mines in Dhenkanal district of Odisha.

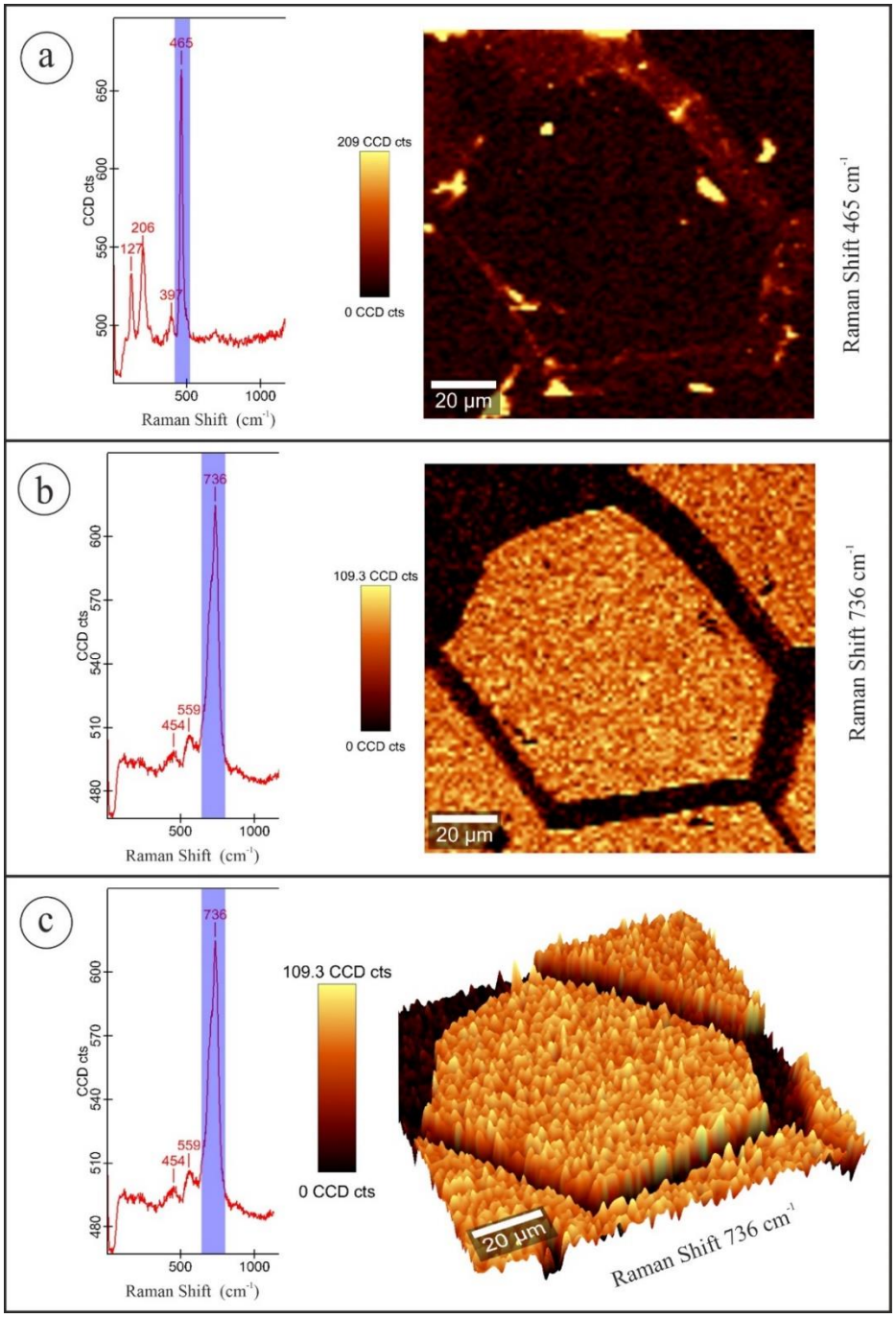

Figure 6. Laser Raman mapping of mineral phases in ultramafic rock from the Asurabandha Chromite Mines in Dhenkanal district of Odisha. **(a)** Raman spectrum of silicate matrix with 2D mapping over Raman Shift 465 cm^{-1}, **(b)** Raman spectrum of chromite crystal with 2D mapping over Raman Shift 736 cm^{1} and **(c)** Raman spectrum with 3D mapping over Raman Shift 736 cm^{-1} for euhedral chromite crystal in the ultramafic rock.

The white colour euhedral chromite crystal ($FeCr_2O_4$ or $FeO.Cr_2O_3$), is characterized by four significant Raman Shifts at approximately 454, 559, 736 and 1437 cm^{-1} (Figure 5c). A weak Raman Shift ~ 454 cm^{-1} in chromite is typically assigned to the E(g) vibrational modes, which are generally represents a minor Raman peak at lower wavenumbers compared to the strong A_1g mode at 680-730 cm^{-1} (Kharbish, 2018). The intensity and exact position of this Raman Shift are influenced by cation substitutions within the chromite's spinel lattice, particularly Fe^{3+} and Al^{3+} (Lughi et al., 2020). The presence of a Raman Shift ~559 cm^{-1} is typically attributed to the F_2g, may be due to impurities or the formation of chromium-bearing phases from the degradation of chromite, such as ferrian chromite (Reddy and Frost, 2005; Zhang and Gan, 2011) or manganese-substituted chromite (Ha et al., 2025). In the Raman spectrum of chromite, the most intense Raman Shift at

~736 cm^{-1} corresponds to the A_1g symmetric stretching mode of the Cr-O bonds within the octahedral groups (Nestola et al., 2014). Chromite is a solid solution with the spinel structure (AB_2O_4) where different cations (Fe^{2+}, Mg^{2+}, Cr^{3+}, Al^{3+}) can substitute for each other (Bosi et al., 2019). A very weak Raman Shift at ~1437 cm^{-1} is typically assigned to the carbonate (CO_3^{2-}) group that appears due to the symmetric stretching vibration mode (Gunasekaran et al., 2006), which indicates presence of carbonate rich mineral phases in the chromite crystals. Low-temperature, carbonate-rich fluids can alter chromite, a chromium-bearing mineral, into a hydrous chrome carbonate through chemical reactions that replace the original crystal structure in the ultramafic rocks (Klein and Garrido, 2011; Majumdar et al., 2016).

DISCUSSION

Chromite is an accessory mineral in mafic rocks but it becomes a dominant mineral in chromitite, often found in ultramafic rocks and coexists in serpentinites (Irvine, 1965; Burkhard, 1993). Chromite is the principal chromium ore, forming as an early-crystallizing mineral in ultramafic rocks like dunite, peridotite, and their secondary product as serpentinite within layered igneous complexes and ophiolites (Stowe, 1994). It occurs in various forms, such as disseminated grains, bands, lenses, and pockets. In Asurabandha chromite deposits, chromite grains are linked and compact, forming a mosaic, chain, or net-like texture in the ultramafic rock. The magmatic texture is the ultramafic rock where cumulus chromite grains form a dense, interconnected framework, and the inter-cumulus minerals (serpentine) fill the spaces between them, which is representative of adcumulate, heteradcumulate, and harrisitic-cumulate types (Wager et al., 1960). In general, cumulus texture in chromitite rocks signify to euhedral to subhedral chromite crystals that settle from a crystallizing magma, forming a framework that encloses later-crystallizing inter-cumulus minerals like serpentine, olivine, or pyroxene termed as heteradcumulate texture (Wager, 1959). Heteradcumulate textures in chromite are characterized by a rock composed almost entirely of poikilitic oikocrysts, which are larger crystals that enclose smaller, cumulus crystals, with little to no inter-cumulus matrix (Campbell, 1968; Hunter, 1996). These textures develop from in-situ crystallization within a boundary layer between a crystal mush and evolving magma. Their formation is favoured by a lack of cumulus seeds in the presence of supercooled magma (Barnes, 1986; Tegner and Wilson, 1995). Various types of cumulus textures are characteristic features of chromitite, a heteradcumulate texture consisting of chromite grains (oikocrysts) that enclose other cumulus minerals like olivine or pyroxene, which then crystallize within interstitial spaces (Campbell, 1978; Latypov et al., 2017). The heteradcumulate texture forms when larger chromite crystals grow from a supersaturated magma, capturing smaller, pre-existing minerals within their structure as they crystallize in place, rather than as a result of direct gravity-induced settling (Tait et al., 1984; Latypov et al., 2022).

Nucleation and crystal growth process is crucial in determining the magmatic texture and crystallization sequence of basaltic or ultramafic rocks, as the foreign surfaces reduce the supercooling or undercooling required for a stable crystal nucleus to form (Gray, 1970; Brandeis et al., 1984; Toramaru and Kichise, 2023). Crystal nucleation in basaltic magma involves the spontaneous formation of crystals or gas bubbles within the bulk of the liquid magma, without the help of existing surfaces or defects (Berkbile and Dowty, 1982; Polacci et al., 2018). Homogeneous and heterogeneous nucleation in basaltic magma involves solid crystals forming on the surfaces of seed grains, which is a more likely process than homogeneous nucleation due to the lower energy barrier (Lofgren, 1983; Gonnermann and Gardner, 2013; Shea, 2017). Common nucleation centres in natural basaltic magmas include other minerals (like pyroxene or olivine), suspended crystals, and even microscopic bubbles, significantly impacting the magma's behaviour during crystallization and evolution of igneous microstructures (Donaldson, 1979; Hersum and Marsh, 2006; Hammer et al., 2010). Euhedral chromite crystals can origin in ultramafic or basaltic magma, but their final appearance depends on the magma's cooling rate and stages of chemical differentiation (Holness et al., 2023). As one of the first minerals to crystallize in the ultramafic magma, chromite can be either euhedral, granular, nodular or dendritic (branching) depending on whether crystal growth is slow or rapid, which depends on the physical process of nucleation (Henry et al., 2024). Chromite crystallization occurs when a chromium-bearing mafic or ultramafic magma becomes immiscible system with olivine and pyroxene, and is heavily influenced by geochemical composition, oxygen fugacity, and the presence of other minerals (Roeder and Reynolds, 1991). As the magma cools, the liquidus of descent follows the chromite saturation surface, when chromium saturation is achieved in the ultramafic magma, it results in the crystallization of chromite (Murck and Campbell, 1986). At the early stage in the process of basaltic magma crystallization, the parental magma (often mafic or ultramafic) cools, leading to the crystallization of early-forming chromite crystals (Barnes, 1986; Latypov et al., 2022). The accumulation of these chromite crystals can form layers of chromitite, a type of rock composed almost entirely of chromite with minor silicate matrix between interstitial mineral grains.

Alteration of ultramafic rocks is primarily known as serpentinization, carbonation and metasomatism, the process where primary magnesium-rich minerals like olivine and

pyroxene are replaced by hydrous minerals, especially serpentine (Moody, 1976; McCollom and Bach, 2009; Klein et al., 2013). In general, serpentinization, which involves water-bearing fluids can lead to carbonation, silicification, that result production of hydrogen gas, impacting the rock's density, magmatic texture and primary mineralogy (Schwarzenbach et al., 2021; Hu et al., 2025). Carbonation of chromite during serpentinization involves the reaction of carbon dioxide (CO_2)-bearing fluids with serpentinized magmatic rocks, including those containing chromite, to form carbonate minerals like magnesite and/or dolomite (Klein et al., 2013; Huang et al., 2024). Formation of carbonate minerals due to carbonation process of chromite, typically occurring in mafic and ultramafic rocks, leads to changes in mineralogy and fluid chemistry (Klein and Garrido, 2011). As divalent cations in mafic and ultramafic rocks like magnesium, iron, and calcium bind with CO_2 results in the formation of carbonate minerals such as pyroaurite, stichtite and manasseite (Frondel, 1941). Carbonate-rich fluids cause chromite alteration by driving Mg-Fe exchange and Al loss, leading to the formation of iron-rich ferritchromite or ferrichromite and associated silicates like antigorite (Hodel et al., 2020; Eberhard et al., 2023). The specific conditions of the hydrothermal fluids, such as their temperature, pressure, and chemical composition, influence the type and extent of alteration encompass metasomatism, serpentinization and carbonation processes. The serpentinization and carbonation reactions are often associated with seafloor hydrothermal systems and subduction zones (Lowell and Rona, 2002; Deschamps et al., 2013). Alteration of ultramafic rocks lead to changes in the mineralogy, porosity, and chemical composition of the rocks, with potential effects on the solubility and redistribution of elements like chromium within the system (Oze et al., 2004; Shen et al., 2021). Serpentinization alters chemical composition of chromite crystal by reacting with carbonate-rich fluids, causing mineralogical changes like ferrichromite, pyroaurite, stichtite and can incorporate various trace elements (Sc, Ti, V, Ni, Mn, Co, and Zn) enrichment at earlier stages (Ulmer, 1974; Bara et al., 2014; Datta and Mondal, 2021; Liu et al., 2023).

In the Asurabandha chromite deposit, euhedral chromite crystals growth suggested that the magmatic conditions allow for uninhibited and sustained crystallization in a state of moderate super-saturation. This is more common in large, slow-cooling layered intrusions, to develop fully-formed crystal faces, chromite needs the right balance of heat, chemical supply, and physical space. Slow cooling rate provides sufficient time for the atoms of a mineral to migrate through the magma and systematically attach to the surfaces of a crystal growth. The surrounding magma must continuously resupply the elements needed to build the crystal structure of chromite, in this case, magnesium (Mg), iron (Fe), chromium (Cr) and aluminium (Al) supply from the magma. However, the Laser Raman-SNOM application with 2D (Figure 6a, b) and 3D mapping (Figure 6c) of chromite crystal from the Asurabandha deposits, indicates inhomogeneous or heterogeneous pattern observed in the chromite crystal structure. The chromite crystal is described as heterogeneous because its chemical composition is highly variable, and its internal crystal structure can be complex, possibly influenced by the crystallization conditions under which it formed or may be affected by hydrothermal alteration processes.

CONCLUSIONS

In Asurabandha deposits, chromite may be crystallized through heterogeneous nucleation in ultramafic magma, where new crystals grow on existing ones, resulting in aggregated or clustered textures. The crystal nucleation may be random rather than following a precise crystallographic alignment, further contributing to the heterogeneous distribution of the chromite crystal aggregates. This results in the heteradcumulate-like appearance where chromite crystals grown surrounded by silicate matrix. A chromite heteradcumulate texture is a type of igneous cumulate texture, where, large interlocking crystals of chromite (the cumulus minerals) enclose smaller, randomly oriented silicate crystals, such as olivine or pyroxene, that later altered to serpentine. The heteradcumulate texture observed in the Asurabandha chromite deposit inferred the specific arrangement where the cumulus minerals (chromite) have overgrown to enclose the inter-cumulus grains. The heteradcumulate texture of chromite crystal indicates a specific sequence of magma crystallization and evolution. Early crystallization, during the cooling of a magma, chromite begins to crystallize at a high temperature and accumulates to form a framework of crystals. Growth of surrounding crystals, the interstitial melt, trapped between the chromite grains, subsequently crystallizes to form silicate minerals like olivine or pyroxene.

In Asurabandha chromite deposits, presence of euhedral chromite crystal is a strong evidence that an individual grain of the mineral which crystallized without any interference, well-defined crystal faces reflect its inherent crystal structure. However, the Laser Raman-SNOM studies infer that the euhedral chromite phases are heterogenous with respect to internal crystal structure. The internal structure of chromite crystal and chemical composition are non-uniform. In chromite grain, heterogenous crystal structure are referring to primary characteristics with two distinct properties: (i) variable chemical composition in the crystal, and (ii) different processes of nucleation that favour crystal growth during crystallization in the magma. Compositional heterogeneity in the chromite crystal may appear because of trace element substitution during magmatic crystallization or secondary alteration processes.

Acknowledgements

The authors acknowledged to the Head of the Department, Department of Geology, Institute of Science, Banaras Hindu University (BHU) for providing necessary facilities. AG acknowledged the Council of Scientific & Industrial Research (CSIR), New Delhi, sponsored Junior Research Fellowship. DP acknowledged financial support from BHU Institute of Eminence (IoE) sponsored SEED Grant and Professional Development Fund (PDF).

Author credit statement

AG: Data curation, data analysis methodology, preparation of maps, editing and processing of complete data. This work is a part of his doctorate thesis, DP: conceptualization, data curation, quality checks, methodology, funding acquisition, draft editing and revision and supervision.

Data availability

Data is presented in the article.

Compliance with ethical standards

The authors declare that there is no conflict of interest and adhere to copyright norms.

References:

Arasada, R.C., Srinivasa Ra., G. and Sahoo, P.R., 2020. Integrated geological and geophysical studies for delineation of laterite covered chromiferous ultramafic bodies around Bhuban, southwestern part of Sukinda ultramafic complex, Odisha. Ore Geol. Rev., 119, 103402. https://doi.org/10.1016/j.oregeorev.2020.103402.

Ashwal., L.D. and Cairncross, B., 1997. Mineralogy and origin of stichtite in chromite-bearing serpentinites. Contrib. Mineral. Petrol., 127, 75-86.

Aspiotis, S., Schluter, J., Hildebrandt, F. and Mihailova, B., 2023. Raman spectroscopy for crystallochemical analysis of Mg-rich layered silicates: serpentine and talc. J. Raman Spectrosc., 54(12), 1502-1516.

Bahram, B., Hesam, M., Prakash, D. and Iris, W., 2019. Raman characteristics of Alpine–Himalayan serpentine polymorphs: A case study of Khankuie ultramafic complex, southeast of Iran. J. Earth Syst. Sci., 128, 238. https://doi.org/10.1007/s12040-019-1259-6.

Banerjee, P.K., 1972. Geology and Geochemistry of the Sukinda Ultramafic Field, Cuttack district, Orissa. Mem. Geol. Surv. Ind., 103, 1-320.

Barnes, S.J., 1986. The effect of trapped liquid crystallization on cumulus mineral compositions in layered intrusions. Contrib. Mineral. Petrol., 93, 524-531.

Barnes, S.J., 2000. Chromite in komatiites, II. modification during greenschist to mid-amphibolite facies metamorphism. J. Petrol., 41(3), 387-409.

Barra, F., Gervilla, F., Hernández, E., Reich, M., Padron-Navarta, J.A. and Gonzalez-Jimenez, J.M., 2014. Alteration patterns of chromian spinels from La Cabaña peridotite, south-central Chile. Miner. Petrol., 108, 819-836.

Behera, A. and Nayak, B., 2023. Metasomatic silicification of chromitite bodies in Asurabandha area, Odisha, India. J. Earth Syst. Sci., 138, 148. https://doi.org/10.1007/s12040-023-02167-1.

Berkebile, C.A. and Dowty, E., 1982. Nucleation in laboratory charges of basaltic composition. Am. Min., 67, 886-899.

Bersani, D. and Lottici, P.P., 2016. Raman spectroscopy of minerals and mineral pigments in archaeometry. J. Raman Spectrosc., 47, 499-530.

Bosi, F., Biagioni, C. and Pasero, M., 2019. Nomenclature and classification of the spinel supergroup. Eur. J. Mineral., 31, 183-192.

Brandeis, G., Jaupart, C. and Allegre, C.J., 1984. Nucleation, crystal growth and the thermal regime of cooling magmas. J. Geophys. Res., 89, B12, 10161-10177.

Burkhard, D.J.M., 1993. Accessory chromium spinels: their coexistence and alteration in serpentinites. Geochim. Cosmochim. Acta, 57, 1297-1306.

Campbell, I.H., 1968. The origin of heteradcumulate and adcumulate textures in the Jimberlana norite. Geol. Mag., 105(4), 378-383.

Campbell, I.H., 1978. Some problems with the cumulus theory. Lithos, 11, 311-323.

Datta, P. and Mondal, S.K., 2021. Compositional variations, thermometry, and probable parental magmas of Archean chromite from the Sargur greenstone belt, Western Dharwar Craton (India). Lithos, 380-381, 105867. https://doi.org/10.1016/j.lithos.2020.105867.

Deschamps, F., Godard, M., Guillot, S. and Hattori, K., 2013. Geochemistry of subduction zone serpentinites: A review. Lithos, 178, 96-127.

Donaldson, C.H., 1979. An experimental investigation of the delay in nucleation of olivine in mafic magma. Contrib. Mineral. Petrol., 69, 21-32.

Eberhard, L., Frost, D.J., McCammon, C.A., Dolejs, D. and Connolly, J.A.D., 2023. Experimental constraints on the ferric Fe content and oxygen fugacity in subducted serpentinites. J. Petrol., 64, 1-18.

Frondel, C., 1941. Constitution and polymorphism of the pyroaurite and sjogrenite groups. Am. Min., 26, 295-315.

Gillet, P., Cleach, A.L. and Madon, M., 1990. High-temperature Raman Spectroscopy of SiO_2 and GeO_2 polymorphs: anharmonicity and thermodynamic properties at high temperature. J. Geophys. Res. Solid Earth, 95, 21635-21655.

Gonnermann, H.M. and Gardner, J.E., 2013. Homogeneous bubble nucleation in rhyolitic melt: Experiments and nonclassical theory. Geochem. Geophys. Geosyst., 14, 4758-4773.

Gray, N.H., 1970. Crystal growth and nucleation in two large diabase dikes. Can. J. Earth Sci., 7(2), 366-375.

Gunasekaran, S., Anbalagan, G. and Pandi, S., 2006. Raman and infrared spectra of carbonates of calcite structure. J. Raman Spectrosc., 37, 892-899.

Ha, D.H., Noh, G., Kim, H., Kim, D.H., Kim, J., Jung, S., Hwang, C., Lee, H.Y., Yun, Y.J., Kwak, J.Y., Kang, K. and Yi, S.N., 2025. Raman spectroscopy study of K-birnessite single crystals. J. Mater. Chem. A, 13, 617. https://doi.org/10.1039/D4TA06118G.

Hammer, J.E., Sharp, T.G. and Wessel, P., 2010. Heterogeneous nucleation and epitaxial crystal growth of magmatic minerals. Geology, 38(4), 367-370.

Henry, H., Ceuleneer, G., Proietti, A., Kaczmarek, M.A., Chatelin, T. and De Parseval, P., 2024. How does nodular chromite nucleate and grow? an integrated microstructural and petrological approach. J. Petrol., 65, egae061. https://doi.org/10.1093/petrology/egae061.

Hersum, T.G. and Marsh, B.D., 2006. Igneous microstructures from kinetic models of crystallization. J. Volcan. Geoth. Res., 154, 34-47.

Hodel, F., Macouin, M., Trindade, R.I.F., Araujo, J.F.D.F., Respaud, M., Meunier, J.F., Cassayre, L., Rousse, S., Drigo, L. and Schorne-Pinto, J., 2020. Magnetic properties of ferritchromite and Cr-magnetite and monitoring of Cr-spinels alteration in ultramafic and mafic rocks. Geochem. Geophys. Geosyst., 21, e2020GC009227. https://doi.org/10.1029/2020GC009227

Holness, M.B., Vukmanovic, Z. and O'Driscoll, B., 2023. The formation of chromite chains and clusters in igneous rocks. J. Petrol., 64, 1-24.

Hope, G.A., Woods, R. and Munce, C.G., 2001. Raman microprobe mineral identification. Min. Eng., 14, 1565-1577.

Hu, Z., Qin, M., Xing, H., Wang, J., Jin, G., Tan, Y. and Yan, W., 2025. Effects of serpentinization and deserpentinization on rock elastic properties in subduction zones. Earth Sci. Rev., 263, 105069. https://doi.org/10.1016/j.earscirev.2025.105069.

Huang, Y., Okumura, S., Matsumoto, K., Takahashi, N., Tang, H., Wu, G., Tsujimori, T., Nakamura, M., Okamoto, A. and Li, Y., 2024. Experimental constraints on serpentinite carbonation in the presence of a H_2O–CO_2–NaCl fluid. Contrib. Mineral. Petrol., 179, 98. https://doi.org/10.1007/s00410-024-02175-4.

Hunter, R.H., 1996. Texture development in cumulate rocks. Developments in Petrology, 15, 77-101.

Irvine, T.N., 1965. Chromian spinel as a petrogenetic indicator, Part 1. Theory. Can. J. Earth Sci., 2, 648-672.

Keresztury, G., 2006. Raman Spectroscopy: Theory. In: Handbook of Vibrational Spectroscopy, pp 71-87. https://doi.org/10.1002/0470027320.s0109.

Kharbish, S., 2018. Raman spectroscopic features of Al- Fe^{3+}- poor magnesiochromite and Fe^{2+}- Fe^{3+}- rich ferrian chromite solid solutions. Miner. Petrol., 112, 245-256.

Klein, F. and Garrido, C.J., 2011. Thermodynamic constraints on mineral carbonation of serpentinized peridotite. Lithos, 126, 147-160.

Klein, F., Bach, W. and McCollom, T.M., 2013. Compositional controls on hydrogen generation during serpentinization of ultramafic rocks. Lithos, 178, 55-69.

Kraemer, D., Frei, R., Ernst, D.M., Bau, M. and Melchiorre, E., 2021. Serpentinization in the Archean and Early Phanerozoic – insights from chromium isotope and REY systematics of the Mg–Cr hydroxycarbonate stichtite and associated host serpentinites. Chem. Geol., 565, 120055. https://doi.org/10.1016/j.chemgeo.2020.120055.

Lafuente, B., Downs, R.T., Yang, H. and Stone, N., 2015. The power of databases: the RRUFF project. In: Highlights in Mineralogical Crystallography, T. Armbruster & R.M. Danisi, eds. Berlin, pp 1-30.

Latypov, R., Chistyakova, S. and Mukherjee, R., 2017. A novel hypothesis for origin of massive chromitites in the Bushveld Igneous Complex. J. Petrol., 58(10), 1899-1940.

Latypov, R., Christyakova, S., Barnes, S.J., Godel, B., Delaney, G.W., Cleary, P.W., Radermacher, V.J., Campbell, I. and Jakata, K., 2022. Chromitite layers indicate the existence of large, long-lived, and entirely molten magma chambers. Sci. Rep., 12, 4092. https://doi.org/10.1038/s41598-022-08110-6.

Li, J., Chou, I.M., Wang, X., Liu, Y., Han, Z. and Gao, J., 2025. Pressure sensor based on the Raman shift of the 128 cm^{-1} band of quartz for pressure measurements in hydrothermal diamond-anvil cells. Chem. Geol., 674, 122558. https://doi.org/10.1016/j.chemgeo.2024.122558.

Liu, L., Mernagh, T.P. and Hibberson, W.O., 1997. Raman spectra of high-pressure polymorphs of SiO_2 at various temperatures. Phys. Chem. Miner., 24, 396-402.

Liu, R., Zhao, J., Zhou, M. and Qi, H., 2023. Alteration of chromite during serpentinization of peridotites. Lithos, 460-461, 107385. https://doi.org/10.1016/j.lithos.2023.107385.

Lofgren, G.E., 1983. Effect of heterogeneous nucleation on basaltic textures: a dynamic crystallization study. J. Petrol., 24, 229-255.

Lowell, R.P. and Rona, P.A., 2002. Seafloor hydrothermal systems driven by the serpentinization of peridotite. Geophys. Res. Lett., 29(11), 1531, 261-264. https://doi.org/10.1029/2001GL014411.

Lughi, V., Lenaz, D., Bonifacio, A., Princivalle, F., Sergo, V. and Parisi, F., 2020. A Raman spectroscopy study of the oxidation processes in synthetic chromite $FeCr_2O_4$. Ceram. Int., 46, 29382-29387.

Majumdar, A.S., Hovelmann, J., Mondal, S.K. and Putnis, A., 2016. The role of reacting solution and temperature on compositional evolution during harzburgite alteration: Constraints from the Mesoarchean Nuasahi Massif (eastern India). Lithos, 256-257, 228-242.

McCollom, T.M. and Bach, W., 2009. Thermodynamic constraints on hydrogen generation during serpentinization of ultramafic rocks. Geochim. Cosmochim. Acta, 73, 856-875.

McMillan, P., 1984. Structural studies of silicate glasses and melts – applications and limitations of Raman spectroscopy. Am. Min., 69, 622-644.

McMillan, P.F., 1989. Raman spectroscopy in mineralogy and geochemistry. Ann. Rev. Earth Planet. Sci., 17, 255-283.

Mishra, S. and Gupta, S., 2013. Superposed deformation and inherited structures in an ancient dilational step-over zone: post-mortem of the Rengali Province, India. J. Structural Geol., doi: 10.1016/jsg.2013.11.004.

Moody, J.B., 1976. Serpentinization: a review. Lithos, 9, 125-138.

Murck, B.W. and Campbell, I.H., 1986. The effects of temperature, oxygen fugacity and melt composition on the behaviour of chromium in basic and ultrabasic melts. Geochim. Cosmochim. Acta, 50, 1871-1887.

Nestola, F., Periotto, B., Andreozzi, G.B., Bruschini, E. and Bosi, F., 2014. Pressure-volume equation of state for chromite and magnesiochromite: A single-crystal X-ray diffraction investigation. Am. Min., 99, 1248-1253.

Neuville, D.R., de Ligny, D. and Henderson, G.S., 2014. Advances in Raman spectroscopy applied to earth and material sciences. Rev. Min. Geochem., 78, 509-541.

Oze, C., Fendorf, S., Bird, D.K. and Coleman, R.G., 2004. Chromium geochemistry of serpentine soils. Int. Geol. Rev., 46(2), 97-126.

Pandit, D., 2024. Characterization of Sulphide Ore Minerals Using Combined Laser Raman with Scanning Near-field Optical Microscopy (SNOM). J. Sci. Res., 68(3), 1-5.

Polacci, M., Arzilli, F., La Spina, G., Le Gall, N., Cai, B., Hartley, M.E., Di Geneova, D., Vo, N.T., Nonni, S., Atwood, R.C., Llewellin, E.W., Lee, P.D. and Burton, M.R., 2018. Crystallisation in basaltic magmas revealed via in situ 4D synchrotron X-ray microtomography. Sci. Rep., 8, 8377. https://doi.org/10.1038/s41598-018-26644-6.

Raman, C.V., 1922. Molecular diffraction of light. University of Calcutta, pp 1-103. http://dspace.rri.res.in/handle/2289/2180.

Raman, C.V., 1923. The scattering of light by liquid and solid surfaces. Nature, 112, 281-282. https://doi.org/10.1038/112281a0.

Raman, C.V., 1927. The scattering of light in amorphous solids. J. Opt. Soc. Am., 15(4), 185-189. https://doi.org/10.1364/JOSA.15.000185.

Raman, C.V., 1928. A new radiation. Indian J. Physics, 2, 387-398. http://dspace.rri.res.in/handle/2289/2135.

Raman, C.V., 1929. The Raman effect: investigation of molecular structure by light scattering. Trans. Faraday Soc., 25, 781-792. https://doi.org/10.1039/TF9292500781.

Raman, C.V., 1942. Spectroscopic investigation of the solid and liquid states. Curr. Sci., 11, 225-227. http://dspace.rri.res.in/handle/2289/2199.

Raman, C.V., 1943. The vibration spectrum of a crystal lattice. Proc. Indian Acad. Sci. (Math. Sci.) 18, 237-250. https://doi.org/10.1007/BF03046531.

Raman, C.V., 1945. Scattering of light in crystals. Nature, 155, 396-397. https://doi.org/10.1038/155396a0.

Raman, C.V., 1947. The vibration spectra of crystals. Proc. Indian Acad. Sci., A26, 339-355. https://doi.org/10.1007/BF03170892.

Raman, C.V. and Krishnan, K., 1928. A new type of secondary radiation. Nature, 121, 501-502.

Reddy, B.J. and Frost, R.L., 2005. Spectroscopic characterization of chromite from the Moa-Baracoa Ophiolitic Massif, Cuba. Spectrochim. Acta, Part A 61, 1721-1728.

Rodgers, K.A., 1993. Routine identification of aluminium hydroxide polymorphs with the Laser Raman Microscope. Clay Minerals, 28, 85-99.

Roeder, P.L. and Reynolds, I., 1991. Crystallization of chromite and chromium solubility in basaltic melts. J. Petrol., 32, 909-934.

Saha, A.K., 1994. Crustal evolution of Singhbhum north Orissa, Eastern India. Mem. Geol. Soc. India 27, 1-341.

Sahoo, K.C., 2014. PGE exploration in Odisha: an overview. Indian J. Geosci., 83, 31-37.

Santti, J., Kontinen, A., Sorjonen-Ward, P., Johanson, B. and Pakkanen, L., 2006. Metamorphism and chromite in serpentinized and carbonate-silica-altered peridotites of the Paleoproterozoic Outokumpu-Jormua Ophiolite Belt, eastern Finland. Int. Geol. Rev., 48(6), 494-546.

Schwarzenbach, E.M., Vogel, M., Fruh-Green, G.L. and Boschi, C., 2021. Serpentinization, carbonation, and metasomatism of ultramafic sequences in the Northern Apennine Ophiolite (NW Italy). J. Geophys. Res. Solid Earth, 126, e2020JB020619. https://doi.org/10.1029/2020JB020619.

Shea, T., 2017. Bubble nucleation in magmas: A dominantly heterogeneous process? J. Volcan. Geoth. Res., 343, 155-170. http://dx.doi.org/10.1016/j.jvolgeores.2017.06.025.

Shen, J., Wang, S.J., Qin, L., Ni, H., Li, S., Du, J., Shen, T., Zhang, L. and Yu, H., 2021. Tracing serpentinite dehydration in a subduction channel: chromium element and isotope evidence from subducted oceanic crust. Geochim. Cosmochim. Acta, 313, 1-20. https://doi.org/10.1016/j.gca.2021.06.030.

Singh, A.K. and Pandit, D., 2025. Petrography and Laser Raman Characterization of Banded Hematite Jasper from Agori Formation of Mahakoshal Greenstone Belt. J. Scientific Res., 69, 1-7.

Stowe, C.W., 1994. Compositions and tectonic settings of chromite deposits through time. Econ. Geol., 89, 528-546.

Tait, S.R., Huppert, H.E. and Sparks, R.S.J., 1984. The role of compositional convection in the formation of adcumulate rocks. Lithos, 17, 139-146.

Tegner, C. and Wilson, J.R., 1995. Textures in a poikilitic olivine gabbro cumulate: evidence for supercooling. Min. Petrol., 54, 161-173.

Toramaru, A. and Kichise, T., 2023. A new model of crystallization in magmas: Impact of pre-exponential factor of crystal nucleation rate on cooling rate exponent and log-linear crystal size distribution. J. Geophys. Res. Solid Earth, 128, e2023JB026481. https://doi.org/10.1029/2023JB026481.

Tripathy, A.K., Sahoo, K.C., Abhilash, P.K., Chandhury, T., Kar, R.N., Mohanthy, M. and Das, M., 2014. PGE - bearing Chromite cumulates from boninitic ultramafic parentage in Bhuban ultramafic complex (BUC), Odisha. Indian J. Geosci., 68 (2), 223-236.

Ulmer, G.C., 1974. Alteration of chromite during serpentinization in the Pennsylvania-Maryland district. Am. Min., 59, 1236-1241.

Vandenabeele, P., 2013. Practical Raman Spectroscopy - An Introduction. John Wiley & Sons, Ltd. DOI:10.1002/ 9781119961284.

Wager, L.R., 1959. Differing powers of crystal nucleation as a factor producing diversity in layered igneous intrusions. Geol. Mag., 96, 75-80.

Wager, L.R., Brown, G.M. and Wadsworth, W.J., 1960. Types of igneous cumulates. J. Petrol., 1(1), 73-85.

White, W.B. and Minser, D.G., 1984. Raman spectra and structure of natural glasses. J. Non-Cryst. Solids, 67, 45-59.

Zhang, Z.W. and Gan, F.X., 2011. Analysis of the chromite inclusions found in nephrite minerals obtained from different deposits using SEM-EDS and LRS. J. Raman Spectrosc., 42(9), 1808-1811.

Received on: 7-10-2025; Revised on: 25-1-2026; Accepted on: 30-01-2026

J. Ind. Geophys. Union, 30(2) (2026), 114-121
https://doi.org/10.71122/JIGU.30(2)2026.0012

Abundance, distribution pattern and health risk assessment of polycyclic aromatic hydrocarbons in size-segregated aerosols during Diwali festival in Delhi (India)

Nisha Rani[1,2] and Monika J. Kulshrestha*[1,2]
[1]CSIR-National Physical Laboratory, Dr. K.S. Krishnan Marg, New Delhi-110012, India
[2]Academy of Scientific and Innovative Research (AcSIR), Ghaziabad-201002, India
*Corresponding Author: monikajk@yahoo.com

ABSTRACT

Size-segregated aerosol samples were collected in Delhi during the Diwali festival (3-5 November, 2021) to evaluate Polycyclic Aromatic Hydrocarbons (PAHs) concentrations, molecular distribution, sources, and associated health risk. 3 samples (each with nine size ranges) were collected using an eight-stage Andersen cascade impactor, i.e., before-Diwali (BD), Diwali day (DD), and after-Diwali (AD). The ∑PAHs concentrations across different aerosol size fractions were in the range 1.2-147.4 ng/m³, with a sharp spike on Diwali day, and remained high in the after-Diwali sample. The nine size ranges were classified into submicron ($PM_{<0.43-1.1}$), fine ($PM_{1.1-2.1}$), and coarse ($PM_{2.1->9}$) fractions. Submicron fraction dominated PAHs loading (61.4%), followed by coarse (21.0%) and fine (17.6%) fractions. Naphthalene, benzo[b]fluoranthene, and Chrysene were observed to be the most abundant PAHs. The lognormal size distribution was bimodal, with peaks in the submicron and coarse fractions. Molecular diagnostic ratios indicated firecracker burning, vehicular emissions, coal/biomass burning, and cooking as the dominant PAHs sources. Inhalation cancer risk assessment revealed significantly higher carcinogenic risk in the submicron fraction, with risk exceeding acceptable limits by several orders of magnitude on Diwali day, underscoring the severe health implications of festival-related emissions.

Keywords: Diwali; Size-segregated aerosols; Polycyclic Aromatic Hydrocarbons (PAHs); Size distribution; Molecular Diagnostic Ratios; Health risk assessment

INTRODUCTION

Diwali is one of the main festivals in India and is celebrated with widespread cultural activities, including decorating houses with lights, lighting diyas/candles, and performing Goddess Lakshmi pooja, along with intense firecracker burning for a very short duration (Rastogi et al., 2019). Several studies have reported abrupt spikes in fine and coarse particulate matter, gaseous pollutants, and a wide range of inorganic and organic compounds due to firecracker burning during this period, indicating the short-lived, but strong impact of firecracker emissions on urban air quality (Kulshrestha et al., 2004; Singh et al., 2016; Kumar et al., 2020; Rani et al., 2023). Previous studies have also emphasized the health implications during such short-term episodic events (Chandu et al., 2023; Kumar et al., 2023). PAHs are ubiquitous organic compounds composed of two or more fused aromatic rings, and many are strong carcinogens and mutagens. PAHs are primarily formed by incomplete combustion and pyrolysis of carbonaceous fuels, as well as by the evaporation of petroleum products (Shen et al., 2012). Epidemiological and toxicological studies indicate that long-term exposure to particle-bound PAHs, even at low levels, can increase risks of lung cancer, DNA damage, and respiratory problems, while short-term exposure during pollution episodes can aggravate asthma and other acute health outcomes (Kim et al., 2013). Therefore, PAHs are categorised as persistent organic pollutants, and understanding their atmospheric levels, sources, and size distributions is critical for protecting air quality and human health.

In India, Diwali-related size-segregated aerosol studies have examined various particulate components, including water-soluble ions, trace metals, elemental and organic carbon, and selected organic marker compounds (Rastogi et al., 2019; Mahilang et al., 2020). Regarding PAHs, many studies have examined PM_{10}- and $PM_{2.5}$-associated PAHs during the Diwali festival (Sarkar et al., 2010; Perrino et al., 2011; Kurwadkar et al., 2023). But there is a scarcity of research examining the distribution of PAHs across different particle size ranges during Diwali, despite the fact that particle size governs both the lifetime and respiratory deposition of particulate matter (PM). Possibly no previous study has quantified particle-bound PAHs in size-segregated aerosols during the Diwali festival in Delhi. The present study addresses this gap by elucidating their molecular and size distributions and associated human health risks.

METHODOLOGY

Study area

Delhi, the capital of India, is situated in the upper Indo-Gangetic Plain. It is one of the world's most polluted cities, especially in the Indo-Gangetic Plain, primarily due to its location and dense population (World Air Quality Report, 2024). Size-segregated aerosol sampling for this study was carried out at CSIR-National Physical Laboratory located in central Delhi (28°37′52″ N, 77°10′01″ E). The site is surrounded by agricultural fields, forest areas, residential and institutional areas, commercial centres, and a nearby major road, which contributes to vehicular emissions (Singh and Kulshrestha, 2024; Rani and Kulshrestha, 2025). Figure 1 shows the location of the sampling site.

Size-segregated aerosol collection

Size-segregated aerosol samples were collected using an 8-stage Andersen Cascade Impactor (ACI; TISCH), which

was mounted on the rooftop of CSIR-National Physical Laboratory, at ~15 m above ground level. The impactor had a constant flow rate of 28.3 L min^{-1}, monitored with a dry gas meter (ITRON). The aerodynamic cut-off diameters of impactor stages were <0.43, 0.65, 1.1, 2.1, 3.3, 4.7, 5.8, and >9.0 µm. Three sets of size-segregated aerosol samples were collected: before-Diwali (03-11-2021), Diwali Day (04-11-2021), and after-Diwali (05-11-2021), each with a sampling duration of 23 hours (10:30 AM - 9:30 AM of the next day). Quartz microfiber filters (Whatman, 82.6 mm diameter) were used for collecting samples in different size ranges, with a backup filter (81 mm) placed downstream of the final stage to capture remaining particles. All filters were pre-baked at 400 °C for 4 h to remove any organic contamination.

Chemical analysis

To analyse the chemical composition of size-segregated aerosol samples, the solvent extraction method was employed. 3/4 of each filter was extracted with a solvent mixture of acetone and dichloromethane (1:1 by volume). The filters in the solvent mixture were subjected to ultrasonic extraction at ~40°C for three consecutive cycles of one hour each. Initially, the liquid extract was concentrated to 2 mL using a Kuderna-Danish apparatus, then reduced to 1 mL by using high-purity nitrogen. The samples were stored in a refrigerator until further chemical analysis. PAHs in the size-segregated aerosols were quantified using a Gas Chromatograph- Mass Spectrometer (GC-MS, Shimadzu QP2020) with a Rxi-5MS capillary column (30 m × 0.25 mm internal diameter). Helium was used as the carrier gas for the transport of vapourised compounds in GC-MS. 1 µL of sample was injected in splitless mode, with the injector temperature set to 280°C. The oven temperature was initially held at 50°C for 3 minutes, then increased to 150°C at 20°C/min (held for 3 minutes), and finally raised to 280°C at 4°C/min (held for 47 minutes). The MS was operated in electron impact ionisation mode at 70 eV, with source and interface temperatures maintained at 225°C and 300°C, respectively. A total of 18 PAHs were quantified i.e., naphthalene (Nap), 1-methylnaphthalene (1-MNap), 2-methylnaphthalene (2-MNap), acenaphthylene (Acy), acenaphthene (Ace), fluorene (Flu), phenanthrene (Phe), anthracene (Ant), fluoranthene (Flt), pyrene (Pyr), benz[a] anthracene (BaA), chrysene (Chry), benzo[b]fluoranthene (BbF), benzo[k]fluoranthene (BkF), benzo[a]pyrene (BaP), dibenz[a,h]anthracene (DaA), benzo[ghi]perylene (BghiP), and indeno[1,2,3-cd]pyrene (InP). PAHs quantification was performed using the internal standard method, which compensates for slight fluctuations in the instrument's response to each compound. The internal standard deuterated n-tetracosane (C24D50) was added to all calibration standards and samples. 9-point calibration curves (0.001, 0.005, 0.01, 0.05, 0.1, 0.5, 1, 2, 5 ppm) were plotted for most PAHs, while 7-point calibration curves for BaP and InP, and 5-point calibration curves for DaA, all exhibited high linearity ($R^2 \geq 0.99$). Analyte concentrations were calculated using relative response factors based on the ratios of analyte to internal standard peak areas and their corresponding concentration ratios. The analytical method detection limits (MDLs) were experimentally derived and ranged from 0.0001 µg/mL to 0.05 µg/mL. The filter blanks were extracted and analysed for PAHs as with the samples. All PAHs in the blanks were observed below detection limits. The recovery efficiency was ~98%.

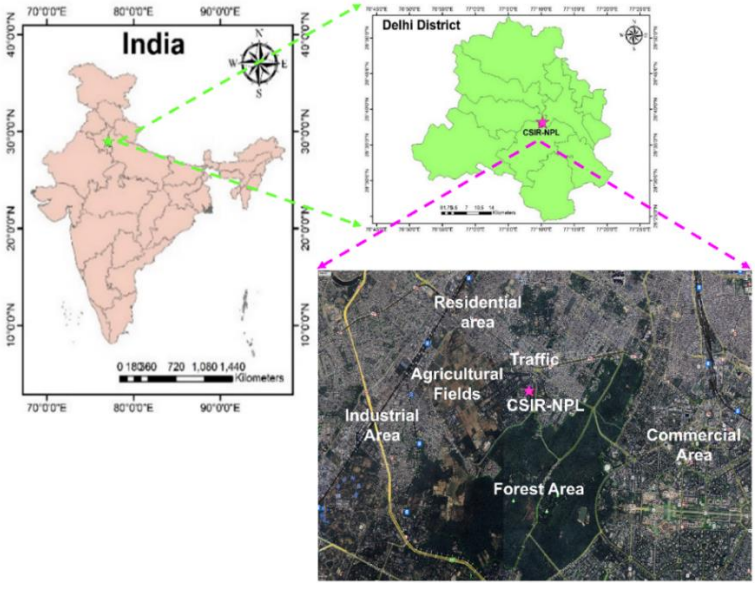

Figure 1. Location of study site in New Delhi (India)

Respiratory health risk assessment

The International Agency for Research on Cancer has classified several PAHs as carcinogenic, including BaA, BbF, DaA, and InP, in addition to BaP (https://monographs.iarc.who.int/list-of-classifications). Carcinogenic potential of total PAHs was estimated using Toxic Equivalency Quotient (TEQ). TEQ was determined by multiplying the concentration of each individual PAH (PAH_i) by its respective toxic equivalent factor (TEF_i) as follows:

$$TEQ = \sum_i PAH_i \times TEF_i$$

The TEF values for different PAHs are provided in **Table 1**. Inhalation Cancer Risk (ICR) for lungs associated with PAHs' exposure was determined using the equation:

$$ICR = TEQ \times UR_{BaP}$$

where UR_{BaP} signifies the unit risk factor related to BaP. The calculation was performed assuming a lifetime exposure duration of 70 years, in accordance with the EPA recommendations for inhalation cancer risk assessment (EPA, 2005). As per epidemiological research on coke-oven workers, BaP inhalation has been linked to a lung cancer risk of 8.7×10^{-5} per ng/m³ (WHO, 2000). Accordingly, the value of 8.7×10^{-5} per ng/m³ was used as unit risk in the present assessment.

RESULTS AND DISCUSSION

Total PAHs in size-segregated aerosols

The ∑PAHs concentrations across different aerosol size fractions were observed in the range of 1.2-147.4 ng/m³ during the Diwali festival (Figure 2). The ∑PAHs levels varied between 1.2-11.2 ng/m³ in the before-Diwali sample, while a sudden spike was observed in the sample on Diwali day, with concentrations ranging from 22.0-147.4 ng/m³. In the after-Diwali sample, concentrations decreased in all size fractions (6.6-106.7 ng/m³) compared to Diwali day, except in the 3.3-4.7 μm size range, where a slight increase was observed. But the levels in the after-Diwali sample remained higher than those in the before-Diwali samples. Among all the size fractions, coarse showed less variation, while submicron and fine showed significant variation, which could be attributed to the preferential association of PAHs with fine particles. The submicron fraction was the dominant carrier of PAHs, comprising 61.4% of the total PAHs mass, with the fine and coarse fractions contributing 17.6% and 21.0%, respectively, during the study period. A multi-site study conducted in Jamshedpur during the COVID-19 pandemic revealed similar results, with the lowest total PAHs concentrations on the pre-Diwali day, followed by a marked elevation during Diwali festival days.

Table 1. Toxic Equivalent Factor of individual PAHs (Source: Nisbet and Lagoy, 1992)

Compounds	TEF
Naphthalene	0.001
Naphthalene, 2-methyl	0.001
Acenaphthylene	0.001
Acenaphthene	0.001
Fluorene	0.001
Phenanthrene	0.001
Anthracene	0.01
Fluoranthene	0.001
Pyrene	0.001
Benz[a]anthracene	0.1
Chrysene	0.01
Benzo[b]fluoranthene	0.1
Benzo[k]fluoranthene	0.1
Benzo[a]pyrene	1
Indeno[1,2,3-cd]pyrene	0.1
Dibenz(a,h)anthracene	1
Benzo[ghi]perylene	0.01

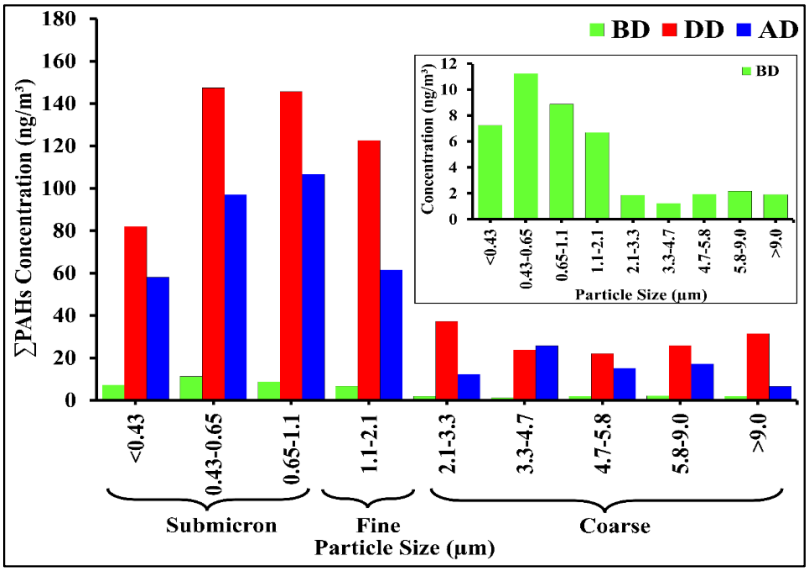

Figure 2. Total PAHs in different size ranges of aerosols during Diwali festival (Inset: BD sample). BD: before-Diwali, DD: Diwali day, AD: after-Diwali

The elevated PAHs levels on Diwali Day 1 and Diwali Day 2 were primarily attributed to firework combustion, local biomass burning, and industrial emissions (Kurwadkar et al., 2023). Earlier studies at Delhi, Tianjin, and Nanjing also reported vehicular emissions as the chief sources of PAHs during firework festivals (Sarkar et al., 2010; Shi et al., 2014; Kong et al., 2015).

Molecular distributions of PAHs

18 PAHs were quantified in size-segregated aerosol samples during the Diwali festival. Molecular distribution of PAHs in before-Diwali, Diwali day, and after-Diwali samples is shown in Figure 3. Nap was the most abundant PAH, followed by BbF and Chry in all three samples. However, their levels were several times higher on Diwali day and after-Diwali samples than in before-Diwali samples. Higher levels of BaP, InP, BghiP, Flt, Pyr, Flu, and Phe were also observed in Diwali day and after-Diwali samples. Nap is produced from various combustion-related activities, including industrial operations, vehicle exhaust, cigarette and biomass (wood and grass) burning, incomplete combustion of petroleum products, cooking, and coal combustion (Jia and Batterman, 2010). BbF is associated with diesel and coal combustion, while BaP and Chry arise from traffic emissions, and the combustion of organic materials such as wood and crop residues (Ren et al., 2017). BaP, InP, BghiP, Flt, Pyr, Flu, and Phe also originate from vehicular emissions, fossil fuel combustion, biomass burning, and cooking activities (Ray et al., 2017).

The main sources of high PAHs levels during the Diwali festival include increased vehicular emissions from people moving to meet family/friends and to do shopping, biomass/waste burning as people tend to deep-clean their houses during Diwali, cooking, and coal combustion. Ring-wise distribution showed the overall dominance of 4- and 5-ring PAHs (~50%) across all three days, with the highest levels in the Diwali day sample. On Diwali day, the Lakshmi pooja is often accompanied by a hawan (worship of fire), in which materials such as wood, ghee (clarified butter), camphor, incense sticks, etc., are burned, leading to the emission of high concentrations of 3-, 4-, and 5-ring PAHs (Dewangan et al., 2014). This prevalence is of particular toxicological importance because these HMW compounds are known to exhibit mutagenic and carcinogenic properties (Kulshrestha et al., 2019). An earlier study on PAHs in Delhi during the Diwali festival also reported the highest levels of 5-ring PAHs, i.e., BbF, BaP, DaA, and BkF (Sarkar et al., 2010). Higher levels of Nap at Tianjin on Chinese New Year's Eve were also attributed to cooking sources, as festival periods are characterized by more elaborate cooking preparations than on regular days, leading to a proportionally higher contribution from cooking-related emissions during these occasions (Shi et al., 2014). Firecracker burning also substantially contributes to atmospheric PAHs loading by thermally degrading organic matrix materials, including paper coverings, wooden frames, and organic binders, which undergo pyrolysis at elevated temperatures, releasing PAHs that subsequently partition onto submicron particles. Research conducted in Nanjing demonstrated that extensive firework combustion on Chinese New Year's Eve substantially elevated PAHs' mass concentrations, with a particularly pronounced increase observed for higher-molecular-weight PAH species (Kong et al., 2015).

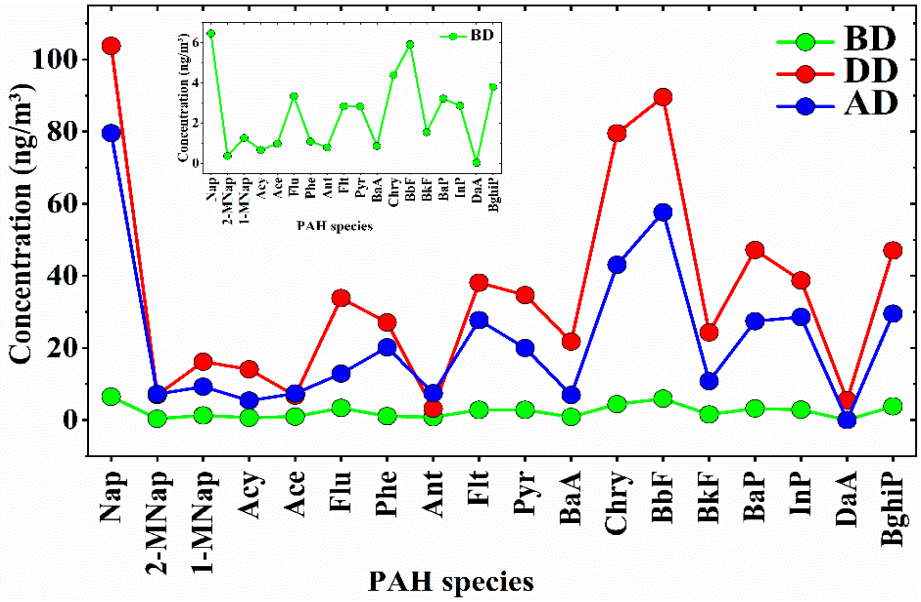

Figure 3. Molecular distribution of PAHs in BD, DD and AD samples (Inset: BD sample). BD: before-Diwali, DD: Diwali day, AD: after-Diwali

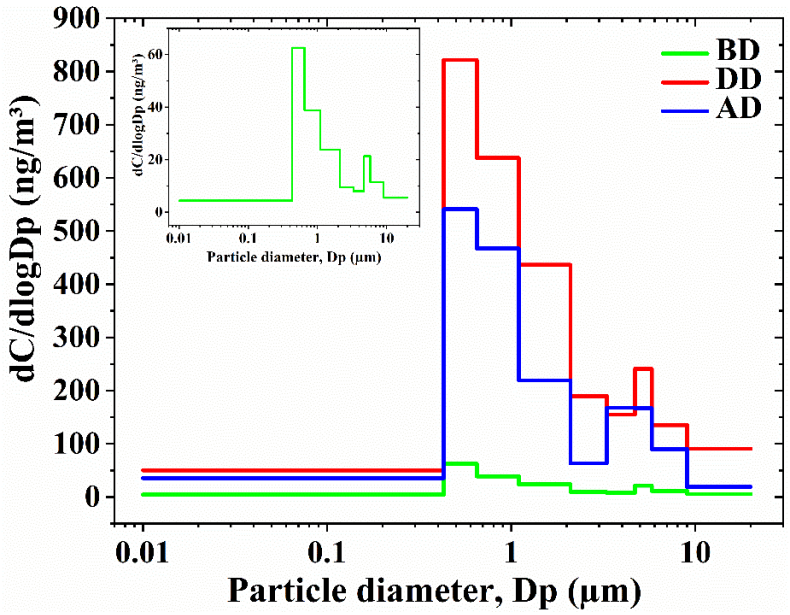

Figure 4. Lognormal size distribution of total PAHs in BD, DD and AD samples (Inset: BD sample). BD: before-Diwali, DD: Diwali day, AD: after-Diwali

Lognormal size distribution of PAHs

The lognormal size distribution of ∑PAHs across size-segregated aerosols during the Diwali festival is shown in Figure 4. ∑PAHs exhibited a bimodal size distribution in all samples, with distinct concentration peaks in the submicron fraction (0.43-0.65 µm) and the coarse fractions (3.3-4.7 and 4.7-5.8 µm). In all the samples, the submicron fraction showed significantly higher PAHs loading than the coarse fraction. The Diwali day sample showed the most pronounced PAHs peak in the submicron fraction, with levels ~13 times higher than before-Diwali and ~1.5 times higher than after-Diwali samples. These observations reflect rigorous anthropogenic contributions from multiple combustion and thermal emissions occurring simultaneously, including cooking, lighting activities (candles/diyas/oil lamps), firecracker burning, and increased vehicular emissions (Orecchio, 2011; Hossain and Salehuddin, 2012; Kong et al., 2015). Fossil fuel combustion in vehicles produces PAHs, which undergo gas-to-particle conversion, leading to preferential accumulation in the submicron fraction (Sicre et al., 1990).

Molecular diagnostic ratios (MDRs) of PAHs

MDRs were applied to detect probable PAHs sources in size-segregated aerosols during Diwali. **Table 2** shows the source value ranges and average values of MDRs in the before-Diwali, Diwali day, and after-Diwali samples. The ANT/(ANT+PHE) ratios of 0.42, 0.11, and 0.27 in before-Diwali, Diwali day, and after-Diwali samples showed pyrogenic signatures, such as firecracker burning, which were the main contributors to atmospheric PAHs loading (Han et al., 2011). The FLT/(FLT+PYR) ratios in before-Diwali (0.50), Diwali day (0.52), and after-Diwali (0.58) samples showed a continuous influence of coal and biomass combustion during the Diwali episode (Han et al., 2011). The FLU/(FLU+PYR) ratio showed diesel emissions in the before-Diwali (0.54) sample, while gasoline emissions were dominant in the Diwali day (0.49) and after-Diwali (0.39) samples, indicating intensified vehicular traffic during the period (Ravindra et al., 2008). The BaA/(BaA+Chry) ratio was <0.2 in before-Diwali and after-Diwali samples, reflecting petroleum and petrogenic contributions, while it was 0.21 in the Diwali day sample, signifying liquid fossil-fuel, vehicle, and crude oil combustion on the highest emission day (Nezhad et al., 2023). The BaP/BghiP ratios in before-Diwali (0.85), Diwali day (1.00), and after-Diwali (0.93) samples showed a consistently high traffic contribution across all days, reflecting vehicular emissions as a consistent PAHs' source even in the presence of episodic combustion events (Tobiszewski and Namiesnik, 2012). The ΣLMW/ΣHMW ratios in before-Diwali (0.53), Diwali day (0.50), and after-Diwali (0.59) samples indicated pyrogenic dominance, underscoring combustion processes as the main source of PAHs mass across all sampling stages, with intensification evident during Diwali Day (Hazarika et al., 2019).

Overall, MDRs identified combustion as the dominant PAHs source throughout the Diwali episode, with firecracker burning, coal/biomass burning, cooking, and vehicular traffic jointly contributing to atmospheric PAHs loading. Earlier studies employing MDRs on PM_{10} and $PM_{2.5}$ samples from different locations in Delhi, and Jamshedpur, Jharkhand, during the Diwali festival similarly attributed coal combustion, vehicular emissions, and biomass/wood burning as the major contributors to atmospheric PAHs' concentrations (Sarkar et al., 2010; Kurwadkar et al., 2023). In urban and rural locations across China, investigations conducted during firework-intensive festival periods including the Chinese Spring Festival and Chinese New Year, identified coal combustion, vehicular emissions, and biomass burning as the principal PAHs sources in $PM_{2.5}$ aerosols, whereas fireworks were not explicitly attributed as direct PAHs' contributors in those studies (Kong et al., 2015; Zhang et al., 2019).

Table 2. Probable source estimation of PAHs using molecular diagnostic ratios as reported in previous studies. BD: before Diwali, DD: Diwali day, AD: after Diwali

PAH Ratio	Value range, Source	References	BD	DD	AD
ANT/ (ANT+PHE)	<0.1 Petrogenic >0.1 Pyrogenic	Han et al. (2011)	0.42	0.11	0.27
FLT/ (FLT+PYR)	<0.4 Petrogenic 0.4-0.5 Liquid fossil fuel combustion >0.5 Coal biomass combustion	Han et al. (2011)	0.50	0.52	0.58
FLU/ (FLU+PYR)	<0.5 Gasoline emission >0.5 Diesel emission	Ravindra et al. (2008)	0.54	0.49	0.39
BaA/ (BaA+Chry)	<0.2 Petroleum & Petrogenic 0.2-0.35 Liquid fossil fuel, vehicle and crude oil combustion >0.35 Coal, grass, and wood combustion	Nezhad et al. 2023	0.16	0.21	0.14
BaP/BghiP	<0.6 non-traffic emissions >0.6 Traffic emissions	Tobiszewski and Namiesnik (2012)	0.85	1.00	0.93
ΣLMW/ΣHMW	<1 Pyrogenic >1 Petrogenic	Hazarika et al. (2019)	0.53	0.50	0.59

Table 3. TEQ and ICR values of PAHs in size-segregated aerosols during Diwali. BD: before Diwali, DD: Diwali day, AD: after Diwali

Day	TEQ			ICR		
	SM	F	C	SM	F	C
BD	3.5	0.8	0.2	3.019E-04	6.809E-05	1.898E-05
DD	50.5	16.9	4.3	4.396E-03	1.468E-03	3.710E-04
AD	31.0	6.7	1.0	2.701E-03	5.867E-04	8.694E-05

Respiratory health risk assessment

TEQ and ICR values, calculated across the three aerosol size fractions, are presented in **Table 3**. An inverse relationship between particle size and TEQ values was observed on all days, with fine fractions demonstrating substantially higher carcinogenic potency than coarser fractions (Ren et al., 2017). The Diwali day sample showed the highest TEQ values across all size fractions, followed by the after-Diwali and before-Diwali samples. Similar observations with high TEQ values in $PM_{2.5}$ were reported in Shandong and Henan Provinces, China, during the Chinese New Year festival period. Average ∑TEQ concentrations at multiple locations (range: 15.40-35.48 ng/m³) significantly exceeded China's BaP regulatory standard of 2.5 ng/m³ (24-hour average) by ~6-14 times (Zhang et al., 2019). ICR values of 10^{-6} signify an acceptable low risk, 10^{-5} denote medium risk, and 10^{-4} show high risk levels. The values for coarse and fine fractions remained in the medium to high cancer risk category throughout the episode. But the submicron fraction, being the smallest and most penetrating aerosol fraction, showed the highest risk. The high carcinogenic potential was due to the preferential association of toxic PAHs with the finest aerosol fraction. The calculated submicron ICR value of 4.396×10^{-3} on Diwali day indicates that ~4,396 people in one million individuals may develop cancer under continuous long-term (70-year) exposure conditions (EPA, 2005). This value significantly exceeded the acceptable limit of 1×10^{-6} specified by the United States Environmental Protection Agency (USEPA, 1991). Zhang et al. (2019) documented maximum ICR values in the adult age group (30-70 years), indicating that adults experienced more cancer risk compared to other age categories. In Nanjing, also, considerably high carcinogenic risks from PAHs were reported on Chinese New Year celebration days, necessitating the urgent implementation of emission-reduction policies explicitly focusing on firework combustion during the festival period (Kong et al., 2015).

CONCLUSIONS

Total PAHs levels showed a spike on Diwali Day across all size fractions. However, the largest contribution of ∑PAHs mass was observed in the submicron fraction. Molecular distributions, size distributions, and diagnostic ratios of PAHs indicated the presence of diversified sources, i.e., firecracker burning, vehicular emissions, lighting activities (candles/diyas/oil lamps), coal/biomass burning, and cooking. The predominance of 4- and 5-ring PAHs, along with high ICR values, especially in submicron and fine fractions, indicated a high carcinogenic burden associated with short-term festival activities. Cancer risks on Diwali Day far exceeded acceptable levels, underscoring the need for targeted control measures, promoting low-emission celebrations, issuing public advisories, especially for sensitive groups (children, elderly, patients), and stringent management of fireworks and other combustion sources during major festivals in highly polluted urban regions.

Acknowledgements

The authors are highly grateful to the Director, CSIR-NPL, New Delhi, for providing the necessary facilities to carry out this research through OLP-210332 funds. Nisha Rani is thankful to the University Grants Commission (UGC), New Delhi, for providing financial support through a Senior Research Fellowship (SRF).

Authors credit statement

Nisha Rani: Data curation, formal analysis, investigation, writing- original draft.

Monika J. Kulshrestha: Funding acquisition, Methodology, Project administration, Resources, Supervision, Validation, Writing- review and editing, Conceptualization.

Data availability

The datasets generated during and/or analysed during the current study are not publicly available due to unpublished data, but are available from the corresponding author on reasonable request.

Compliance with ethical standards

The authors have no relevant financial or non-financial interests to disclose and adhere to copyright norms.

References

Chandu, K., Raju, A.D., Kumar, S.V.J. and Mahendra, N., 2023. Spatial variations in PM2. 5/PM10 over time in Andhra Pradesh, India. J. Ind. Geophys. Union, 27(3), 211-220.

Dewangan, S., Pervez, S., Chakrabarty, R. and Zielinska, B., 2014. Uncharted sources of particle bound polycyclic aromatic hydrocarbons from South Asia: Religious/ritual burning practices. Atmosph. Pollution Res., 5(2), 283-291.

EPA, 2005. US, Guidelines for Carcinogen Risk Assessment. Washington, DC.

Han, B., Ding, X., Bai, Z., Kong, S. and Guo, G., 2011. Source analysis of particulate matter associated polycyclic aromatic hydrocarbons (PAHs) in an industrial city in northeastern China. J. Environ. Monitoring, 13(9), 2597-2604.

Hazarika, N., Das, A., Kamal, V., Anwar, K., Srivastava, A. and Jain, V.K., 2019. Particle phase PAHs in the atmosphere of Delhi-NCR: With spatial distribution, source characterization and risk approximation. Atmosph. Environ., 200, 329-342.

Hossain, M.A. and Salehuddin, S.M., 2012. Polycyclic aromatic hydrocarbons (PAHs) in edible oils by gas chromatography coupled with mass spectroscopy. Arabian J. Chem., 5(3), 391-396.

Jia, C. and Batterman, S., 2010. A critical review of naphthalene sources and exposures relevant to indoor and outdoor air. Int. J Environ. Res. and public health, 7(7), 2903-2939.

Kim, K.H., Jahan, S.A., Kabir, E. and Brown, R.J., 2013. A review of airborne polycyclic aromatic hydrocarbons (PAHs) and their human health effects. Environ. Int., 60, 71-80.

Kong, S., Li, X., Li, L., Yin, Y., Chen, K., Yuan, L., Zhang, Y., Shan, Y. and Ji, Y., 2015. Variation of polycyclic aromatic hydrocarbons in atmospheric PM2.5 during winter haze period

around 2014 Chinese Spring Festival at Nanjing: Insights of source changes, air mass direction and firework particle injection. Science of the Total Environ., 520, 59-72.

Kulshrestha, U.C., Rao, T.N., Azhaguvel, S. and Kulshrestha, M.J., 2004. Emissions and accumulation of metals in the atmosphere due to crackers and sparkles during Diwali festival in India. Atmosph. Environ., 38(27), 4421-4425.

Kulshrestha, M.J., Singh, R. and Ojha, V.N., 2019. Trends and source attribution of PAHs in fine particulate matter at an urban and a rural site in Indo-Gangetic plain. Urban Climate, 29, 100485.

Kumar, K., Singh, S., Chandra, S. and Kulshrestha, M.J., 2020. Episodic measurements of PM2.5 during crop residue burning and Diwali Periods at Delhi. J. Ind. Geophys. Union, 24(4), 40-50.

Kumar, K., Kulshrestha, M.J., and Singh, S., 2023. Influence and distribution pattern of n-Alkanes in PM2.5 and PM10 during odd- even scheme in Delhi, India. J. Ind. Geophys. Union, 27(3), 174-184.

Kurwadkar, S., Sankar, T.K., Kumar, A., Ambade, B., Gautam, S., Gautam, A.S., Biswas, J.K. and Salam, M.A., 2023. Emissions of black carbon and polycyclic aromatic hydrocarbons: Potential implications of cultural practices during the Covid-19 pandemic. Gond. Res., 114, 4-14.

Mahilang, M., Deb, M.K., Nirmalkar, J. and Pervez, S., 2020. Influence of fireworks emission on aerosol aging process at lower troposphere and associated health risks in an urban region of eastern central India. Atmosph. Pollution Res., 11(7), 1127-1141.

Nezhad, M.E., Goudarzi, G., Babaei, A.A. and Mohammadi, M.J., 2023. Characterization, ratio analysis, and carcinogenic risk assessment of polycyclic aromatic hydrocarbon compounds bounded PM10 in a southwest of Iran. Clinical Epidemiology and Global Health, 24, 101419.

Nisbet, I.C. and Lagoy, P.K., 1992. Toxic equivalency factors (TEFs) for polycyclic aromatic hydrocarbons (PAHs). Regulatory toxicology and pharmacology, 16(3), 290-300.

Orecchio, S., 2011. Polycyclic aromatic hydrocarbons (PAHs) in indoor emission from decorative candles. Atmosph. Environ., 45(10), 1888-1895.

Perrino, C., Tiwari, S., Catrambone, M., Dalla Torre, S., Rantica, E. and Canepari, S., 2011. Chemical characterization of atmospheric PM in Delhi, India, during different periods of the year including Diwali festival. Atmos. Pollut. Res., 2(4), 418-427.

Rani, N. and Kulshrestha, M.J., 2025. Seasonal distribution and deposition patterns of size-segregated particulate matter in human respiratory system in Central Delhi, India. Air Quality, Atmosphere & Health, 18(1), 179-203.

Rani, N., Singh, S. and Kulshrestha, M.J., 2023. Measurement and Distribution Pattern of n-alkanes in Size-Segregated Aerosols During Diwali Festival in Delhi, India. Water, Air, & Soil Pollution, 234(4), 212.

Rastogi, N., Singh, A. and Satish, R., 2019. Characteristics of submicron particles coming from a big firecracker burning event: implications to atmospheric pollution. Atmosph. Pollution Res., 10(2), 629-634.

Ravindra, K., Sokhi, R. and Van Grieken, R., 2008. Atmospheric polycyclic aromatic hydrocarbons: source attribution, emission factors and regulation. Atmosph. Environ., 42(13), 2895-2921.

Ray, D., Chatterjee, A., Majumdar, D., Ghosh, S.K. and Raha, S., 2017. Polycyclic aromatic hydrocarbons over a tropical urban and a high-altitude Himalayan Station in India: Temporal variation and source apportionment. Atmosph. Res., 197, 331-341.

Ren, Y., Wang, G., Wu, C., Wang, J., Li, J., Zhang, L., Han, Y., Liu, L., Cao, C., Cao, J. and He, Q., 2017. Changes in concentration, composition and source contribution of atmospheric organic aerosols by shifting coal to natural gas in Urumqi. Atmosph. Environ., 148, 306-315.

Sarkar, S., Khillare, P.S., Jyethi, D.S., Hasan, A. and Parween, M., 2010. Chemical speciation of respirable suspended particulate matter during a major firework festival in India. J. Hazardous Materials, 184(1-3), 321-330.

Shen, G., Tao, S., Wei, S., Zhang, Y., Wang, R., Wang, B., Li, W., Shen, H., Huang, Y., Chen, Y. and Chen, H., 2012. Emissions of parent, nitro, and oxygenated polycyclic aromatic hydrocarbons from residential wood combustion in rural China. Environ. Sci, Technology, 46(15), 8123-8130.

Shi, G.L., Liu, G.R., Tian, Y.Z., Zhou, X.Y., Peng, X. and Feng, Y.C., 2014. Chemical characteristic and toxicity assessment of particle associated PAHs for the short-term anthropogenic activity event: During the Chinese New Year's Festival in 2013. Science of the Total Environ., 482, 8-14.

Sicre, M.A., Marty, J.C. and Saliot, A., 1990. n-Alkanes, fatty acid esters, and fatty acid salts in size fractionated aerosols collected over the Mediterranean Sea. J. Geophys. Res. Atmospheres, 95(D4), 3649-3657.

Singh, S. and Kulshrestha, M.J., 2024. Investigating sources and health risk assessment of n-alkanes in atmospheric wet deposition in Indo-Gangetic Plain. Atmosph. Environ., 324, 120412.

Singh, R., Chandra, S., Kulshrestha, M.J. and Rashmi, 2016. Chemical constituents in PM10 aerosols during Diwali and Holi Fesitivals in Delhi. J. Ind. Geophys. Union, 20(4), 440-444.

Tobiszewski, M. and Namieśnik, J., 2012. PAH diagnostic ratios for the identification of pollution emission sources. Environ. Pollution, 162, 110-119.

USEPA, 1991. Role of the baseline risk assessment in Superfund remedy selection decisions, Office of Solid Waste and Emergency Response, Washington, USA, 1991.

Website. https://monographs.iarc.who.int/list-of-classifications

WHO, U., 2000. Air quality guidelines for Europe, Second Edition. WHO Reg. Publ. Eur. Ser. 91.

World air quality report, 2024. IQAir. https://www.greenpeace.org/static/planet4-chile-stateless/2025/03/edf90b7a-2024_world_air_quality_report_vf.pdf

Zhang, J., Yang, L., Ledoux, F., Courcot, D., Mellouki, A., Gao, Y., Jiang, P., Li, Y. and Wang, W., 2019. PM2.5-bound polycyclic aromatic hydrocarbons (PAHs) and nitrated PAHs (NPAHs) in rural and suburban areas in Shandong and Henan Provinces during the 2016 Chinese New Year's holiday. Environ. Pollution, 250, 782-791.

Received on: 29-01-2026 ; Revised on: 05-02-2026 ; Accepted on: 06-02-2026

J. Ind. Geophys. Union, 30(2) (2026), 122-135
https://doi.org/10.71122/JIGU.30(2)2026.0013

A comparative study of stochastic nature of anthropogenic aerosol using SARIMA and LSTM methods

J. Arul Asir[1*], H. Johnson Jeyakumar[1] and C. P. Anil Kumar[2]
[1]P.G and Research Department of Physics, Pope's College, Manonmaniam Sundaranar University, Abishekapatti, Tirunelveli – 627012, Tamil Nadu, India.
[2]Equatorial Geophysical Research Laboratory, Indian Institute of Geomagnetism, Tirunelveli- 627011, Tamil Nadu, India.
[*]Corresponding author: arulasirphy@popescollege.edu.in

ABSTRACT

The troposphere is a dynamic region characterized by intricate interactions among natural and anthropogenic processes. Among these, aerosol loading, particularly fine particulate matter ($PM_{2.5}$), poses significant challenges in understanding the greenhouse effect and complicates air quality assessment due to its spatiotemporal variability. This study presents a comparative stochastic modelling framework for forecasting anthropogenic aerosol concentrations using both parametric and non-parametric approaches over Alandur (13.0° N, 80.10° E), Tamil Nadu, India. Specifically, a Seasonal Autoregressive Integrated Moving Average (SARIMA) model and a Long Short-Term Memory (LSTM) neural network, were employed to forecast $PM_{2.5}$ levels using observational data from 2023 and 2024. SARIMA, a classical statistical model, effectively captured regular patterns and seasonal trends. In contrast, the LSTM model, a deep learning approach, demonstrated enhanced performance in modelling non-linear dependencies and temporal dynamics. Model evaluations based on Root Mean Square Error (RMSE), indicated that LSTM consistently outperformed SARIMA, underlining its effectiveness in capturing the stochastic and complex behaviour of aerosol concentrations. These findings underscore the potential of integrating advanced machine learning techniques with traditional time series models to enhance the accuracy of air quality forecasting and environmental risk mitigation strategies.

Keywords: Aerosol, $PM_{2.5}$ levels, Alandur (Tamil Nadu), Health impact, Seasonal ARIMA, Machine learning, Neural network.

INTRODUCTION

Particulate matter (PM) in the atmosphere, originating from both natural and anthropogenic sources, consists of fine solid or liquid particles suspended in air. These aerosols are either directly emitted or formed via secondary chemical reactions of precursor gases. As a result, PM is a heterogeneous mixture with varied chemical compositions and size distributions, often exhibiting a core-shell morphology where secondary constituents condense around a primary core. Based on aerodynamic diameter, PM is commonly classified into fine particles ($PM_{2.5}$; ≤2.5 μm), ultrafine particles ($PM_{0.1}$; ≤0.1 μm), and nanoparticles ($PM_{0.05}$; ≤0.05 μm or ≤50 nm). This spatial-temporal distribution of PM concentration and composition is driven by complex interactions between emission sources, atmospheric transport mechanisms, in-situ chemical transformations, and removal processes such as dry and wet deposition. In addition to primary and secondary sources, background particulate matter representing PM levels in the absence of local anthropological influence, also contributes to the overall spatiotemporal variability (Yang et al., 2011: Celo and Dabek-Zlotorzynska, 2011; Seinfeld and Pandis, 2016; Guevara, 2016; Donahue et al., 2016). Alongside emission sources and transformation mechanisms, atmospheric conditions play a crucial role in modulating PM behaviour. Meteorological parameters such as wind speed, temperature, and relative humidity, significantly influence the dispersion, accumulation, and chemical transformation of aerosols (Zhang et al., 2018). Recent studies (Bhattarai et al., 2024; Pan et al., 2024; Yim et al., 2024), highlight the growing concern over fine particulate matter ($PM_{2.5}$) due to its combined impact on air quality degradation and climate alteration. With an atmospheric lifetime ranging from days to weeks, $PM_{2.5}$ is capable of long-range transport, leading to trans-boundary pollution and contributing to both regional and global environmental challenges. Meteorological influences and public health consequences are linked to PM exposure.

Andreae (2009) established a global correlation between CCN (Cloud Condensation Nuclei) concentrations and Aerosol Optical Thickness (AOT), showing that polluted marine and continental regions have nearly ten times higher CCN concentrations and about five times greater AOT than remote areas. This highlights the crucial role of aerosol optical properties in influencing cloud microphysics. Complementing these findings, Zhang et al. (2012) investigated CCN activation dynamics in Tianjin, China, using a thermal-gradient diffusion chamber (Droplet Measurement Technologies - CCNC). alongside aerosol size and composition analysis. Their findings confirmed that larger or more hygroscopic particles activate at lower supersaturation, while smaller or less hygroscopic particles, require higher supersaturation. Additionally, meteorological factors significantly influence $PM_{2.5}$ concentrations. Zhao et al. (2017), using the WRF-Chem model, found that increased anthropogenic aerosol loading in China, significantly enhanced cloud droplet formation and the liquefaction process in cumulus clouds. Following these results, Cheung et al. (2019) studied $PM_{2.5}$ over northern Taiwan from April 2017 to March 2018. In this study, continental air masses exhibited higher hygroscopicity (K-values), whereas local air masses showed higher Condensation Nuclei and CCN concentrations but lower K-values. These differences were reflected in the $PM_{2.5}$ chemical composition. The study also found that new particle formation enhanced

CCN levels through coagulation with smaller particles. Gao et al. (2023) further expanded on this by quantifying Aerosol Radiation Interactions (ARIs) and Aerosol Cloud Interactions (ACIs) over an eight-year period (2013–2021). Their results showed that ARI's contributed more substantially to $PM_{2.5}$ enhancement (5.59 $\mu g\, m^{-3}$) than ACI's (3.96 $\mu g\, m^{-3}$) during peak pollution episodes in eastern China. While aerosol composition determines particle activation and growth, meteorological parameters such as temperature and humidity, govern their dispersion and transformation.

Besides, Megaritis et al. (2014), employing a three-dimensional chemical transport model, quantified the seasonal sensitivity of $PM_{2.5}$ across Europe to variations in meteorological parameters, identifying temperature as the predominant influence year-round. Similarly, Tai et al. (2012) observed strong positive correlations between $PM_{2.5}$ and temperature across most of the United States, except for nitrate components in the southeast, which exhibited an inverse relationship. Principal component analysis further revealed that key meteorological modes explained 20–40% of the daily variability in $PM_{2.5}$ concentrations. Similarly, long term environmental changes, such as climate variability and land cover alterations, also influence $PM_{2.5}$ levels. Fu et al. (2016) used global chemical transport models to quantify these impacts over East Asia, finding that climate change can cause significant seasonal shifts in $PM_{2.5}$ concentrations, with reductions in winter and increases in summer. Although land cover and land use changes contributed to regional variability, anthropogenic emissions remained the primary driver of air quality deterioration. Farahat and Abuelgasim (2022) analyzed PM_{10} and $PM_{2.5}$ variations during cloud seeding missions in the United Arab Emirates. Their findings indicated that $PM_{2.5}$ levels were most elevated in industrial areas and were significantly influenced by cloud seeding, whereas urban PM_{10} concentrations remained higher but less sensitive to such interventions. In a similar manner**,** Singh et al. (2021) analyzed $PM_{2.5}$ trends across five Indian megacities Delhi, Kolkata, Mumbai, Hyderabad, and Chennai alongside the U.S. data over a six-year period (2014–2019). Delhi emerged as the most polluted city, followed by Kolkata and Mumbai. Expanding on the urban pollution patterns, Gu et al. (2024) also evaluated the health impacts of $PM_{2.5}$ across Southeast Asia using air quality modeling. They estimated approximately 900,000 premature deaths annually, with 87% linked to $PM_{2.5}$ exposure. Of these, 77% were due to local emissions primarily from industrial (45%) and residential (17%) sectors, while 23% were attributed to transboundary pollution. Time series forecasting can play a vital role in environmental monitoring by enabling predictive insights into complex and temporally structured phenomena.

Owing to the inherent stochasticity of atmospheric processes, model selection must align with the data's structural characteristics and forecasting objectives (Chatfield, 1975; Gautam and Singh, 2020). Previously, the power spectral analysis using a Blackman Tukey window. revealed dominant biennial and seasonal periodicities in $PM_{2.5}$ concentrations over Alandur's industrial corridor during pre- and post- pandemic periods. Further, wavelet-based phase coherence, confirmed the persistence of these periodic components, highlighting strong meteorological influences (Asir et al., 2024). In this study, we compare two forecasting frameworks Seasonal Autoregressive Integrated Moving Average (SARIMA) and Long Short-Term Memory (LSTM) networks, representing parametric and non-parametric approaches, respectively. SARIMA, grounded in linear stochtic modeling, is well-suited for seasonal stationarity, while LSTM networks, with their memory-cell architecture, effectively capture nonlinear and dependencies.

OBSERVATIONAL SITE AND AQUIRED DATA

The observational site selected for this study is Alandur (13.0° N, 80.10° E), located in the southern part of Chennai, Tamil Nadu (India). Known for its dense population, heavy vehicular traffic, and industrial zones, Alandur presents a complex urban environment encompassing residential, commercial, and transportation sectors. This diverse setting makes it a suitable candidate for evaluating aerosol loading and forecasting in mixed-use urban areas. $PM_{2.5}$ concentration data were sourced from the Central Pollution Control Board's (CPCB) Continuous Ambient Air Quality Monitoring Stations (CAAQMS) via the portal (https://airquality.cpcb.gov.in), covering the years 2023 and 2024, with 730 daily records in total. Due to routine maintenance, the 2023 dataset had 45 missing values, addressed using a 21-day rolling mean imputation. For the 12 missing values in 2024, a 7-day moving average was applied. Each year was treated as a separate timeline, while this approach helped preserve temporal continuity, it has smoothed out certain seasonal components in 2023; this limitation was considered during SARIMA model fitting. Outliers were detected using the Inter quartile Range (IQR) method, identifying values outside the Q_1–Q_3 range. The outlier rates were 1.37% for 2023 and 2.46% for 2024. Instead of removal, these values were normalized using the Z-score method to retain extreme event information while minimizing their impact on model training**.** A sensitivity analysis was also performed to ensure that the results were not biased by the chosen window sizes and their results are given in Table 1.

Table 1. Sensitivity analysis: Actual vs imputed $PM_{2.5}$ data (2023 and 2024)

Year	Imputation method	Statistic	Actual ($PM_{2.5}$)	Imputed ($PM_{2.5}$)	% Change (actual vs imputed)
2023	21-Day window	Mean	45.244	44.947	−0.65
		Median	40.660	40.070	−1.45
		Mode	28.145	26.161	−7.05
		Std dev	24.016	24.027	0.05
		Julian days	365	365	0.83
2024	7-Day window	Mean	45.114	45.096	−0.04
		Median	29.010	29.010	0.00
		Mode	13.620	13.620	0.00
		Std dev	35.396	35.355	−0.12
		Julian Days	366	366	0.00

METHODS

In time series analysis, data collected over time have temporal dependencies and non-stationarity commonly observed in real world (Shumway and Stoffer, 2011). The Autocorrelation Function (ACF) quantifies correlations between observations at different lags, aiding pattern detection and model development. Robust time series models integrate deterministic trends with stochastic components to capture both systematic and random variations (Kirchgässner and Wolters, 2007). These methods are essential in environmental and physical sciences, where complex temporal dynamics are common**.** A crucial prerequisite in this analysis is determining the stationarity of the time series, as it ensures consistent statistical properties over time and underpins the development of accurate models and reliable forecasts. In many practical systems, stationarity is maintained through regular control actions or continuous component maintenance, which stabilize underlying processes and prevent structural changes**.** A time series is called stationary, if the joint probability distribution of any n observations, $\{z_{t+1}, z_{t+2}, \ldots, z_{t+n}\}$ (i.e., realizations of the time series at times t + 1, t + 2, . . . , t + n) of this series remain the same as another set of n observations shifted by k time units, that is, $\{z_{t+1+k}, z_{t+2+k}, \ldots, z_{t+n+k}\}$ for practical purposes (Bisgaard and kulahci, 2011).

Extending the concept of stationarity, the autocorrelation function (ACF) and the Partial Autocorrelation Function (PACF), provide critical insights into the underlying structure of a time series. When a series exhibits a trend, the ACF typically shows large positive autocorrelations at small lags, reflecting the similarity of adjacent observations and resulting in a slow decay over increasing lags. Seasonality introduces distinct periodic peaks in the ACF at multiples of the seasonal frequency, signalling regular cyclical patterns. The coexistence of trend and seasonality, produces an ACF characterized by both gradual decline and periodic spikes. Conversely, a lack of significant autocorrelation across all lags indicates a purely random process, commonly termed white noise (Hyndman and Athanasopoulos, 2014), as provided in Eq.1.

Autocorrelation function is expressed as $r_k = \frac{\sum_{t=k+1}^{T}(y_t-\bar{y})(y_{t-k}-\bar{y})}{\sum_{t=1}^{T}(y_t-\bar{y})^2}$ (1)

where, r_k is the autocorrelation at lag k, y_t is the value of the time series at time (t), y_{t-k} Lagged value of the time series k steps before time (t), $\bar{y}$ is the mean of the time series value

Like the ACF, PACF depends solely on the second order properties of the process. The partial autocorrelation at lag k, denoted as α_K, represents the correlation between X_1 and X_{k+1}, adjusted for the influence of intervening observations $X_2,\ldots,X_K$ (Brockwell and Davis, 2016). PACF quantifies the direct relationship between observations at different lags, by removing the effects of intermediate lags. This makes the PACF a valuable tool for identifying which lagged terms have a meaningful and independent impact on the current observation. Negative partial correlation is often referred to as the reflection coefficient which lie within the range of –1 and 1 (Broerson, 2006; Hyndman and Athanasopoulos, 2014) as in Eq. 2.

The partial autocorrelation function is expressed as $\phi_{n,n} = \frac{\rho_n - \sum_{k=1}^{n-1}\phi_{n-1,k}\rho(n-k)}{1-\sum_{k=1}^{n-1}\phi_{n-1,k}\rho(k)}$ (2)

where, $\phi_{n,n}$ is the partial autocorrelation at lag n, ρ_n is the autocorrelation at lag n, ϕ_{n-1} Partial autocorrelation at lag k from the previous step (lag n−1), $k\rho(n-k)$ autocorrelation at lag n−k

However, visual inspection of the ACF and PACF alone is insufficient to conclusively determine stationarity. Unit root tests are applied to statistically assess the need for differencing. Among these, the Augmented Dickey-Fuller (ADF) test is widely used, extending the Dickey-Fuller test by including lagged differences to account for autocorrelation. The ADF models the first-order difference of the series as a regression on lagged values and lagged differences up to m lags, providing a formal test for non-stationarity (Cromwell et al., 1994; Pal and Prakash, 2017). The ADF Test is given by Eq. 3

$$\Delta x(t) = \alpha_1 x(t-1) + \Sigma_J \beta_j \Delta x(t-j) + e(t) \quad (3)$$

where, $\Delta x(t)$ represents the change in the variable x at time t. $\alpha_1 x(t-1)$ represents the current change in $x(t)$ which is influenced by its previous value $x(t-1)$, with $\alpha_1$as the coefficient, $\beta_j \Delta x(t-j)$ represents the influence of past changes in x(t) on the current change, β_j are the coefficients for each lag j, and $e(t)$ is the error term or noise

Parametric and non-parametric methods

Due to limited observational data, multiple stochastic processes can explain the same time series. Model selection begins by defining candidates and applying estimation or inference. Parametric models, like ARIMA and SARIMA, have fixed parameters, while nonparametric models, such as LSTM networks or power spectral analysis, involve flexible or infinite parameters (Fan and Yao, 2005). Although the distinction can be blur, it guides estimation methods. Empirical evidence is mixed: parametric models offer efficiency and interpretability, while nonparametric methods provide flexibility for complex patterns (Gautam and Singh, 2020). Model choice should align with data characteristics and forecasting goals.

ARIMA and SARIMA

The Autoregressive (AR) model was introduced by Yule (1927) and expanded by Walker (1931), while Slutzky (1937) developed the Moving Average (MA) model. Wold (1938) laid the theoretical groundwork for the combined ARMA framework. Box and Jenkins (1976) integrated these components into the Autoregressive Integrated Moving Average (ARIMA) model, designed for effective modeling and forecasting of both stationary and non-stationary time series. The ARIMA model comprises three parts: autoregressive (ar), which relates observations to their past values; integrated (I), which applies differencing to achieve stationarity; and moving average (ma), which models dependence on past forecast errors.

For seasonal data, SARIMA extends ARIMA by incorporating seasonal differencing and seasonal AR and MA terms. These models are widely applied in environmental and risk analysis for capturing complex temporal dynamics (Yule, 1927; Walker, 1931; Slutzky, 1937; Wold, 1938; Box and Jenkins, 1976; Kumar and Jain, 2010; Hyndman and Athanasopoulos, 2014; Pal and Prakash, 2017; Naveen and Anu, 2017; Kaur et al., 2023). ARIMA (p, d, q) model is expressed as Eq. 4.

$$Y_t = C + \sum_{i=1}^{p} \phi_t y_{t-i} + \sum_{J=1}^{q} \theta_j \varepsilon_{t-j} + \varepsilon_t \quad (4)$$

where, c - is the constant term, ϕ_t - is the coefficient of AR, θ_j - is the coefficient of MA

The SARIMA model is typically denoted as SARIMA (p, d, q) (P, D, Q) $_s$, where S is the length of the seasonal cycle (for example, 12 for monthly data with yearly seasonality). The general form of the SARIMA (p, d, q) (P, D, Q)$_s$ is expressed as Eq. 5:

$$Y_t = C + \sum_{i=1}^{p} \phi_t y_{t-i} + \sum_{I=1}^{P} \boldsymbol{\phi_t} Y_{t-IS} + \sum_{J=1}^{q} \theta_j \varepsilon_{t-j} + \sum_{J=1}^{Q} \boldsymbol{\theta_J} \varepsilon_{t-JS} + \varepsilon_t \quad (5)$$

where, c - is the constant term, ϕ_t - is the coefficient of AR, θ_j - is the coefficient of ma, $\boldsymbol{\phi_t}$ - is the coefficient of seasonal AR, $\boldsymbol{\theta_j}$ - is the coefficient of ma. The differencing equation is represented as Integration I_D (Differencing equation) $y'_t = Y_t - Y_{t-s}$

In SARIMA modeling, the seasonal order P, D, Q, and s reflect recurring patterns in time series data. However, this seasonal structure can vary from year to year due to external factors such as climate variations or changes in emission sources. These factors can alter the strength, timing, or frequency of seasonal peaks and valleys. SARIMA addresses this by iteratively adjusting seasonal parameters during model fitting, enabling it to capture both stable seasonal patterns and annual fluctuations. Hence, the seasonal order varies from year to year, and SARIMA models capture this by adjusting the seasonal parameters, ensuring the model adapts to evolving patterns while maintaining predictive accuracy.

Long Short – Term Memory (LSTM) Neural Network Analysis

The increasing availability of computational power and large-scale data has greatly advanced the effectiveness of modeling techniques in uncovering complex and hidden patterns in time series data. Among these, neural networks have emerged as powerful tools due to their ability to learn intrinsic relationships directly from raw inputs. Recurrent Neural Networks (RNNs) are particularly well-suited for modeling sequential data, as they use the current input and previous hidden state to capture temporal dependencies. However, traditional RNNs often suffer from vanishing or exploding gradient problems, which limit their ability to learn long-term dependencies. To address this, Long Short-Term Memory (LSTM) networks a specialized form of RNNs were developed (Figure 1). LSTMs introduce a cell state that carries information across time steps and use a gating mechanism to regulate the flow of information. Each LSTM cell contains three gates: the forget gate, which removes irrelevant past information; the input gate, which decides what new information to store; and the output gate, which determines the information to pass forward. These gates, governed by sigmoid activation functions and element-wise operations, allow

LSTMs to selectively retain relevant information and discard noise. This architecture enables LSTMs to model long-term, non-linear dependencies more effectively than standard RNNs, reducing overfitting and computational complexity. Due to these advantages, LSTMs are widely applied in fields such as weather forecasting, anomaly detection, and environmental time series modeling, where long-term memory and adaptability are crucial (Rebala et al., 2019; Yu et al., 2021; Luo and Gong, 2023).

Model evaluation metrics MSE and RMSE

MSE involves squaring the errors, its value is always non-negative, ranging from zero to infinity. Furthermore, MSE increases exponentially as the magnitude of errors increases. Therefore, a model exhibiting a lower MSE value, ideally approaching zero, is considered to have superior predictive accuracy**.** The RMSE is the square root of the mean squared error (MSE). Taking the root does not affect the relative ranks of models, but it yields a metric with the same units X (Hudson, 2022). The basic equation can be expressed as,

$$\text{MSE} = {}^{1}/_{n} \sum_{I=1}^{n} (y_i - \hat{y}_i)^2 \qquad (6)$$

$$\text{RMSE} = \sqrt{\frac{1}{n}\sum_{I=1}^{n} (y_i - \hat{y}_i)^2} \qquad (7)$$

where, y_i is the actual value, $\hat{y}_i$ is the predicted value, n is the number of observations.

RESULTS AND DISCUSSION

Figure 2(a) and (b) illustrate the time series of daily $PM_{2.5}$ concentrations for 2023 and 2024, with the x-axis representing months and the y-axis indicating concentration intensity. In 2023, the dry winter months (January–February) exhibited a sharp increase in $PM_{2.5}$ levels, peaking in early January. In contrast, 2024 showed milder winter fluctuations, with peaks occurring later in January. Summer and post-monsoon months (March–June), revealed moderate variations, with generally higher concentrations in 2023 compared to 2024. During the southwest monsoon (July–August), 2024 recorded abrupt fluctuations, while 2023 displayed more stable trends. These seasonal variations are consistent with findings by Chen et al. (2020), who reported similar patterns across Delhi, Hyderabad, Chennai, and Mumbai (2015–2018), with peak $PM_{2.5}$ concentrations in winter and minimum levels during the monsoon due to effective wet scavenging. Additionally, intercity differences were attributed to variations in wind patterns and $PM_{2.5}$ transport dynamics.

The SARIMA model was implemented in Python - Jupyter Lab environment to forecast and analyse the stochastic behaviour of $PM_{2.5}$ concentrations. Effective time series forecasting requires modelling future values as functions of past observations, with particular emphasis on capturing trend and seasonality, two fundamental components shaping temporal patterns (Peixeiro, 2022). Accurate identification of these components is essential for informed model selection and reliable forecasting. To analyse the temporal dependence in the $PM_{2.5}$ series, the autocorrelation function (ACF) and partial autocorrelation function (PACF) were applied to identify significant lag structures and guide model selection.

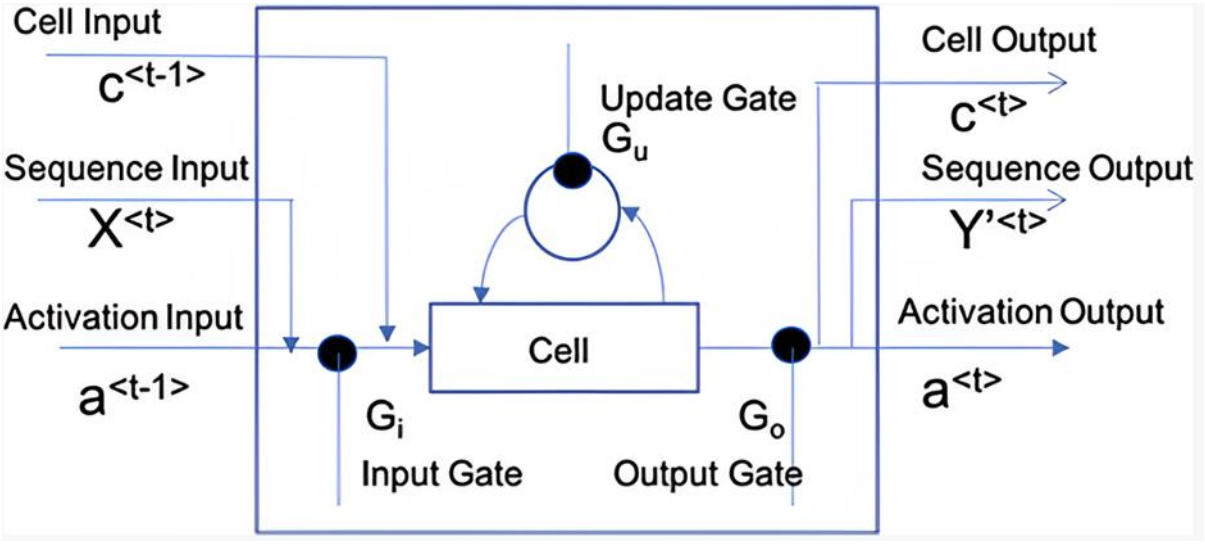

Figure 1. LSTM architecture showing how an LSTM uses its Input Gate (G_i), Update/Forget Gate (G_u), and Output Gate (G_o) to control what information is added, retained, or passed forward at each time step. By combining the current input with the previous cell and hidden states, the LSTM produces an updated cell state and activation output.

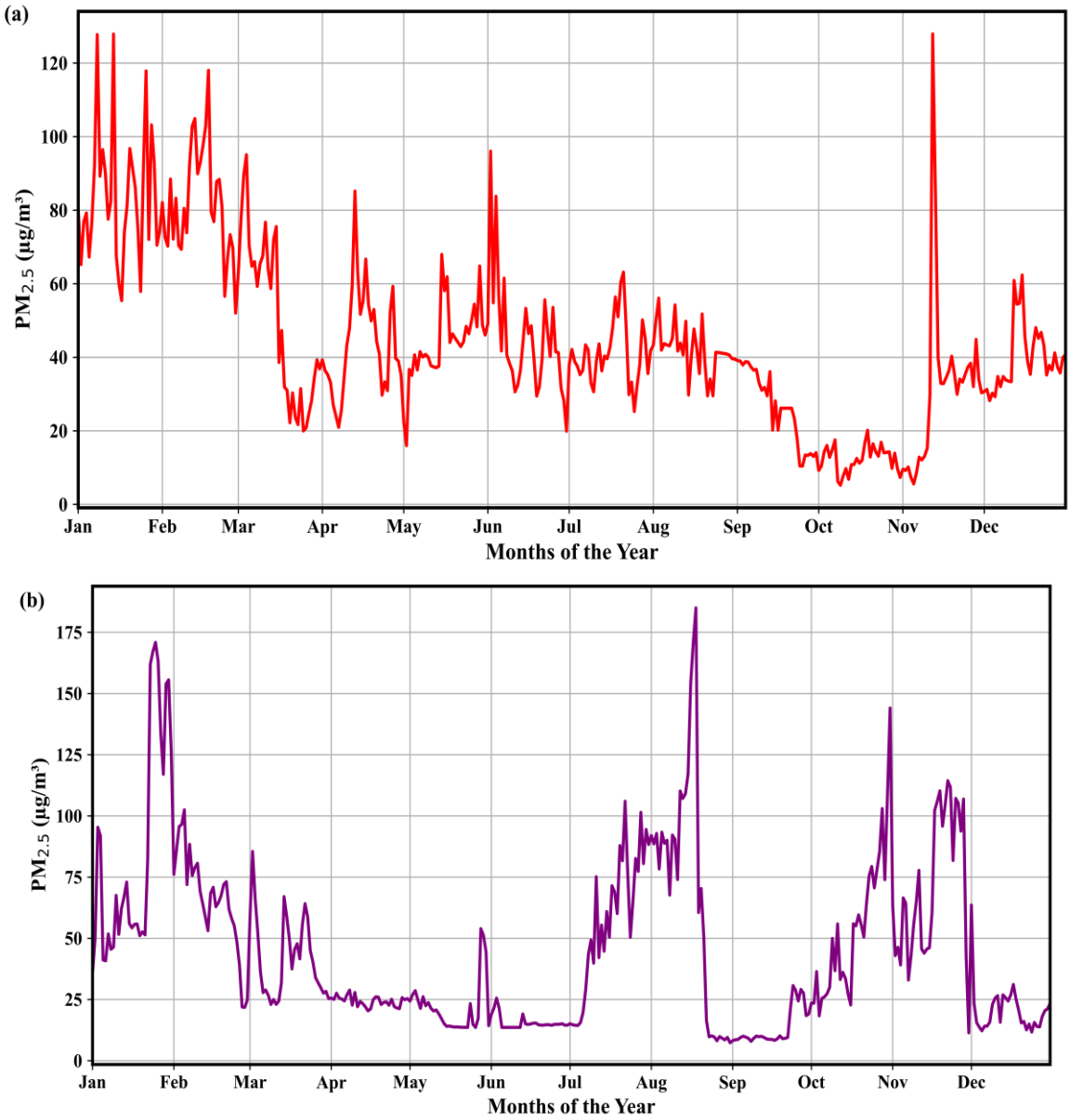

Figure 2. Time series analyses of particulate matter ($PM_{2.5}$) concentrations for the years, **(a)** 2023 and **(b)** 2024

The ACF captures both direct and indirect correlations of a time series with its lagged values, thereby offering insights into persistence and stationarity. A slow decay of the ACF beyond the confidence bounds, as observed for the 2023 dataset (Figure 3a), is indicative of a pronounced trend and potential seasonal effects, consistent with non-stationary dynamics (Kumar and Jain, 2010). In contrast, the PACF designed to isolate the direct effect of each lag by controlling for the intervening lags, revealed significant initial spikes followed by minor fluctuations (Figure 3b), suggesting an autoregressive structure embedded within a non-stationary process (Hyndman and Athanasopoulos, 2014). For 2024, the ACF and the PACF a comparable structure with marginal variations was observed (not presented here due to brevity). To supplement the visual diagnostics, the Augmented Dickey-Fuller (ADF) test was applied to statistically assess the stationarity of both time series. The results returned p-values exceeding the 0.05 threshold, indicating the presence of a unit root in both cases, and thereby confirming non-stationarity at a 95% confidence level. These findings substantiate the necessity for appropriate differencing and seasonal adjustment in model specification to accommodate the intrinsic stochasticity and temporal dependencies characteristic of urban $PM_{2.5}$ concentrations.

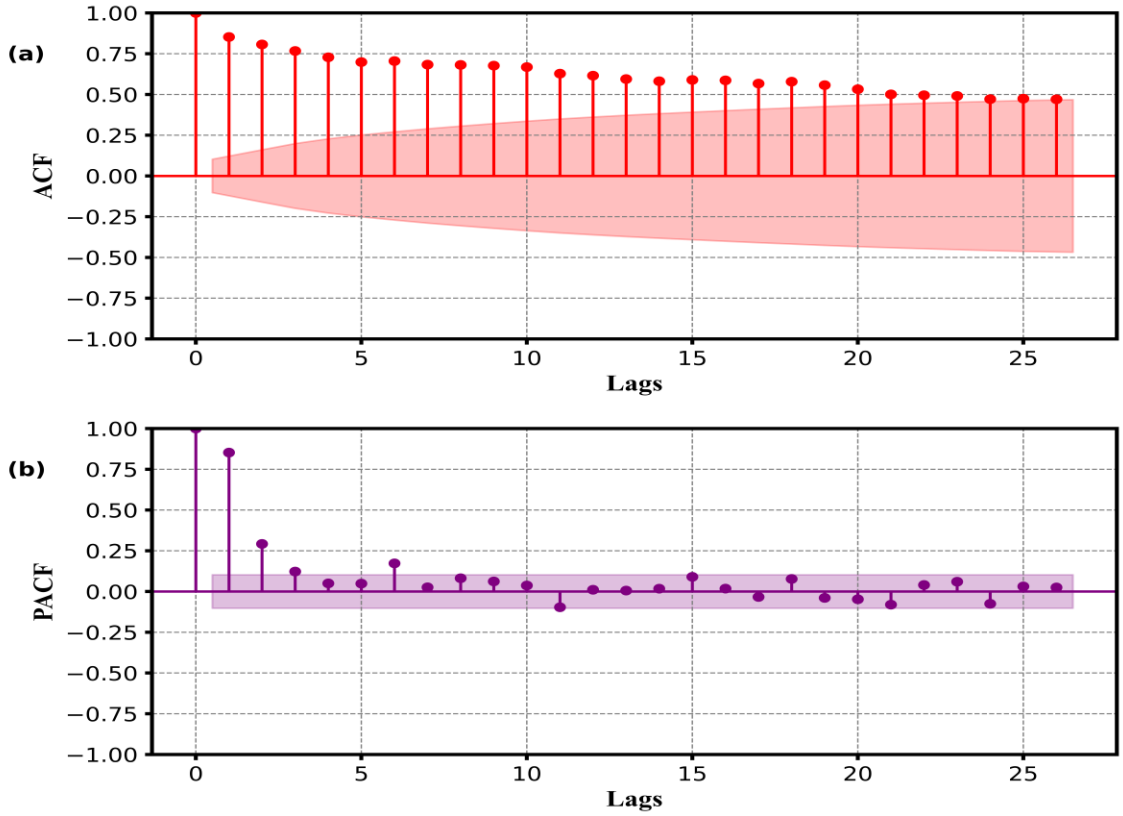

Figure 3. **(a)** ACF and **(b)** PACF plot for the year 2023

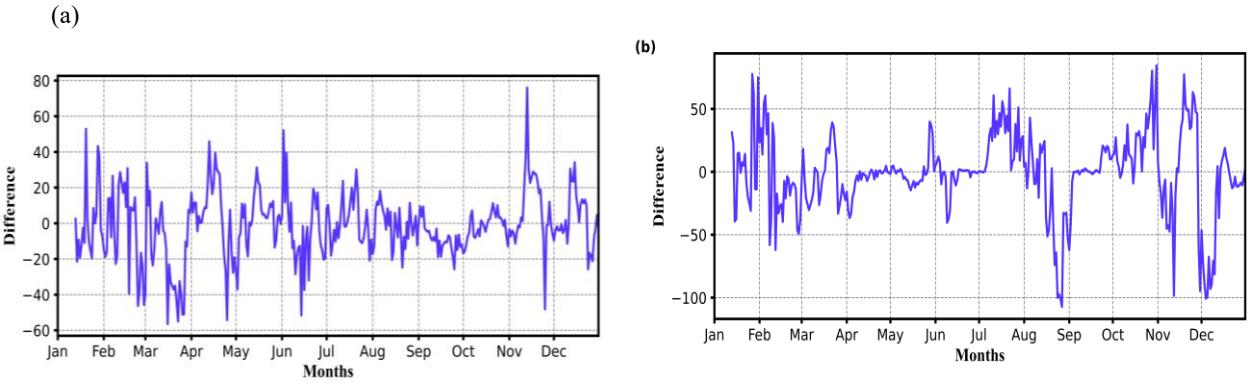

Figure 4. Seasonal first difference of $PM_{2.5}$ plots for the year **(a)** 2023, and **(b)** 2024

Figure 4 (a) and 4 (b**)** illustrate the seasonally differenced $PM_{2.5}$ time series for 2023 and 2024, respectively. A seasonal differencing lag of 12 was applied to capture annual periodicity, resulting in the exclusion of the first 12 observations in each series. Post-differencing, the Augmented Dickey-Fuller (ADF) test yielded statistically significant p-values of 0.0029 (2023) and 0.021 (2024), allowing for rejection of the null hypothesis of a unit root and confirming that both differenced series are stationary.

Following stationarity confirmation, the autocorrelation (ACF) and partial autocorrelation (PACF) plots of the differenced series were examined to identify model parameters, as shown in Figure 5 (a) and 5 (b). For 2023 (Figure 5a), the ACF dropped below the 95% confidence interval by lag 5 and approached zero by lag 10. A slight negative autocorrelation was observed at lag 11. The corresponding PACF (Figure 5b) showed a peak at lag 2 near the confidence limit, decaying to zero by lag 3, with a negative spike at lag 11.

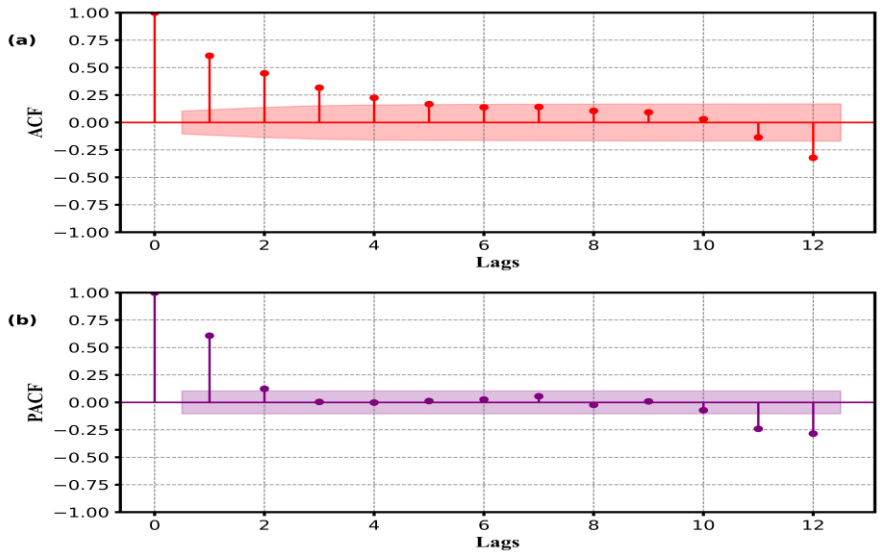

Figure 5. Seasonal differenced plot of **(a)** ACF, and **(b)** PACF for the year 2023

Table 2. AIC, BIC, and HQIC values for various fitted models for the year 2023 and 2024

SARIMA MODEL order 2023	AIC	BIC	HQIC
$(0,0,0)\ (2,1,4)_{11}$	2594.63	2620.768	2605.08
$(1,0,1)\ (2,1,4)_{11}$	2290.35	2323.92	2303.77
$(1,1,1)\ (2,1,4)_{11}$	2280.65	2314.10	2294.06
$(1,1,1)\ (2,1,5)_{11}$	2196.54	2233.44	2211.31
SARIMA MODEL order 2024	AIC	BIC	HQIC
$(0,0,0)\ (3,1,7)_{12}$	2530.98	2570.52	2546.86
$(1,1,1)\ (3,1,6)_{12}$	2294.83	2338.40	2312.31
$(1,0,1)\ (3,1,6)_{12}$	2293.51	2337.12	2311.00

Model order selection for 2023 and 2024

The lag at which autocorrelation (ACF) and partial autocorrelation (PACF) values fall within the 95% confidence interval indicating statistical insignificance, is commonly used to estimate the orders of the moving average MA(q) and autoregressive AR(p) components, respectively. In the presence of pronounced seasonality, the ACF of the seasonally differenced series often shows significant spikes at seasonal lags (e.g., lag 12), implying a stronger seasonal MA component. Conversely, the PACF generally exhibits weaker or fewer seasonal spikes, suggesting a lower seasonal AR order (P), compared to the seasonal MA order (Q). Appropriate model order selection is critical to balance complexity and performance. Underfitting (model under-specification) can miss essential patterns, while overfitting (model over-specification), may capture noise instead of the underlying signal. Thus, ACF and PACF diagnostics serve as key initial tools in guiding SARIMA model specification. To refine model selection, the Akaike Information Criterion (AIC) is employed to evaluate multiple candidate models, with preference given to the model exhibiting the lowest AIC value. This indicates an optimal trade-off between goodness-of-fit and model parsimony. Table 2 presents the Akaike Information Criterion, Bayesian Information Criterion, and HQIC values for several models, from which the optimal configuration was chosen based on minimum information criteria values. The SARIMA $(1, 1, 1)\ (2, 1, 5)_{11}$ configuration yielded the lowest Akaike Information Criterion (AIC), indicating a better balance between model fit and complexity for 2023. Further the seasonal period of 11 is chosen as the data had a large number of missing values filled by statistical methods on different months. This reflected in a trade off in performance of the model when it was modelled for a period of 12 months. Hence, a seasonal period of 11 months was chosen for and optimal Fit. For the year 2024, the SARIMA $(1, 0, 1)\ (3, 1, 6)_{12}$. configuration yielded the lowest Akaike Information Criterion (AIC), indicating a better balance between model fit and complexity. Table 2 gives their model summaries. Minor variations are seen among the all the models.

Tables 3 and **4** present the estimated coefficients for the optimal SARIMA model of order $(1,1,1)\ (2,1,5)_{11}$, $(1,0,1)\ (3,1,6)_{12}$ applied to the $PM_{2.5}$ time series for the years 2023 and 2024, respectively. The Coefficient column reports the estimated parameter values for both seasonal and non-seasonal

components. The standard error reflects the uncertainty associated with each estimate. The z-statistic represents the ratio of the coefficient to its standard error, providing a measure of statistical significance, while P>|z| indicates the two-tailed p-value for the null hypothesis that the coefficient equals zero. For both years, the non-seasonal parameters were statistically significant ($p < 0.05$), suggesting a strong contribution to model performance. However, the seasonal components, while retained for structural completeness, showed comparatively weaker significance especially in 2024 implying less pronounced seasonal effects in that year. This observation supports the visual trends observed in the time series plots. The Ljung–Box Q statistic ($L_1 = 0.67$ and $L_I = 0.57$ for both models), indicates that the residuals approximate white noise, confirming that the temporal structure of the series was adequately captured and validating the assumption of residual independence critical for forecast reliability.

Table 3. Summary of the SARIMA model order $(1,1,1)\ (2,1,5)_{11}$

Model order for 2023		$(1,1,1)\ (2,1,5)_{11}$		
L Jung box (Q)		0.67		
Order	Co-efficient value	Standard error	Z- statistics	$\rho > \|z\|$
AR (1)	0.5160	0.096	5.355	0
MA (1)	-0.8272	0.073	-11.361	0
AR. S (1)	-1.0798	0.90	-11.968	0
AR. S (2)	-0.5290	0.075	-7.071	0
MA. S (1)	0.2163	0.120	1.800	0.072
MA. S (2)	-0.5602	0.088	-6.343	0
MA. S (3)	-0.4551	0.106	-4.2187	0
MA. S (4)	0.1424	0.079	1.801	0.072
MA. S (5)	0.0200	0.083	0.242	0

Table 4. Summary of the SARIMA model order $(1,0,1)\ (3,1,6)_{12}$

Model order for 2024		$(1,0,1)\ (3,1,6)_{12}$		
Ljung box (Q)		0.57		
Order	Co-efficient value	Standard error	Z- Statistics	$\rho > \|z\|$
AR (1)	0.9255	0.020	47.33	0
MA (1)	-0.1938	0.040	-4.808	0
AR. S (1)	0.2591	0.436	0.594	0.533
AR. S (2)	-0.3742	0.457	-0.818	0.413
AR. S (3)	0.0013	0.211	0.006	0.995
MA. S (1)	-1.2103	0.445	-2.720	0.007
MA. S (2)	0.5239	0.808	0.648	0.517
MA. S (3)	-0.3209	0.548	-0.586	0.558
MA. S (4)	0.0744	0.211	0.352	0.725
MA. S (5)	-0.0218	0.170	-0.128	0.898
MA. S (6)	0.0390	0.129	0.302	0.736

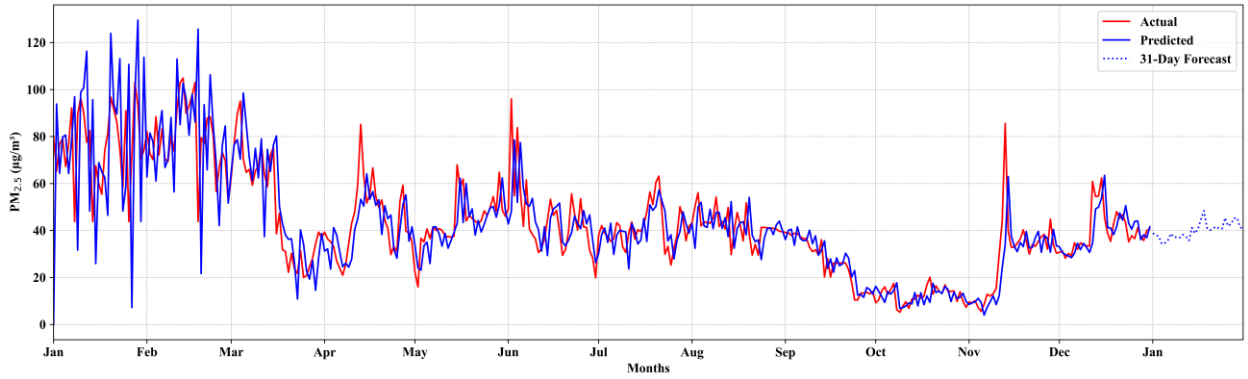

Figure 6. Forecast generated using the SARIMA model of the order $(1,1,1)\ (2,1,5)_{11}$ for the year 2023. The red line represents the actual values. The blue line represents the modelled forecast value. The blue dotted line represents the 31 days out of sample forecast.

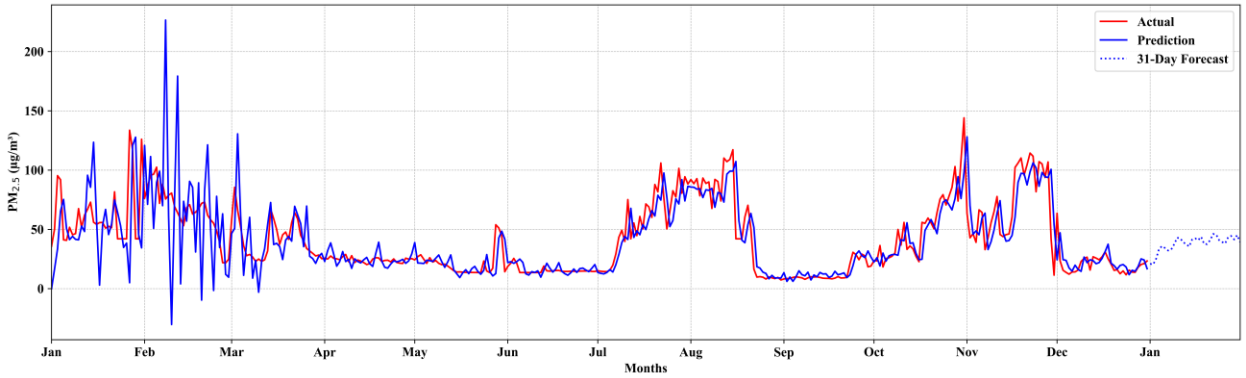

Figure 7. Forecast generated using the SARIMA model of the order (1,0,1) $(3,1,6)_{12}$ for the year 2024. The red line represents the actual values. The blue line represents the modelled forecast value. The blue dotted line represents the 31 days out of sample forecast.

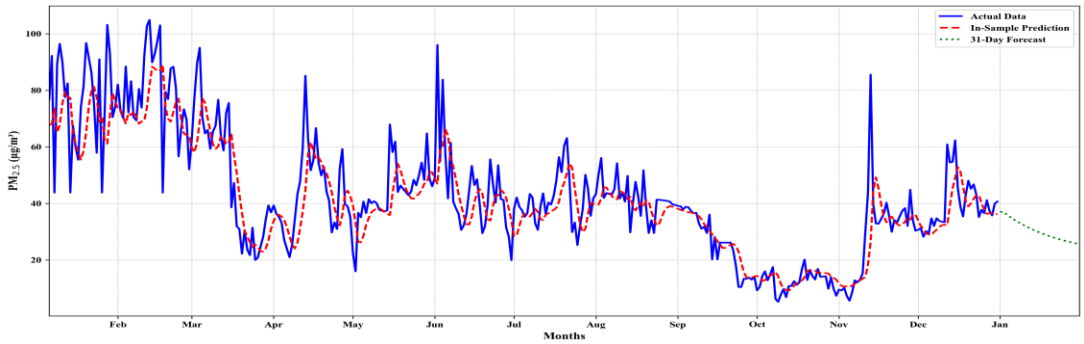

Figure 8. LSTM model forecast for the year 2023. The blue line represents the actual values. The red dashed line represents the modelled forecast value. The green line represents the 31 days out of sample forecast

Figure 6 and 7 present the SARIMA model forecasts for the years 2023 and 2024. The models yielded a Root Mean Square Error (RMSE) of 14.55 µg m^{-3} for the year 2023 and 22.86 µg m^{-3} for 2024, indicating a notable decline in predictive accuracy across the two periods. The increase in RMSE for 2024 suggests greater variability or reduced seasonality in the data, which may have affected the model's ability to capture the underlying temporal patterns. This further underscores the limitations of SARIMA in adapting to evolving or nonlinear dynamics, particularly under conditions of reduced seasonal regularity or abrupt shifts in pollution levels. Several studies have reported RMSE values comparable to the present findings, confirming the robustness of SARIMA models in air quality forecasting. Khamala et al. (2022) used an SARIMA $(1,0,0)(2,1,2)_{12}$ model for aerosol data over East Africa, capturing seasonal patterns effectively and suggesting applicability in broader environmental studies. Bunnang (2024) also applied SARIMA (3,1,3) $(1,1,2)_{12}$ to forecast PM_{10}, achieving an RMSE of 20.839 µg m^{-3}. A comparison with SARIMA-GARCH showed no significant improvement, favoring SARIMA. Similarly, Khanal et al. (2023) evaluated forecasting models for $PM_{2.5}$ in Kathmandu. SARIMA yielded the lowest RMSE of 16.991 µg m^{-3}, outperforming models like Prophet. Other similar studies carried out at different places include, Jain and Mandowara (2019), Mangayarkarasi et al. (2021), Mancini et al. (2022), Atoui et al. (2022), Sakib et al. (2023), and Khan et al. (2024).

LSTM Results

The LSTM model was implemented in Jupyter Lab using Tensor Flow and Keras. It is a stacked neural network designed to predict future $PM_{2.5}$ values based on past observations. The LSTM hyperparameters were selected through a validation based manual tunning process. The model architecture includes three stacked LSTM layers with 50 units each. The first two layers were designed to capture short- and medium-term temporal dependencies, the third layer served as a final temporal encoder before prediction. Dropout layers (rate: 0.3) were added after each LSTM layer to prevent overfitting. A dense layer with one neuron provides the final output. The models were programmed with three layers. The data were scaled to a 0-1 range using MinMaxScaler for efficient training and the train, validation, in 2023 and 2024, the data was divided into three sets. Training (Jan 1- Sep 12), validation (Sep 13-Nov 5), and testing (Nov 6 -Dec 31). A sliding window of size 5 was used to generate input sequences, where each sequence

predicts the next value. The model was compiled using the Adam optimizer and mean squared error loss, with RMSE as an evaluation metric. Early stopping was used to halt training after 10 epochs without validation improvement. Predictions were inverse-transformed and compared with actual values. **Figure 8** and **9** present the LSTM model forecasts for the years 2023 and 2024. The convergence of the model during training was evaluated by plotting the training and validation loss curves for 2023 and 2024, not shown.

The LSTM model for each timeline was run over 10 iterations to avert a particular weight initialization and they are reported in Table 5. It achieved RMSE values of 11.13 μg m^{-3} for 2023 and 17.44 μg m^{-3} for 2024, demonstrating strong predictive accuracy across both years. In comparison, the SARIMA model recorded higher RMSEs of 14.55 μg m^{-3} (2023) and 22.86 μg m^{-3} (2024), indicating reduced performance. This comparative evaluation in this case emphasizes that the LSTM outperformed SARIMA in modelling the nonlinear, stochastic behaviour of $PM_{2.5}$ concentrations, especially under conditions of temporal variability and seasonal shifts. The significant reduction in RMSE underscores LSTM's effectiveness in capturing long-range dependencies and adapting to complex atmospheric dynamics that SARIMA fails to represent adequately. Several studies have reported RMSE values comparable to the present findings, confirming the robustness of LSTM models. Seng et al. (2021) applied an LSTM-based MMSL model for $PM_{2.5}$ prediction in Beijing, achieving RMSEs of 11.15, 10.94, 15.62, and 12.22 μg m^{-3} at four representative stations. The model outperformed traditional methods like ARMA (RMSE: 13.96). In comparison, Tsokov et al. (2022) proposed a hybrid CNN–LSTM spatiotemporal model for hourly $PM_{2.5}$ prediction in Beijing, achieving RMSEs of 30.21 μg m^{-3} (Dongsi), 24.71 μg m^{-3} (Wanliu), and 27.39 μg m^{-3} (Changping) across three stations. The model incorporated optimized architectures via a genetic algorithm and utilized spatial data from surrounding stations. The ensemble of the top-performing models further improved results, with Wanliu achieving the lowest RMSE of 20.74 μg m^{-3}. Other similar studies carried out at different places include, Kim et al. (2019), Xayasouk et al. (2020) and Kristiani et al. (2022).

Model performance comparison

Figure 10 shows the results of the SARIMA and LSTM models' performance analysis. In 2023, the LSTM model demonstrated greater prediction power and flexibility to temporal fluctuations with a significantly lower root mean square error (RMSE) of 11.31 compared to the SARIMA model's 14.55 RMSE. Similarly, with RMSE values of 17.68 and 22.86 in 2024, respectively, the LSTM model continued to outperform SARIMA, despite an increase in error size. The LSTM beats SARIMA by 23.52% in 2023 and 23.71% in 2024, respectively, in percentage terms. The observed increase in RMSE between 2023 and 2024 for the SARIMA model indicates that its predictive power is declining over time. This variation suggests that the data's underlying temporal and seasonal dynamics have changed over the course of the two years. The inherent linearity and assumption of stationarity of the SARIMA model limit its ability to capture nonlinear and time-varying interactions in real-world data. SARIMA is unable to accurately represent abrupt or nonlinear fluctuations caused by other variables present in complex atmospheric and environmental systems, but it performs well for periodic and steady series. Incorporating exogenous variables. The model's performance did not significantly improve, according to preliminary testing. This implies that the short-term fluctuations in the data were not significantly impacted by these factors. By including such features, SARIMAX or hybrid deep learning models perform better when modeling long-term variation. The LSTM model not only captured the seasonal signatures of the unseen future, but also provided a clearer indication of the underlying trend, demonstrating its strength in modeling both short-term fluctuations and long-term temporal dynamics.

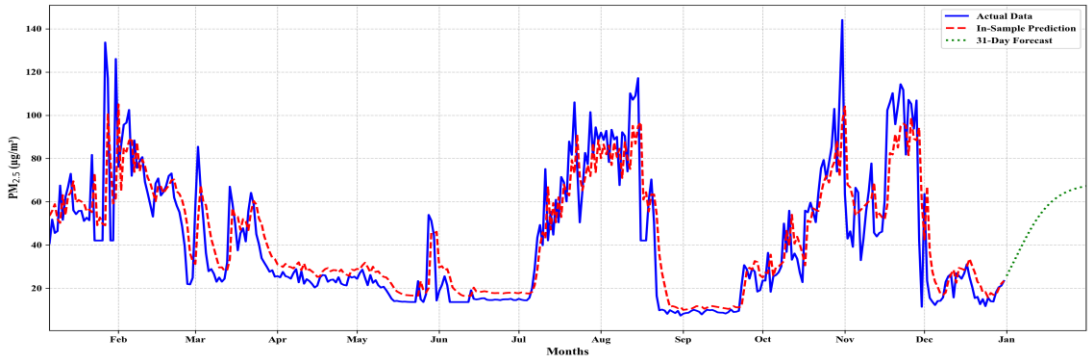

Figure 9. LSTM model forecast for the year 2024. The blue line represents the actual values. The red dashed line represents the modelled forecast value. The green line represents the 31 days out of sample forecast

Table 5. LSTM Models mean RMSE values obtained over 10 Iterations

Year	Number of runs	Mean RMSE	Standard deviation	Range (Min–Max)
2023	10	11.13	0.444	10.348 – 11.732
2024	10	17.44	0.182	17.180 – 17.688

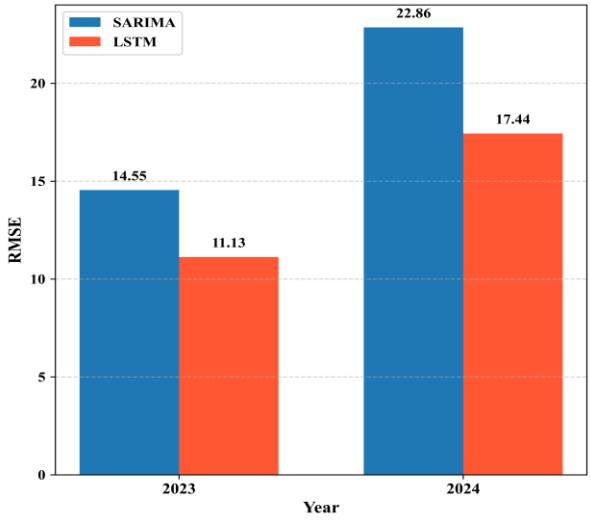

Figure 10. Bar graph comparison of RMSE values for the year 2023 and 2024. The blue bar represents SARIMA model the red bar represents the LSTM model. The RMSE values obtained from SARIMA model is higher the LSTM model in both timelines

CONCLUSIONS

The forecasting performance of parametric (SARIMA) and non-parametric (LSTM) models for $PM_{2.5}$ concentrations over Alandur in 2023 and 2024 was assessed in this study. SARIMA demonstrated greater uncertainty when extrapolating to unknown data, especially in 2024, despite its ability to capture seasonal linear patterns. However, the LSTM model performed better than SARIMA, particularly when it came to identifying non-linear patterns, as evidenced by lower RMSE values (11.13 and 17.44 for 2023 and 2024, respectively) than SARIMA (14.55 and 22.86). Both models were evaluated after imputing the 41-day missing period, the LSTM model achieved superior forecasting performance compared to the SARIMA model, demonstrating its greater capability to capture temporal dependencies even with imputed data. These findings demonstrate how LSTM can be used as an alternative for air quality forecasting in dynamic environmental conditions by non-linear dependencies in atmospheric time series. To enhance environmental risk assessment and early warning systems, the integration of deep learning with traditional statistical models serves as a promising approach.

Acknowledgements

The authors are grateful to the Director, Indian Institute of Geomagnetism, Navi Mumbai for constant support and extending the same to the Ministry of Science and Technology, Government of India. The authors are grateful to the referees for their valuable comments which enhanced the scientific value of this manuscript to several fold.

Author Credit Statement

J. Arul Asir: Programming, methodology, manuscript preparation; H. Johnson Jeyakumar: Supervision, manuscript review; C. P. Anil Kumar: Conceptualization, methodology, supervision, manuscript corrections, revision.

Data availability

Data available with Public domain bins of CPCB

Compliance with Ethical Standards

The authors declare that they have no conflict of interest and adhere to copyright norms.

References

Andreae, M. O., 2009. Correlation between cloud condensation nuclei concentration and aerosol optical thickness in remote and polluted regions. In: Atmos. Chem. Phys., 9, pp 542-556.

Asir, J. A., Jeyakumar, H. J. and Kumar, C. P. A., 2024. Wavelet Based Semblance Analysis of Anthropogenic Aerosol Control on Air Quality During the COVID-19 Pandemic Period. Aerosol Science and Engineering., 9, pp 140-151.

Atoui, A., Slim, K., Andaloussi, S. A., Moilleron, R. and Khraibani, Z., 2022. Time Series Analysis and Forecasting of the Air Quality Index of Atmospheric Air Pollutants in Zahleh, Lebanon. Atmosph.Climate Sci., 12(04), pp 728-749.

Bhattarai, H., Tai, A. P. K., Val Martin, M.V. and Yung, D. H. Y., 2024. Responses of fine particulate matter ($PM_{2.5}$) air quality to future climate, land use, and emission changes: Insights from modeling across shared socioeconomic pathways. Science of the Total Environment., 948, No. 174611.

Bisgaard, S. and Kulahci, M., 2011. Time Series Analysis and Forecasting by Example. Wiley. Wiley Series in Probability and Statistics., pp 48-50.

Box, G. E.P. and Jenkins, G. M. 1976, Time series analysis: forecasting and control, Holden-Day publications, San Fransico.

Brockwell, P. J. and Davis, R. A., 2016. Time Series: Theory and Methods, 3rd Ed., p 83.

Broersen, P. M. T., 2006. Automatic Autocorrelation and Spectral Analysis, 1st Ed., pp 90-95.

Bunnag, T., 2024. Forecasting PM_{10} Caused by Bangkok's Leading Greenhouse Gas Emission Using the SARIMA and SARIMA-GARCH Model. Int. J. Energy Economics and Policy., 14(1), pp 418-426.

Celo, V. and Dabek-Zlotorzynska, E., 2011. Concentration and Source Origin of Trace Metals in $PM_{2.5}$ Collected at Selected Canadian Sites within the Canadian National Air Pollution Surveillance Program. In Environmental Science and Engineering. Springer Science and Business Media, Deutschland GmbH., pp 19–38.

Chatfield, C., 1975. The Analysis of Time Series: Theory and Practice, 1st Ed, Springer New York, NY., p 60.

Chen, Y., Wild, O., Conibear, L., Ran, L., He, J., Wang, L. and Wang, Y., 2020. Local characteristics of and exposure to fine particulate matter ($PM_{2.5}$) in four Indian megacities. Atmosph. Environment: X., 5, No. 100052.

Cheung, H. C., Chou, C. C.-K., Lee, C. S. L., Kuo, W.-C. and Chang, S.-C., 2019. Hygroscopic properties and CCN activity of atmospheric aerosols under the influences of Asian continental outflow and new particle formation at a coastal site in East Asia., 20(10), 5911-5922.

Cromwell, J. B., Hannan, M. J., Labys, W. C. and Terraza, M., 1994. Multivariate tests for time series models. Sage Publications., Inc, pp 21-23.

Donahue, L. N., Posner, L. N., Westervelt, D. M., Li, Z., Shrivastava, M., Presto, A. A., Sulivan, R. C., Adams, P. J., Pandis, S. N. and Robinson, A. L., 2016. Where Did This Particle Come From? Sources of Particle Number and Mass for Human Exposure Estimates in Airborne Particulate Matter Sources, Atmospheric Processes and Health, ed. R. M. Harrison, R. E. Hester, and X. Querol, The Royal Society of Chemistry., 2016, pp 35-71.

Fan, J. and Yao, Q., 2005. Nonlinear time series. Nonparametric and parametric methods., p 9.

Farahat, A. and Abuelgasim, A., 2022. Effect of cloud seeding on aerosol properties and particulate matter variability in the United Arab Emirates. Int. J. Environmental Sci. Technol., 19(2), 951-968.

Fu, Y., Tai, A. P. K. and Liao, H., 2016. Impacts of historical climate and land cover changes on fine particulate matter ($PM_{2.5}$) air quality in East Asia between 1980 and 2010. In: Atmospheric Chemistry and Physic., Vol. 16(16), pp 10369-10383.

Gao, D., Zhao, B., Wang, S., Wang, Y., Gaudet, B., Zhu, Y., Wang, X., Shen, J., Li, S., He, Y., Yin, D. and Dong, Z., 2023. Increased importance of aerosol-cloud interactions for surface $PM_{2.5}$ pollution relative to aerosol-radiation interactions in China with the anthropogenic emission reductions. Atmosph. Chem. Phys., 23(22), 14359-14373.

Gautam, A. and Singh, V., 2020. Parametric versus non-parametric time series forecasting methods: A review. J. Engineering Sci. Technol. Rev., 13(3), 165-171.

Gu, Y., Fang, T. and Yim, S. H. L., 2024. Source emission contributions to particulate matter and ozone, and their health impacts in Southeast Asia. Environment Int., 186, 108578.

Guevara, M., 2016 Emissions of Primary Particulate Matter. In: Airborne Particulate Matter Sources, Atmospheric Processes and Health, ed. R. M. Harrison, R. E. Hester, and X. Querol, The Royal Society of Chemistry, pp.1-34.

Hodson, T. O., 2022. Root-mean-square error (RMSE) or mean absolute error (MAE): when to use them or not. Geoscientific Model Development., 15(14), 5481–5487.

Hyndman, R.J. and Athanasopoulos, G.,2014. Forecasting: principles and practice, 2nd Ed., pp 27-46, 157-180, 223-276.

Jain, S. and Mandowara, V. L., 2019. Study on Particulate Matter Pollution in Jaipur City. Int. J. Appl. Engineering Res., 14(3), 637-645.

Kaur, J., Parmar, K. S. and Singh, S., 2023. Autoregressive models in environmental forecasting time series: a theoretical and application review. Environmental Sci. Poll. Res., 30(8), 19617-19641.

Khamala, G. W., Makokha, J. W. and Boiyo, R., 2022. Statistical Analysis of Aerosols Characteristics from Satellite Measurements over East Africa Using Autoregressive Moving Average (ARIMA). OALib., 09(11), 1-14.

Khan, D. R., Patankar, A. B. and Khan, A., 2024. An experimental comparison of classic statistical techniques on univariate time series forecasting. Proced. Comput. Sci., 235, 2730-2740.

Khanal, I., Prakash Dhakal, O., Kumar Guragain, M., Karki, P. and Pandey, B., 2023. Proc. 14th IOE Graduate Conference Comparative Analysis of Time Series Forecasting Models for Predicting $PM_{2.5}$ level in Kathmandu : SARIMA, Prophet and XG-Boost., 14, pp 1182-1189.

Kim, H. S., Park, I., Song, C. H., Lee, K., Yun, J. W., Kim, H. K., Jeon, M., Lee, J. and Han, K. M., 2019. Development of a daily PM_{10} and $PM_{2.5}$ prediction system using a deep long short-term memory neural network model. Atmosph. Chem. Phys., 19(20), 12935-12951.

Kirchgässner, G. and Wolters, J., 2007. Introduction to Modern Time Series Analysis., pp15-19.

Kristiani, E., Lin, H., Lin, J. R., Chuang, Y. H., Huang, C. Y. and Yang, C. T., 2022. Short-Term Prediction of $PM_{2.5}$ Using LSTM Deep Learning Methods. Sustainability (Switzerland)., 14(4), No. 2068.

Kumar, U. and Jain, V. K., 2010. ARIMA forecasting of ambient air pollutants (O_3, NO, NO_2 and CO). Stochastic Environmental Res. Risk Assess., 24(5), 751-760.

Luo, J. and Gong, Y., 2023. Air pollutant prediction based on ARIMA-WOA-LSTM model. Atmosph. Poll. Res., 14 (6), No.101761.

Mancini, S., Francavilla, A., Graziuso, G. and Guarnaccia, C., 2022. An Application of ARIMA modelling to air pollution concentrations during covid pandemic in Italy. J. Phys. Conf. Ser., 2162(1), No. 012009.

Mangayarkarasi, R., Vanmathi, C., Khan, M. Z., Noorwali, A., Jain, R. and Agarwal, P., 2021. COVID19: Forecasting Air Quality Index and Particulate Matter ($PM_{2.5}$). Comput. Materials and Contin., 67(3), 3363-3380.

Megaritis, A. G., Fountoukis, C., Charalampidis, P. E., Denier Van Der Gon, H. A. C., Pilinis, C. and Pandis, S. N., 2014. Linking climate and air quality over Europe: Effects of meteorology on $PM_{2.5}$ concentrations. Atmosph, Chem. Phys., 14(18), 10283-10298.

Naveen, V. and Anu, N., 2017. Time Series Analysis to Forecast Air Quality Indices in Thiruvananthapuram District, Kerala, India. Int. J. Engineering Res. Appl., 07(06), 66-84.

Pal, A. and Prakash, P.K.S., 2017. Practical Time Series Analysis: Master Time Series Data Processing, Visualization, and Modelling Using Python. Packt Publishing Ltd., pp 47-83, 113, 193.

Pan, R., Song, J., Yi, W., Liu, J., Song, R., Li, X., Liu, L., Yuan, J., Wei, N., Cheng, J., Huang, Y., Zhang, X. and Su, H., 2024. Heatwave characteristics complicate the association between $PM_{2.5}$ components and schizophrenia hospitalizations in a changing climate: Leveraging of the individual residential environment. Ecotoxicology and Environmental Safety, 271, No. 115973.

Peixeiro, M., 2022. Time Series Forecasting in Python. Manning, Shelter Island., p 31.

Rebala, G., Ravi, A. and Churiwala, S., 2019. An Introduction to Machine Learning., pp 134-136.

Sakib, S. R., Sara, K. N., Rasel Tahmid, M. T. H., Rasel, H., Masudul, M., Asif, M. I. A., Aynul, M., Nahid, A. H., Rahman, S., Mridha, M. F. and Islam, A., 2023. Time Series Analysis and Forecasting of Air Quality Index of Dhaka City of Bangladesh., pp 67-76.

Seinfeld, J.H. and Pandis, S.N., 2016. Atmospheric chemistry and physics: from air pollution to climate change, 3rd Ed., p 350.

Seng, D., Zhang, Q., Zhang, X., Chen, G. and Chen, X., 2021. Spatiotemporal prediction of air quality based on LSTM neural network. Alexandria Engineering J., 60(2), 2021–2032.

Shumway, R. H. and Stoffer, D. S., 2011. Time Series Analysis and Its Applications, 4th Ed, Springer New York., p 1.

Singh, V., Singh, S. and Biswal, A., 2021. Exceedances and trends of particulate matter ($PM_{2.5}$) in five Indian megacities. Sci. Total Environment., 750, No.141461.

Slutzky, E., 1937. Summation of random causes as the source of cyclic processes, Econometrica., 5, 105–146.

Tai, A. P. K., Mickley, L. J., Jacob, D. J., Leibensperger, E. M., Zhang, L., Fisher, J. A. and Pye, H. O. T., 2012. Meteorological modes of variability for fine particulate matter ($PM_{2.5}$) air quality in the United States: Implications for $PM_{2.5}$ sensitivity to climate change. Atmosph. Chem. Phys., 12(6), 3131–3145.

Tsokov, S., Lazarova, M. and Aleksieva-Petrova, A., 2022. A Hybrid Spatiotemporal Deep Model Based on CNN and LSTM for Air Pollution Prediction. Sustainability Switzerland., 14(9), No 5104.

Walker, G., 1931 On periodicity in series of related terms. Proc. R. Soc. Lond. Ser., A 131(818), 518-532.

Wold, H., 1938. A Study in the Analysis of Stationary Time Series-Stockholm, Almqvist and Wiksel., pp 214-234.

Xayasouk, T., Lee, H. M. and Lee, G., 2020. Air pollution prediction using long short-term memory (LSTM) and deep autoencoder (DAE) models. Sustainability (Switzerland)., 12(6), No. 2570.

Yang, F., Tan, J., Zhao, Q., Du, Z., He, K., Ma, Y., Duan, F., Chen, G. and Zhao, Q., 2011. Characteristics of $PM_{2.5}$ speciation in representative megacities and across China. Atmosph. Chem. Phys., 11(11), 5207-5219.

Yim, S. H. L., Li, Y., Huang, T., Lim, J. T., Lee, H. F., Chotirmall, S. H., Dong, G. H., Abisheganaden, J., Wedzicha, J. A., Schuster, S. C., Horton, B. P. and Sung, J. J. Y., 2024. Global health impacts of ambient fine particulate pollution associated with climate variability. Environment Int., 186, No. 108537.

Yu, M., Xu, F., Hu, W., Sun, J. and Cervone, G., 2021. Using Long Short-Term Memory (LSTM) and Internet of Things (IoT) for Localized Surface Temperature Forecasting in an Urban Environment. IEEE Access., 9, 137406-137418.

Yule, G. U., 1927. On a Method of Investigating Periodicities in Disturbed Series, with Special Reference to Wolfer's Sunspot Numbers Phil. Trans. R. Soc. Lond., A, 226, 267-298

Zhang, B., Jiao, L., Xu, G., Zhao, S., Tang, X., Zhou, Y. and Gong, C., 2018. Influences of wind and precipitation on different-sized particulate matter concentrations ($PM_{2.5}$, PM_{10}, $PM_{2.5–10}$). Meteorol. Atmosph, Phys., 130(3), 383-392.

Zhang, Q., Meng, J., Quan, J., Gao, Y., Zhao, D., Chen, P. and He, H., 2012. Impact of aerosol composition on cloud condensation nuclei activity. Atmosph. Chem. Phys., 12(8), 3783–3790.

Zhao, B., Liou, K. N., Gu, Y., Li, Q., Jiang, J. H., Su, H., He, C., Tseng, H. L. R., Wang, S., Liu, R., Qi, L., Lee, W. L. and Hao, J., 2017. Enhanced PM2.5 pollution in China due to aerosol-cloud interactions. Scientific Rep., 7(1), No. 4453.

Received on: 30-6-2025; Revised on 16-12-2025; Accepted on 23-12-2025

J. Ind. Geophys. Union, 30(2) (2026), 136-141
https://doi.org/10.71122/JIGU.30(2)2026.0014

Estimation of site response beneath seismic stations in the vicinity of Jaitapur region (Ratnagiri district, Maharashtra), India, using H/V Spectral Ratios

M. Suneetha, H.V.S. Satyanarayana* and P. Pavan Kishore
CSIR-National Geophysical Research Institute, Hyderabad- 500007, India
*Corresponding author: hvsatya@ngri.res.in

ABSTRACT

Jaitapur village (16.59°N, 73.35°E) in Ratnagiri district, Maharashtra, India, is the site of a proposed Nuclear Power Plant that lies within the Konkan Plains of the Deccan Volcanic Province. The region has not experienced any moderate to large earthquakes (Mw ≥ 5.5) during the last five decades, except for a few moderate events (Mw ≈ 5.0) occurring more than 75 km from the Koyna–Warna seismic zone. At the request of the Nuclear Power Corporation of India Limited (NPCIL), a local seismological network was operated by CSIR–National Geophysical Research Institute (CSIR-NGRI), Hyderabad, from November 2004 to February 2012. In this study, ambient noise data recorded during January 2012 at six seismological stations (Mervy, Madban, Dassure, Mutat, Kharepatan, and Oni), were analysed using the Horizontal-to-Vertical Spectral Ratio (HVSR) technique to estimate the site response characteristics. The predominant resonance frequencies at these sites range from 1.5 to 6.0 Hz, with amplification factors between 0.6 and 9.0. Using an average shear-wave velocity of 350 m/s for the laterite and weathered basalt layer, the thickness of the near-surface geological layer was estimated to vary from approximately 17.5 m to 58.3 m. The results indicate significant spatial variability in site response across the region, reflecting lateral heterogeneity in the near-surface geology. These findings provide preliminary constraints on local site effects, which are important for seismic hazard assessment and infrastructure planning in and around the Jaitapur region.

Keywords: HVSR, Site response, Predominant frequency, Laterite, Jaitapur, Konkan plains, Deccan Volcanic Province.

INTRODUCTION

The 65 Ma Deccan Volcanic Province represents one of the largest continental flood basaltic eruptions on Earth, covering about 500,000 km² of western and central India (Widdowson and Cox, 1996). The basaltic sequence consists of multiple lava flows, separated locally by intertrappean sedimentary beds comprising limestone, shale, conglomerates, and sands. The region is structurally influenced by NE–SW and NW–SE trending lineaments, with fewer NNE–SSW features.

Historically, the Deccan volcanic region has experienced several damaging earthquakes in the past, including the 1967 Koyna (Mw 6.3), 1993 Killari (Mw 6.4), 1997 Jabalpur (Mw 5.8), 1956 Anjar (Mw 6.0), and 2001 Bhuj (Mw 7.7) events. The Killari and Bhuj earthquakes alone caused nearly 30,000 fatalities. Jaitapur (Figure 1) became an important location for seismic investigations following the proposal to establish a ~10,000 MW Nuclear Power Plant. At the request of NPCIL, CSIR-NGRI installed a micro-seismological network around Jaitapur in November 2004, which operated until February 2012. The network consisted of six stations: Mervy, Madban, Dassure, Mutat, Kharepatan, and Oni, equipped initially with short-period and later with broadband seismometers (Figure 1).

The stations are located between 16°–17°N and 73°–74°E along the Konkan coast bordering the Arabian Sea. Continuous waveform data recorded by this network were used in the present study to evaluate site response characteristics beneath each station using ambient noise measurements. Although the area lies close to the Koyna–Warna seismic zone, no events with magnitude greater than 2.0 were recorded during the network operation period (CSIR-NGRI internal communication to NPCIL).

METHODOLOGY

Horizontal to vertical spectral ratio (HVSR)

The horizontal to vertical spectral ratio (HVSR), was popularized as Nakamura's method (Nagoshi and Igarashi, 1971; Nakamura, 1989), who demonstrated that the ratio between horizontal and vertical ambient noise records is related to the fundamental frequency of the soil beneath the site and hence to the amplification factor. It can be represented as:

$$HVSR = \frac{\sqrt{H_{NS}^2 + H_{EW}^2}}{V}$$

Where the vertical, east-west, and north-south components of the waveform are denoted by V, H_{EW}, and H_{NS}, respectively.

It is generally accepted that the HVSR technique is effective in identifying the fundamental (natural) resonance frequency of a site. However, there is still debate regarding the extent to which the amplitude of the HVSR peak can be directly related to site amplification. Under idealized conditions dominated solely by fundamental-mode Rayleigh waves, the HVSR amplitude could theoretically increase indefinitely at the site resonance frequency, depending on subsurface properties. In realistic field conditions, however, the coexistence of additional vertical motion components at the same frequency constrains the amplitude of the HVSR peak. From this viewpoint, the peak amplitude primarily reflects the relative contribution of fundamental-mode Rayleigh waves within the ambient vibration wavefield (Ohmachi et al., 1991).

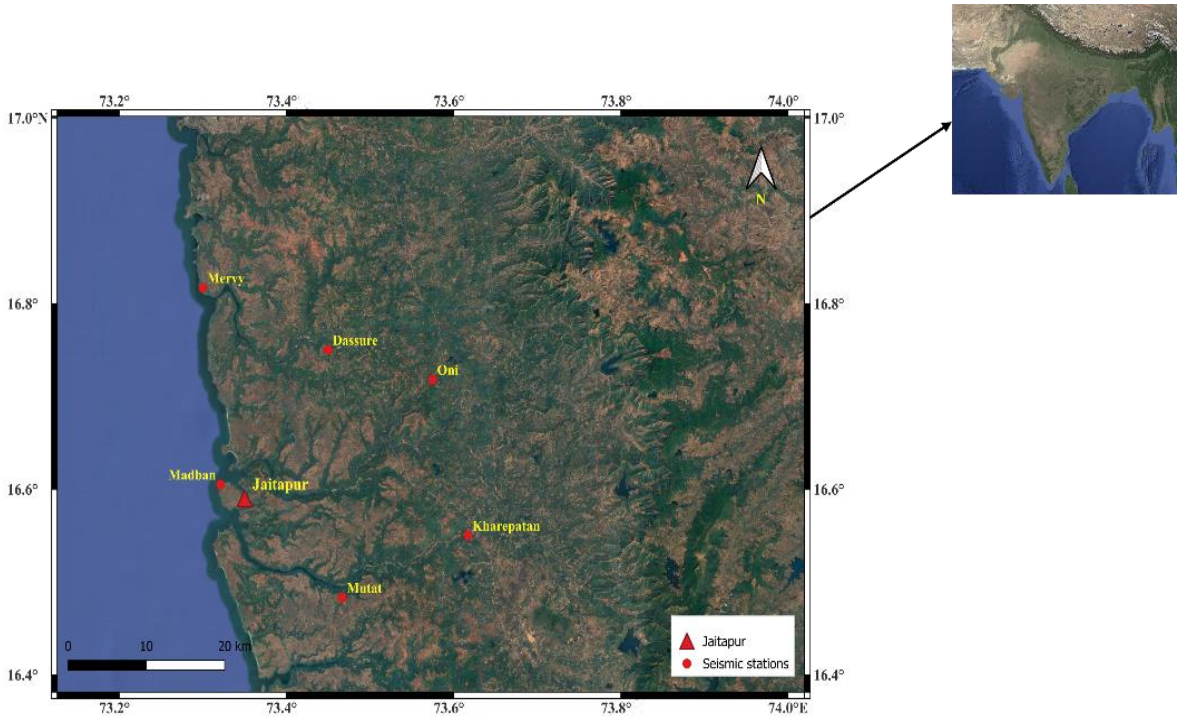

Figure 1. Location of the seismological stations operated under the Jaitapur seismological network, in Ratnagiri district of Deccan volcanic province

Despite this limitation, empirical evidence suggests a meaningful relationship between HVSR peak characteristics and earthquake damage. Observations from Thessaloniki indicate that structural damage tended to increase with decreasing HVSR peak frequencies and with increasing peak amplitudes (Panou et al., 2004). This finding is particularly significant, as it suggests that softer and thicker sedimentary deposits are associated with higher HVSR amplitudes and, consequently, greater seismic damage potential (Mundepi et al., 2009).

One of the major strengths of the HVSR method lies in its operational simplicity and cost efficiency. Measurements can be conducted rapidly, at virtually any location and time, without the need for active sources. Moreover, the method provides a direct estimate of the fundamental resonance frequency or period of sedimentary layers without requiring detailed prior knowledge of subsurface geology or shear-wave velocity structure.

Data acquisition and processing

In the present study, the data from the tri-axial broad-band seismometers of model Reftek 151-60 were used to estimate the HVSR. The Data Acquisition System (DAS) are of model Reftek 130-01/3 which acquires continuous seismic data at 100 samples per second and archives the data in a proprietary 'Reftek' (rt) format. The continuous waveform data recorded in Reftek (rt) format were first converted into SEISAN (Seismic Analysis) format, which is a widely used earthquake analysis system developed by the University of Bergen for seismic data processing, and subsequently transformed into Simple Alignment Format (SAF) for further analysis to be compatible with the processing software for HVSR. Site response estimation was carried out using the GEOPSY software package (Wathelet et al., 2020). The horizontal-to-vertical spectral ratio (H/V) was computed from three-component ambient noise recordings by applying a time window of 60 s to ensure sufficient frequency resolution in the Fourier spectra while maintaining signal stationarity. Longer windows improve spectral stability and allow reliable estimation of low-frequency resonance peaks, which are essential for identifying fundamental site frequencies associated with deeper sedimentary layers. However, for the computation of HVSR the raw data for durations of 6 hours each at the seismological station was considered. Fourier amplitude spectra were smoothed using the approach proposed by Konno and Ohmachi (1998), with additional considerations following Tokeshi and Sugimura (1998). In the present analysis, the quadratic mean of the two horizontal components was adopted to represent the horizontal motion. The final H/V curve for each station was obtained by averaging the spectral ratios calculated over all selected time windows using GEOPSY software package. The site's fundamental or resonance frequency was then determined as the mean value derived from the ensemble of processed noise windows, following the methodology outlined by Nakamura (2000).

Overall, this procedure demonstrates that site response characteristics can be effectively evaluated using ambient vibration recordings acquired with a three-component broadband seismometer. The recorded waveforms were processed in GEOPSY to extract spectral amplitudes and predominant frequency parameters, which were subsequently used to quantify site-specific resonance behavior and seismic amplification levels.

Site amplification

Site amplification represents one of the parameter governing the extent of damage during strong earthquakes, and numerous recent investigations have highlighted the significant influence of near-surface geological conditions on recorded ground motions. The overall site response at a given location arises from the combined effects of several factors, including the mechanical properties of subsurface materials, basin and bedrock topography, groundwater conditions, and the amplification and persistence of seismic waves propagating through the soil column (Xu and Wang, 2021). Among these controlling parameters, the impedance contrast and geometrical relationship between the underlying bedrock and the overlying sedimentary layers (Widdowson and Cox, 1996), play a dominant role in modifying seismic wave propagation. In the present study, ambient vibration data acquired under varying seasonal conditions like rainy, winter, and summer periods, were analysed to obtain a robust and representative assessment of site response characteristics.

The amplitude and frequency content of earthquake-induced ground motions are strongly influenced by near-surface material properties and their spatial configuration, through physical processes such as resonance-based selective filtering, energy damping, and wave-field focusing (Yamazaki and Ansary, 1997). Furthermore, the earthquake hazard assessment commonly incorporate attenuation relationships and site amplification factors that account for source and crustal effects, as well as modifications introduced by surface geology, soil layer thickness, and nonlinear soil behaviour. Nonlinear soil behaviour refers to the reduction of shear modulus and increase in damping of soil materials under strong ground shaking, typically observed during moderate to large earthquakes (Mw $\geq$ 5.5). Such behaviour results in shifts of resonance frequency and amplification levels due to strain-dependent soil response.

Estimation of shallow geological layer thickness

In view of the local geology, the near surface layer is comprised of laterite soil which is compact in nature and as per National Earthquake Hazards Reduction Programme (NEHRP) site classification, and has the maximum average shear wave velocity (Vs) in the range of 180-360 m/s. Hence in the present study, the average V_S of ~ 350 m/s is considered for the shallow geological layer and an effort has been made to estimate the thickness of laterite soils / weathered rock beneath each seismic station through a simplified approach. Assuming a single layer over half space model, the average thickness of shallow geological layer can be estimated from equation.

$$H = V_{av}/4*f_{H/V}$$

Where, V_{av} is Average shear wave velocity (Vs); H is the layer thickness; f is the fundamental resonance frequency (Bard, 2000).

This is an average estimate of the soil thickness based on the observed resonance frequency and an average shear-wave velocity in Jaitapur region based on the assumption of an underlying 2D model. Using the average shear wave velocity (Vs) structure for the area, the soil thickness around Jaitapur area has been computed using this empirical relationship. This leads to very large variation in the soil thickness over short distances, which would result in 2-D and 3-D effects of the basin response in which case, the distinct resonance frequencies may differ from the herein found average Nakamura estimate (Bard, 2000).

RESULTS AND DISCUSSION

The estimated HVSR amplification levels and fundamental frequencies for all stations are summarized in Table 1 and representative spectra are shown in Figure 2. Representative examples of raw ambient noise waveforms from each station were examined to ensure adequate signal quality, stationarity, and absence of transient disturbances prior to HVSR processing. Amplification values range from 0.6 to 9.0, while predominant frequencies vary from 1.5 to 6.0 Hz, indicating strong spatial variability.

Lower resonance frequencies (1.5 Hz) at Kharepatan and Oni suggest the presence of thicker and softer sedimentary layers, whereas higher frequencies (5–6 Hz) at Madban and Mutat, indicate relatively thinner near-surface layers. Using Vs = 350 m/s, the estimated thickness of the lateritic/weathered basalt layer ranges from approximately 17.5 m to 58.3 m. Such average shear-wave velocity used for the laterite/weathered layer, is in accordance with NEHRP site classification for similar geological conditions in the region. Although coastal regions often exhibit thicker sediments, local geological controls such as erosional surfaces, lateritic weathering, and buried paleo-topography, can result in greater sediment thickness inland. The observed inland thickening may reflect localized structural depressions. However, no independent gravity or magnetic data are currently available to confirm basin geometry.

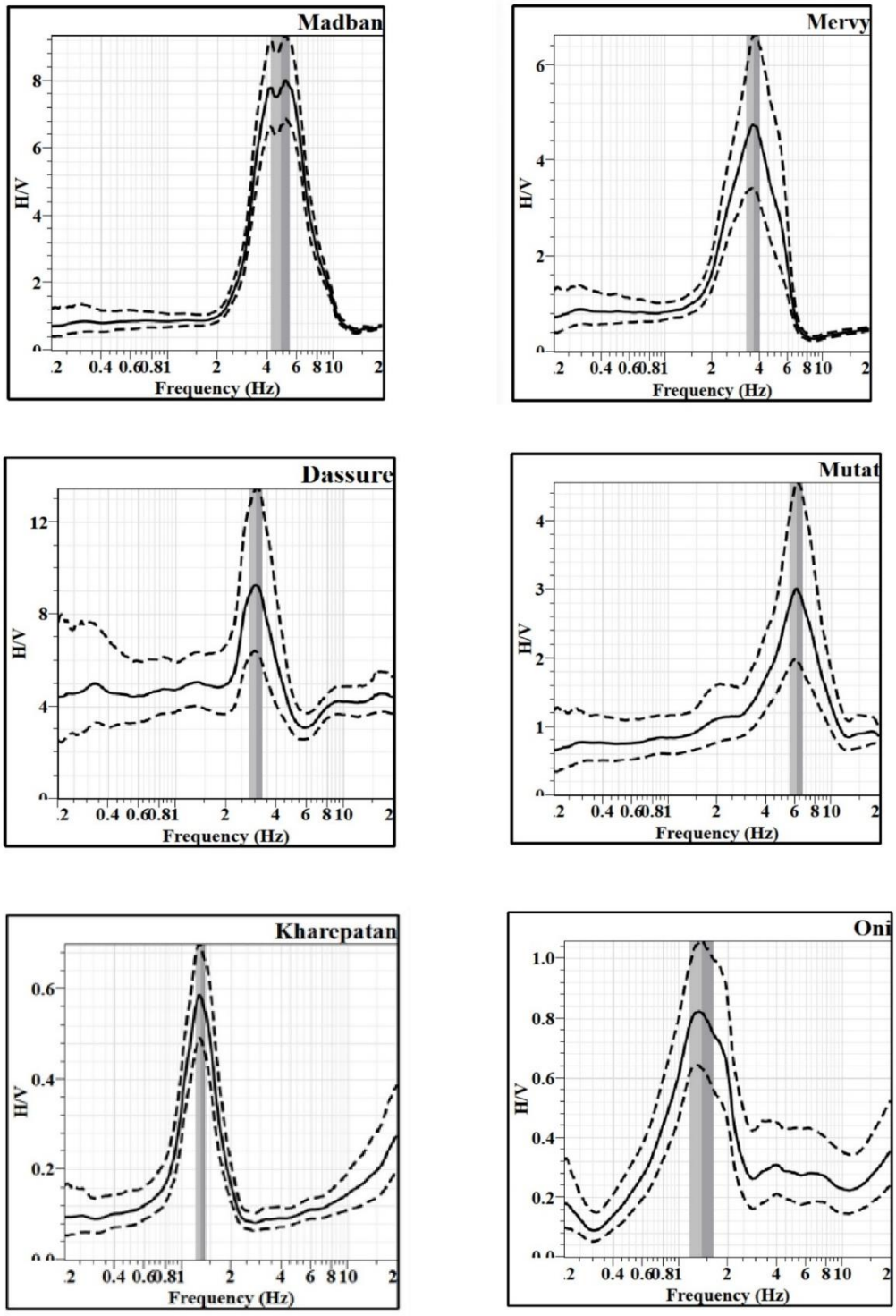

— : Mean (average) H/V spectral ratio

▪▪▪ : ±1 standard deviation of H/V spectral ratio

: Fundamental resonance frequency (f_0)

Figure 2. H/V Spectral ratio plots at different seismic stations around the Jaitapur region

Table 1. The estimated H/V response amplification level and soil/laterite thicknesses at seismic station around the Jaitapur region

Station	Lat ° (N)	Long °(E)	Amplification	Average HVSR $f_{H/V\ (Hz)}$	Thickness (h) from HVSR (m)
Madban	16.605	73.321	7.5	5.0	17.5
Mervy	16.817	73.300	4.5	4.0	21.8
Dassure	16.750	73.450	9.0	3.0	29.1
Mutat	16.483	73.467	2.8	6.0	14.5
Kharepatan	16.550	73.617	0.58	1.5	58.3
Oni	16.718	73.575	0.83	1.5	58.3

Table 1 illustrates the spatial variability of the near-surface layer that consists predominantly of lateritic soil and weathered basaltic material around the Jaitapur region. Near the coastal reference point, the shallow geological layer cover is relatively thin, ranging between ~10–20 m, which reflects the presence of shallow soil and limited near-surface weathering. Moving inland, the soil thickness gradually increases by ~30–40 m, indicating the development of a moderately thick weathered layer. A pronounced increase in depth is observed at the farthest inland location, where soil / laterite thickness reaches approximately 58.3 m. This significant deepening corresponds to a low HVSR fundamental frequency and suggests the presence of a localized structural basin or depression filled with consolidated material.

CONCLUSIONS

This study presents an ambient noise–based assessment of site response characteristics at six seismological stations in the Jaitapur region using the HVSR technique. The estimated predominant frequencies range from 1.5 to 6.0 Hz, while amplification factors vary between 0.6 and 9.0, indicating substantial spatial variability in near-surface geological conditions. Using an average shear-wave velocity of 350 m/s, the thickness of the laterite and weathered basalt layer was estimated to range from approximately 17.5 m to 58.3 m, with an uncertainty of about ±20% due to assumptions in velocity structure and one-dimensional layering. The lower resonance frequencies observed at Kharepatan and Oni suggest the presence of thicker and softer near-surface deposits, compared to other sites. Although no independent geophysical data (e.g., gravity or magnetic surveys) are currently available to confirm the presence of a structural basin, the HVSR results indicate possible lateral variations in subsurface geometry. These findings highlight the importance of considering local site effects in seismic hazard assessment for the Jaitapur region. Further, the Nakamura HVSR method provides a rapid and cost-effective means of estimating fundamental site frequencies; however, it does not account for nonlinear soil behaviour during strong ground shaking. Therefore, the results presented here should be regarded as a first-order approximation that can be refined through future geotechnical, geophysical, and borehole investigations.

Acknowledgement

Authors thankfully acknowledge the Nuclear Power Corporation of India Limited for supporting the establishment of micro seismic network around Jaitapur and Director, CSIR-National Geophysical Research Institute, Hyderabad for providing the necessary facilities and permission to publish the paper. The corresponding author acknowledges the services of U Gowrishankar, P Senthil Kumar and M Kousalya of CSIR-NGRI. The authors acknowledge the valuable suggestions of Dr O. P. Pandey.

Author Credit Statement

M. Suneetha is credited with the data processing, interpretation and drafting of the manuscript. HVS Satyanarayana is credited with the overall responsibility as a principal investigator of the project including the site selections, network establishment, micro seismic data analysis etc. P. Pavan Kishore is credited with study information, interpretation, drafting and review.

Data availability

The data used in this study is available with the corresponding author in the capacity of principal investigator from the CSIR–National Geophysical Research Institute (CSIR-NGRI).

Compliance with ethical standards

The authors declare no conflict of interest and adhere to copyright norms. This study provides preliminary site-response information but does not directly influence the engineering design of the Nuclear Power Plant, which is based on comprehensive geotechnical, seismic, and regulatory assessments.

REFERENCES

Bard, P.Y., 2000. Lecture notes on ‘Seismology, Seismic Hazard Assessment and Risk Mitigation’. International Training Course, Potsdam,160.

Konno, K. and Ohmachi, T., 1998. Ground motion characteristics estimated from spectral ratio between horizontal and vertical components of microtremors. Bull. Seismol. Soc. Am., 88, 228-241.

Mundepi, A.K., Lindholm, C. and Kamal, 2009. Soft soil using Horizontal to Vertical Spectral Ratio (HVSR) for seismic hazard assessment of Chandigarh City in Himalayan foothills, North India. J. Geol. Soc. India, 74, 551-558.

Nakamura, Y., 1989. A method for dynamic characteristics estimation of sub surface using microtremor on the surface. Railway Technical Research Institute Report, 3025-3033.

Nakamura, Y., 2000. Clear identification of fundamental idea of Nakamura's technique and its applications. In: Proc. 12th world conference on earthquake engineering, 2656, 1-8.

Nogoshi, M. and Igarashi, T., 1971. On the Amplitude Characteristics of Microtremor. J. Seism. Soc. Japan, 24, 26-40.

Ohmachi, T., Nakamura, Y. and Toshinawa, T., 1991. Ground motion characteristics the San Francisco Bay area detected by microtremor measurements. Proc. 2nd Int. Conf. on Recent Advances in Geotechniques. Earthquake Engineering and Soil Dynamics. San Louis, Missouri. 11-15, 1643-1648

Panou, A. A., Theodulidis, N., Hatzidimitriou, P. M., Papazachos, C. B. and Stylianidis, K., 2004. Ambient noise Horizontal-to-vertical spectral ratio for assessing site effects in urban environments: the case of thessaloniki city (northern Greece). Bull. Geol. Soc. Greece, 36(3), 1467-1476.

Tokeshi, J.C. and Sugimura, Y., 1998. A comparison of the Fourier phase spectral method with the Nakamura technique for a horizontally layered structure. In: Proc. XIth European Conference on Earthquake Engineering, Paris, September (6-11).

Wathelet, M., Chatelain, J.- L., Cornou, C., Giulio, G. D., Guillier, B., Ohrnberger, M. and Savvaidis, A., 2020. Geopsy: A User-Friendly OpenSource Tool Set for Ambient Vibration Processing. Seismol. Res. Lett., 91, 1878–1889,

Widdowson, M. and Cox, K. G., 1996. Uplift and erosional history of the Deccan Traps, India: Evidence from laterites and drainage patterns of the Western Ghats and Konkan coast. Earth Planet. Sci. Lett. 137, 57–69.

Xu, R. and Wang, L., 2021. The horizontal-to-vertical spectral ratio and its applications. EURASIP J. Adv. Signal Process 2021(1), 75.

Yamazaki, F. and Ansary, M.A., 1997. Horizontal-to-vertical spectrum ratio of earthquake ground motion for site characterization. Earthq. Engineering and structural dyn., 26, 671-689.

Received on: 23-12-2025; Revised on 25-01-2026; Accepted on 28-01-2026

J. Ind. Geophys. Union, 30(2) (2026), 142-147
https://doi.org/10.71122/JIGU.30(2)2026.0015

Acanthite (Ag_2S) as an indicator of late-stage silver mineralization in the Zawar Pb–Zn system, Rajasthan, India: Insights from Scanning Electron Microscopy (SEM) and Energy-Dispersive X-ray Spectroscopy (EDS) microtextural studies

Sima Gorai*, Bulusu Sreenivas and T. Vijaya Kumar
[1]CSIR-National Geophysical Research Institute, Uppal Road, Hyderabad 500007, India.
*Corresponding author: sima.geol90@gmail.com

ABSTRACT

This study investigates the occurrence, microtextural characteristics and chemical composition of acanthite (Ag_2S) in the Zawar deposit, Rajasthan, India, to understand the conditions and the paragenetic relationship of silver mineralization in this classic carbonate-hosted Mississippi Valley Type (MVT) ore deposit. Silver in Zawar, traditionally considered a by-product of lead (Pb) and zinc (Zn) extraction, is shown here to occur as late-stage acanthite developed as distinctive veins and star-shaped aggregates along the weak zones and micro-fractures within earlier-formed pyrite. Scanning Electron Microscopy (SEM) reveals that these acanthite crystals are confined to structurally controlled micro-openings, indicating precipitation from late stage fluids that exploited pre-existing sulfide microstructures. Energy-dispersive X-ray spectroscopy (EDS) confirms a dominantly silver (Ag) and, sulfur (S) composition, and only minor iron (Fe) and calcium (Ca), suggesting limited solid solution or sub-microscopic inclusions of associated sulfides. The dominance of monoclinic acanthite in carbonate-hosted, structurally focused sites, is fully consistent with the deposition from basinal brines at low temperatures. These textural and geochemical observations, collectively indicate that silver enrichment at Zawar is genetically linked to the waning stages of MVT-type hydrothermal activity.

Keywords: Silver, Acanthite, Hydrothermal mineralization, Micro-textural Studies, Zawar.

INTRODUCTION

Globally, silver production is dominated by Australia, Mexico, China, Peru, and Russia, while India, though among the top three consumers, contributes only a small share of the 6,10,000 tonnes worldwide reserve in 2023, indicating a heavy reliance on imports (Indian Minerals Yearbook, 2023). Total reserve of silver in India is about 7700 tonnes, mainly found as a by-product from lead, zinc, copper, and gold refining in Rajasthan, Jharkhand, and Andhra Pradesh, and its strategic importance is growing with rising industrial demand in electronics, solar energy, and storage sectors. The Zawar deposit of Rajasthan, is one of the economically significant carbonate-hosted Pb-Zn orefields and an important historical centre for silver production (Haldar, 2004). Mining in this belt has been active since at least medieval times, with archaeological evidence for large-scale lead zinc smelting, from poly metallic ores in the Zawar hills. Modern operations by Hindustan Zinc Limited (HZL) at Mochia, Balaria, Zawarmala and Baroi, continue to produce Zn–Pb ore with silver recovered as a significant by-product. Although the principal ore minerals are galena (PbS) and sphalerite (ZnS), silver is hosted both in solid solution within these sulphides and in discrete silver minerals. Classical mineralogical work on Zawar describes small amounts of argentite and native silver associated with the main sulphide assemblage (Mookherjee, 1964).

Generally, Silver sulfide (Ag_2S) occurs in three temperature-dependent polymorphs that share the same chemical composition but differ in structure and stability (Sadovnikov et al., 2015). At low temperatures, the stable phase is α-Ag_2S (acanthite), which has a monoclinic structure with relatively ordered Ag^+ positions and forms the common silver ore mineral in most deposits. On heating above ~177 °C, acanthite transforms to β-Ag_2S (argentite), a high-temperature polymorph with a cubic (isometric) structure in which Ag^+ ions become partially disordered and highly mobile in nature, this phase is usually preserved only as acanthite pseudomorphs after argentite because it inverts on cooling (Sadovnikov et al., 2015). At still higher temperatures (typically above ~600 °C under experimental conditions), Ag_2S transforms further to γ-Ag_2S, another high-symmetry cubic phase with even greater Ag^+ mobility and structural disorder. The objective of this study is to characterize the morphology, microtextural setting, and chemical composition of acanthite in the Zawar deposit using SEM and EDS analyses, in order to understand the nature of silver mineralization

GEOLOGY OF THE STUDY AREA

The Zawar deposit lies within the highly mineralised Proterozoic Aravalli Supergroup of the Aravalli Craton in NW India (Deb et al., 1989). Stratigraphically, mineralisation occurs in a siliciclastic–dolomitic carbonate succession of the Middle Aravalli Group, within the Zawar Formation (Mukherjee and Bhattacharya, 2021). The belt is characterised by two major superposed folds, the hook-shaped Main Zawar Fold (MZF) and the antiformal anticline Zawarmala Fold, developed under lower greenschist facies metamorphism and hosting several important mines, including Balaria, Mochia Magra, Baroi Magra and Zawarmala (Roy, 1995). The regional geology of the area is depicted in Figure 1.

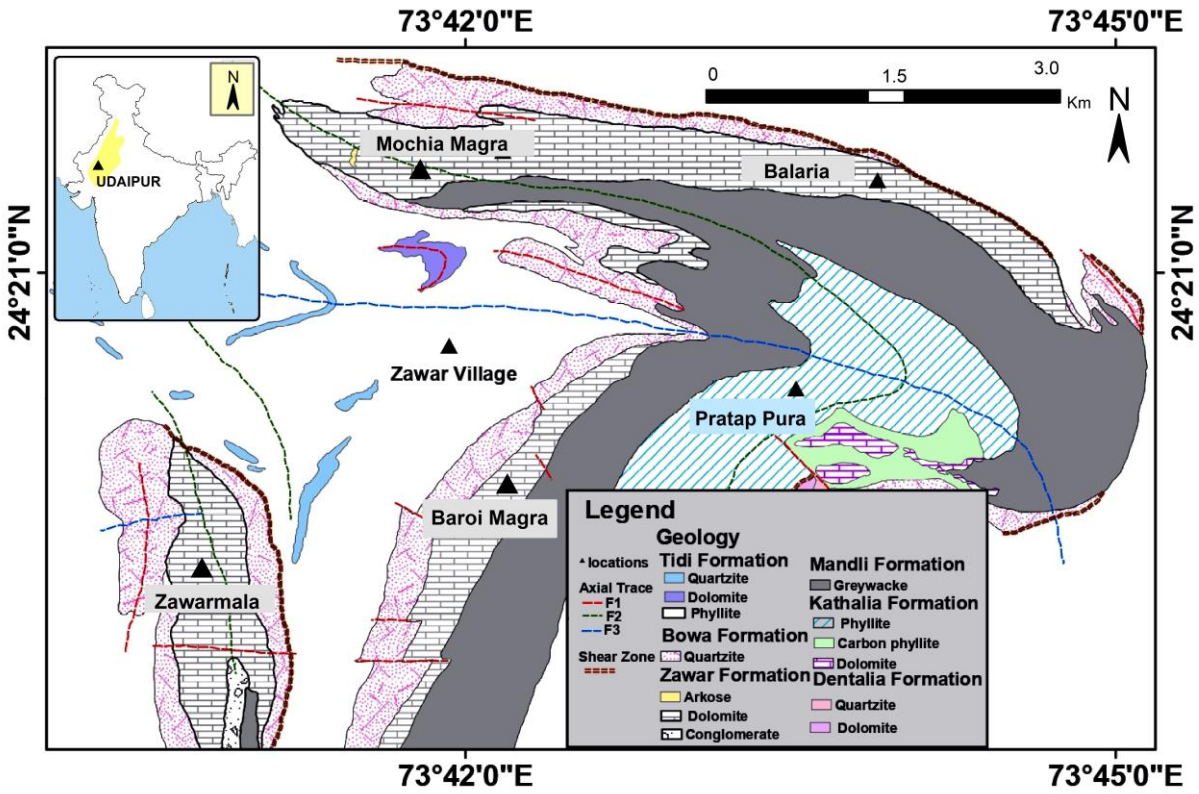

Figure 1. Geological map of the Zawar Deposit, together with the sampling locations, which are shown as solid triangles (after Roy, 1995).

METHODOLOGY

Sampling details

The samples have been extracted from various mining sites of the Zawar deposit that include Balaria (24°21'36.35"N, 73°44'14.26"E), Mochia Magra (24°21'48.72"N, 73°43'04.73" E), Baroi Magra (24°20'59.97" N, 73°42'18.06"E), and Zawarmala (24°20'08.45"N, 73°41'19.88"E), which has been marked on the geological map **(**Figure 1**).**

Scanning Electronic Microscope (SEM) Study

SEM study was carried out to examine the micro-textural and morphological features of the samples. Polished thick sections (>100 µm) were carbon-coated to ensure surface conductivity and minimize charging effects. SEM imaging was performed at an accelerating voltage (HV) of 20 kV, which provided optimal resolution and depth of field for distinguishing fine mineral phases and textural relationships. 660 nm spot sizes are used for the analysis, with working depth 14.97 to 18.25 mm. Backscattered Electron (BSE) images were acquired using a TESCAN VEGA3 scanning electron microscope, operated with the TESCAN control software, which facilitated precise control of imaging parameters and high-quality documentation of microstructural features.

Energy-dispersive X-ray spectroscopy (EDS) Study

EDS study was employed to determine the qualitative and quantitative chemical composition of selected mineral phases. The EDS system is integrated with the SEM , enabling point, line, and area analyses directly on the imaged regions of interest. Measurements were carried out at an accelerating voltage of 20 kV, which is suitable for exciting characteristic X-rays of the major and minor elements present in the samples. Elemental spectra were acquired and processed using Bruker ESPRIT software, which applies appropriate peak deconvolution and matrix corrections to improve analytical reliability and generate consistent compositional data.

RESULTS AND DISCUSSION

The development of star-shaped acanthite crystals has been observed within the Zawar deposit (Figure 2a). These crystals are commonly associated with pyrite (Py) and are predominantly localized along fractured zones within the Py grains, suggesting that the acanthite formation was controlled by microstructural pathways during late-stage mineralization. This star-shaped texture reflects rapid quench crystallisation triggered by the sudden interaction of hot, Ag-rich hydrothermal fluids with a cooler Py substrate, focusing mineral precipitation along fracture-controlled weak zones (Figure 2b). The Zawar deposit is characterised by sphalerite,

galena, and pyrite as the dominant sulfide mineral assemblage, typical of Mississippi Valley–type (MVT) mineralisation (Gorai et al., 2025 a, b). Hydrothermal alteration zones-is also observed in the phyllites from the hinge of the MZF, associated with the epithermal monazite mineralization (Gorai et al., 2024). MVT deposits typically form from low-temperature, basinal brines that migrate through carbonate host rocks and precipitate ore minerals in structurally controlled sites such as fractures, faults, and dissolution cavities (Misra, 2000). The localization of acanthite in micro-fractures of Py, suggests late-stage precipitation from Ag-bearing hydrothermal fluids that exploited these structural weaknesses, consistent with the open-space filling textures typical of MVT systems (**Figure 2c, d**). Furthermore, the close association with Py, a common sulfide in MVT environments, indicates that silver was likely introduced during the terminal stages of mineralization when fluid chemistry favoured Ag–S complex stability, leading to acanthite deposition. The presence of acanthite in Zawar, can be directly linked to the low-temperature hydrothermal conditions. In MVT systems, ore deposition typically occurs from basinal brines at temperatures between 100 °C and 200 °C, within carbonate host rocks under low-pressure conditions (Maghfouri and Choulet, 2021). Argentite (Arg), the high-temperature cubic polymorph of Ag_2S, becomes unstable below ~173 °C and inverts to monoclinic acanthite upon cooling (Sadovnikov et al., 2015). Therefore, the dominance of acanthite rather than Argentite in Zawar, indicates that silver precipitation occurred during the late, low-temperature stages of hydrothermal activity .

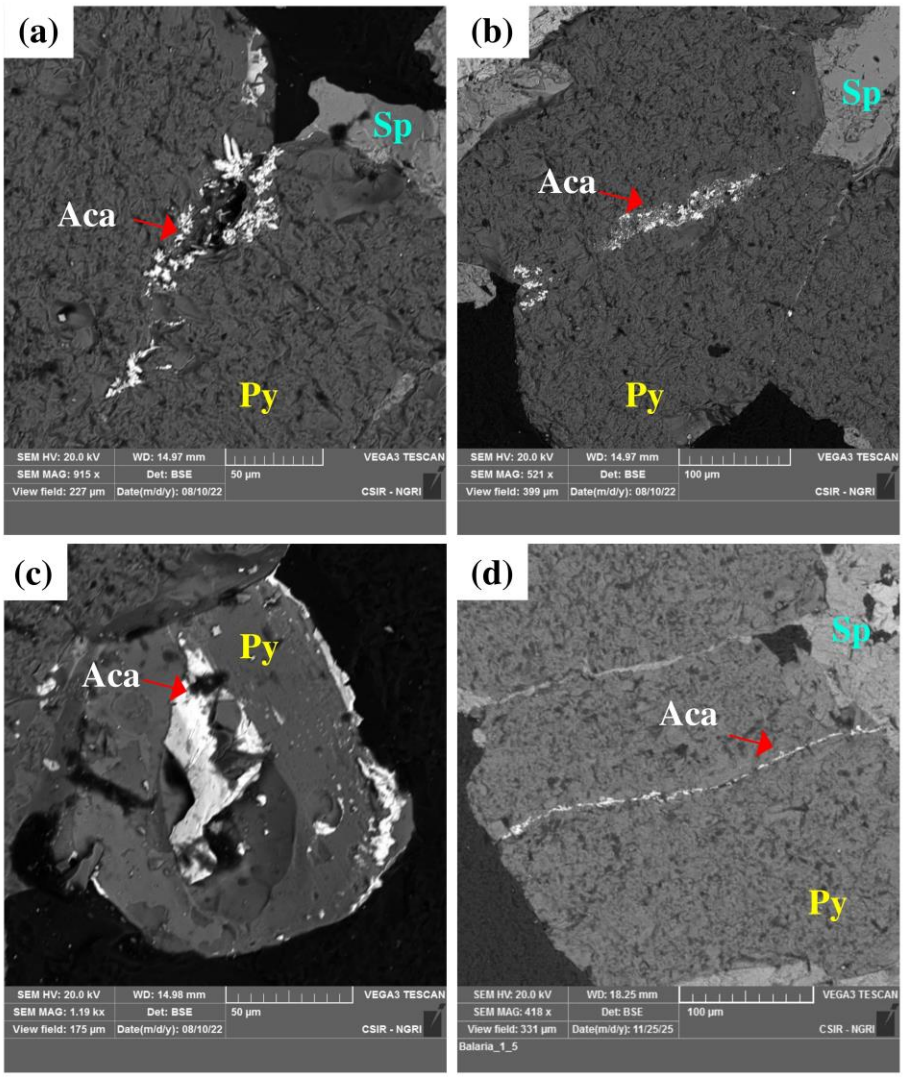

Figure 2. SEM images illustrating the textural relationships of acanthite (Aca). **(a)** Star texture of acanthite (Aca) developed in the micro fracture of pyrite (Py), is indicative of rapid crystallization, **(b)** Vein like acanthite (Aca) emplaced along structurally weak zones of pyrite (Py) associated with sphalerite (Sp), **(c)** Acanthite (Aca) infilling depressions along the surface of pyrite (Py), and **(d)** Thin acanthite (Aca) vein occupying a fracture zone within pyrite (Py).

EDS analyses of acanthite crystals show that they are dominantly composed of Ag and S. Minor to trace amounts of other elements (Ca, Fe), are occasionally detected, suggesting limited solid-solution or sub-microscopic inclusions of associated sulfides. The elemental compositional map of the acanthite grains, obtained from EDS analyses is shown in Figure 3a-**d**. The EDS spectra as shown in Figure 4a, b confirm that the analysed grains correspond to acanthite and supports the silver sulfide phase in the ore assemblages. Moreover, the association of acanthite with Py in fracture zones (Figure 2), further supports a late-stage precipitation, where descending Ag-bearing fluids interacted with earlier sulfides and carbonates under cool, reducing conditions, stabilizing acanthite as the final Ag-sulfide phase (Dill, 2010). Acanthite typically forms in cool, reducing environments where sulfur-rich, low-temperature fluids interact with Ag bearing solutions (Dill, 2010). As the temperature drops and conditions become more chemically reducing, Ag prefers to bond with S, rather than remain dissolved in the fluid. This causes acanthite to precipitate in veins, open spaces, or along fractures within earlier-formed sulfides and carbonates. Such late-stage, deposition over the cool surfaces of the early formed sulfides, often produces glass like quench textures, marking the final silver-enrichment phase in many hydrothermal ore systems. This mineralogical evidence reinforces the interpretation of the deposition of silver in the Zawar deposit.

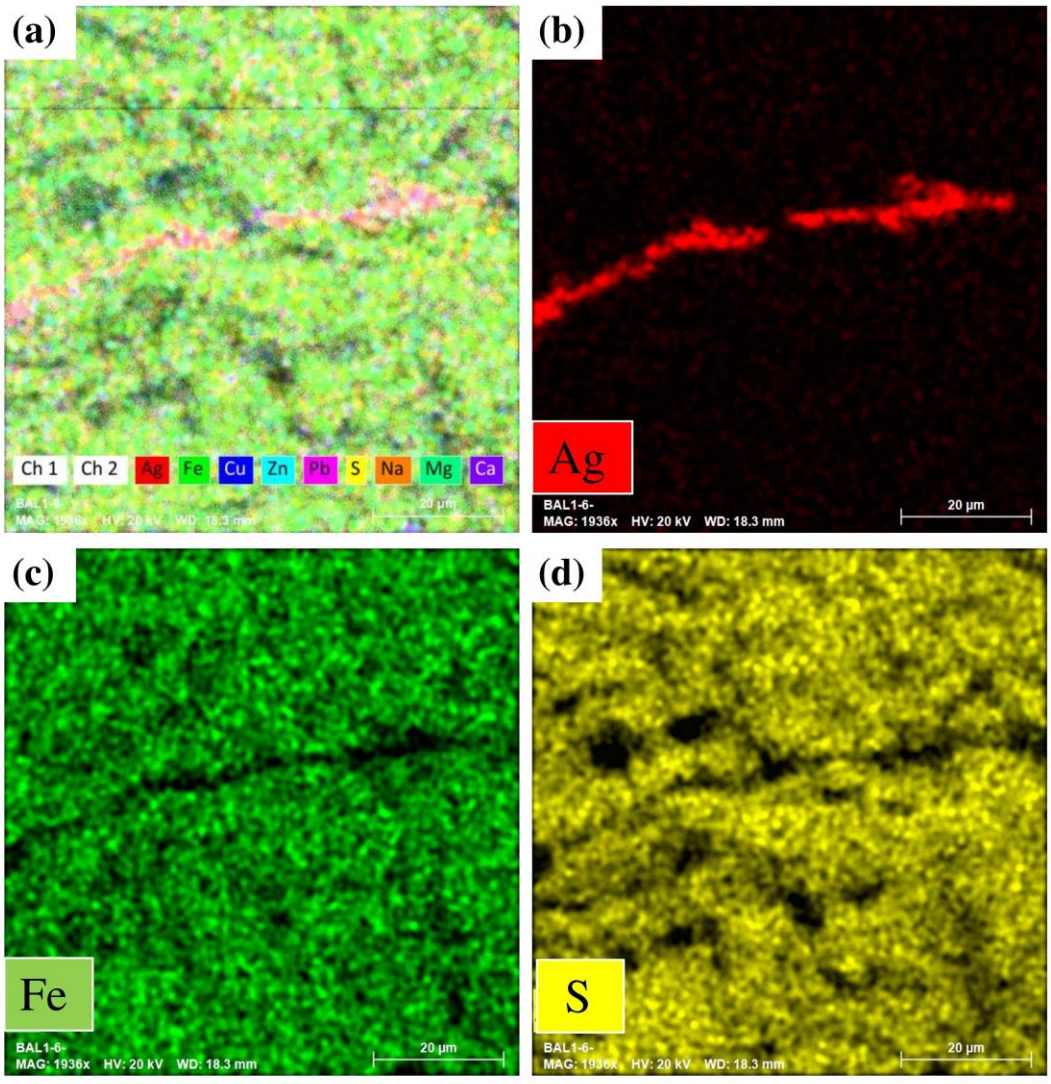

Figure 3. EDS elemental maps of acanthite vein showing that silver (Ag) and sulfur (S) are concentrated along a fracture-controlled vein, whereas, iron (Fe) is distributed in the surrounding host phase. **(a)** composite elemental distribution. Individual elemental map of **(b)** silver (Ag), **(c)** iron (Fe), and **(d)** sulfur (S).

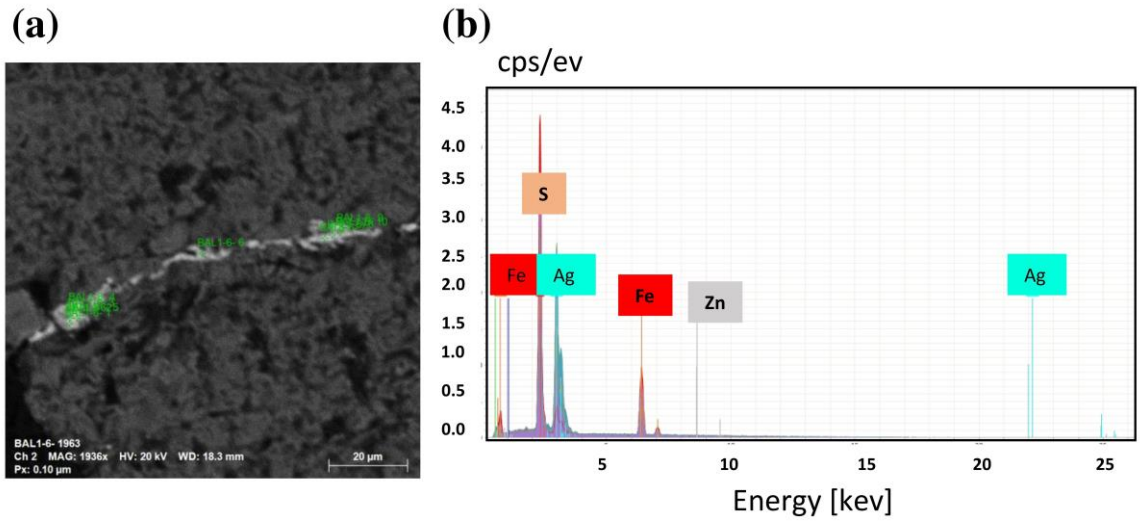

Figure 4. (a) Fracture-controlled acanthite mineralization with EDS analysis points. **(b)** EDS elemental concentration spectrum confirming acanthite, characterized by dominant Ag and S with minor trace-element contributions.

CONCLUSIONS

SEM and, EDS investigations of the Zawar deposit demonstrate that silver occurs as late-stage acanthite, developed as distinctive star-shaped aggregates along fractural sites within earlier-formed Py. The textural evidence for rapid quenching of Ag-bearing fluids against cooler sulfide surfaces, coupled with the confinement of acanthite to structurally controlled micro-openings, is fully consistent with the deposition from low-temperature basinal brines, characteristic of MVT systems (Awadh, 2018). EDS data confirm that these phases are dominantly Ag and S with minor Ca and Fe reflecting Ag_2S composition with only limited elemental substitution or inclusions of other sulfides. Together, the polymorph stability of Ag_2S, the microstructural setting of acanthite, and it's close association with Py and carbonate host rocks, indicate that silver enrichment at Zawar is genetically linked to the late stages of MVT-style hydrothermal activity.

Acknowledgements

We are thankful to Dr. Prakash Kumar, Director, CSIR-National Geophysical Research Institute (CSIR-NGRI), Hyderabad, for his constant encouragement, provision of research facilities, and permission to undertake this work. We are deeply indebted to Dr. EVSSK Babu for his kind supports and granting access to laboratory facilities. We would like to express our sincere thanks to Dr. Biswajit Mandal for his encouragement and valuable inputs related to this work. Thanks to Dr. A. Kasi Viswanadham of Vedanta Resources Limited for providing field guidance. We profoundly thank to Dr. O.P. Pandey, Chief Editor, for his valuable comments and suggestions to improve the quality of the manuscript. We also sincerely thank the two anonymous reviewers for their valuable and constructive comments, which significantly improved the quality of the manuscript. We also extend our appreciation to the authors of the studies cited herein and to the wider scientific community for their foundational contributions to this field.

Author credit statement

Sima Gorai: Conceptualization, data generation, methodology and writing original draft; Bulusu Sreenivas: Supervision, validation, review and editing; T Vijaya Kumar: Methodology and data acquisition.

Data availability

The data set generated and or analysed during the current study are available from the corresponding author on reasonable request.

Compliance with ethical standards

There is no conflict of interest associated with this publication and authors adhere to copyright norms.

REFERENCES

Awadh, S. M., 2018. Petrography and mineral chemistry of a newly discovered Ag and Cd ore minerals in the Zn-Pb-barite occurrence in Alanish area, Zakho, northern Iraq. Iraqui Bull of Geol. mining, 14(2), 97-108.

Deb, M., Thorpe, R. I., Cumming, G. L. and, Wagner, P. A., 1989. Age, source and stratigraphic implications of Pb isotope data for conformable, sediment-hosted, base metal deposits in the Proterozoic Aravalli-Delhi orogenic belt, northwestern India. Precam. Res., 43(1-2), 1-22.

Dill, H. G., 2010. Authigenic heavy minerals a clue to unravel supergene and hypogene alteration of marine and continental sediments of Triassic to Cretaceous age (SE Germany). Sediment. Geol., 228(1-2), 61-76.

Gorai, S., Rani, N., Kumar, T. V. and, Sreenivas, B., 2024. Integrated Remote Sensing and Petrographic Guide to Delineate the Hydrothermal Alteration Zones Along the Phyllites of the Main Zawar Fold, Rajasthan, India. J. Ind. Soc. Remote Sensing, 52(9), 1923-1936.

Gorai, S., Dalai, B., Kumar, T. V. and, Sreenivas, B., 2025a. Machine learning applications in trace element analysis: decoding the origin of galena in the Zawar Zn-Pb Deposit, India. Earth Sci. Informatics, 18(3), 1-19.

Gorai, S., Dalai, B., Vijaya Kumar, T. and, Sreenivas, B., 2025b. Integration of Machine Learning with In-Situ LA-ICP-MS Trace Element Analysis: Multi-Classification Approach Reveals the Hydrothermal Origin of Sphalerite in the Zawar Zn-Pb Deposit, Rajasthan, India. J. Geol. Soc. Ind, 101(8), 1235-1246.

Haldar, S. K., 2004. Deposits of Rajasthan, India. Sediment Hosted Lead-Zinc Sulphide Deposits, p. 264.

Indian Minerals Yearbook, 2023. Pp. 388 - 396.

Maghfouri, S. and, Choulet, F., 2021. Ore-forming processes, O–C isotopes geochemistry, and fluid inclusions in the Darreh-Zanjir fault control MVT-type Zn–Pb deposit: Iran. Arabian J. of Geosci., 14(20), 2083.

Misra, K. C., 2000. Mississippi Valley-Type (MVT) Zinc-Lead Deposits. In: Understanding Mineral Deposits (pp. 573-612). Dordrecht: Springer Netherlands.

Mookherjee, A., 1964. The geology of the Zawar lead-zinc mine, Rajasthan, India. Econ. Geol., 59(4), 656-677.

Mukherjee, A., and, Bhattacharya, H. N., 2021. Mixed siliciclastic–carbonate debrite–turbidite deposits in Paleoproterozoic Aravalli Supergroup, Zawar, Rajasthan, India: Implications on the Aravalli Basin evolution. J. Earth Syst. Sci., 130(3), 1-16.

Roy, A. B., 1995. Geometry and evolution of superposed folding in the Zawar lead-zinc mineralized belt, Rajasthan. Proc. Ind. Acad. Sci.-Earth Planet. Sci., 104(3), 349-37.

Sadovnikov, S. I., Gusev, A. I. and Rempel, A. A., 2015. An in situ high-temperature scanning electron microscopy study of acanthite–argentite phase transformation in nanocrystalline silver sulfide powder. Physical Chemistry Chemical. Phys., 17(32), 20495-20501.

Received on: 22-01-2026; Revised on 05-02-2026; Accepted on 09-02-2026

GUIDE FOR AUTHORS

The Journal of Indian Geophysical Union (JIGU), a SCI Journal published bimonthly by the Indian Geophysical Union (JIGU), is an inter disciplinary journal from India that publishes high-quality research in earth sciences with special emphasis on the topics pertaining to the Indian subcontinent and the surrounding Indian Ocean region. The journal covers several scientific disciplines related to the Earth sciences such as solid Earth Geophysics, geology and geochemistry, apart from marine, atmosphere space and planetary sciences. J-IGU welcomes contributions under the following categories :

*Research articles, short notes and students section reporting new findings, results, etc.

*Review articles providing comprehensive overview of a significant research field.

In addition, JIGU also welcomes short communications, after communications and report on scientific activity, book reviews, news and views, etc.

The manuscript should be submitted electronically as a single word format (.doc file) including the main text, figures, tables, and any other supplementary information along with the signed "Declaration Letter". The manuscript should be submitted by email (jigul1963@ gmail.com) to the Chief Editor.

After acceptance of the manuscript the corresponding author would be required to submit all source files (text and Tables in word format) and figure in high resolution standard (*.jpg, *.tiff, *.bmp) format. These files may be submitted to JIGU as a single *.zip file along with the "Copyright Transfer Statement".

IMPORTANT INFORMATION

Ethics in publishing; J-IGU is committed to ensuring ethics in publication and takes a serious view of plagiarism including self-plagiarism in manuscripts submitted to the journal, Authors are advised to ensure ethical values by submitting only their original work and due acknowledgement to the work of others used in the manuscript. Authors must also refrain from submitting the same manuscript to more than one journal concurrently, or publish the same piece of research work in more than one journal, which is unethical and unacceptable. Editor of JIGU is committed to make every reasonable effort to investigate any allegations of plagiarism brought to his attention, as well as instances that come up during the peer review process and has full authority to retract any plagiarized publication from the journal and take appropriate action against such authors if it is proven that such a misconduct was intentional.

Similarly, Editor and Reviewers are also expected to follow ethical norms of publishing by ensuring that they don't use any unpublished information, communicated to them for editorial or review purpose, in their own research without the explicit written consent of the author. They are also expected to keep manuscript' data/ observations/ any other information related to the peer review confidential to protect the interest of the authors. Reviewers should refrain from reviewing the manuscripts in which they have conflicts of interest resulting from competitive, collaborative, or other relationships or connections with any of the authors, companies, or institutions connected to the manuscript.

Conflict of interest

All authors are requested to disclose any actual or potential conflict of interest including any financial, personal or other relationships with other people or organizations within three years of beginning the submitted nor that could inappropriately influence, or be perceived to influence, their work.

Submission declaration

Submission of a manuscript implies that the work has not been published previously and it is not under consideration for publication elsewhere, and that if accepted it will not be published elsewhere in the same or any other form, in English or in any other language, without the written consent of the publishers. It also implies that the authors have taken necessary approval from the competent authority of the institute/organization where the work was carried out.

Copyright

After acceptance of the manuscript the corresponding author would be required to sign and submit the "Copyright Transfer Statement".

MANUSCRIPT PREPARATION

The corresponding author should be identified (include E-mail address, Phone/Mobile number). Full affiliation and postal address must be given for all co-authors.

Abstract:

An abstract of not more than 300 words must be included.

Text:

The manuscript should be structured to include a front page containing the title, Author(s) name, affiliation and address of the institute, where the work was carried out, and 5-to-6 Key words. Author(s) present address, if different from the above mentioned address, may be given in the footnote. The corresponding author should be identified with an asterisk and his/her email ID should be provided. This page should be followed by the main text consisting of Abstract, Introduction, Methods/ Techniques/ Area description, Results, Discussion, Conclusions, Acknowledgements, and References. Tables and Figures with captions should be inserted at the end of main text. It should not be inserted in the body of the text.

Figures/ Illustrations:

figures should be provided in camera-ready form, suitable for reproduction (which may include reduction) without retouching. Figures in high-resolution (at least 300 dpi) standard formats (*.jpg, * tiff, *.bmp) are acceptable. Figures should be numbered according to their sequence in the text. References should be made in the text to each figure. Each figure should have a suitable caption.

Tables:

Authors should take note of the limitations set by the size and layout of the journal. Table should not exceed the printed area of the page. They should be typed on separate sheets and details about the tables should be given in the text. Heading should be brief. Large tables should be avoided and may be provided as supplementary information, if required.

Equations:

Equations should be numbered sequentially with Arabic numerals and cited in the text. Subscripts and Superscripts should be set off clearly.

Equation writing software that presents each equation as an object in MS Word will be accepted. Style and convention adopted for the equations should be uniform throughout the paper.

References:

All references to publications cited in the main text should be presented as a list of references in order following the text and all references in the list must be cited in the text. References should be arranged chronologically, in the text. The list of references should be arranged alphabetically at the end of the paper.

References should be given in the following form:

Kaila, K.L., Reddy PR., Mall D.M., Venkateswarlu, N., Krishna V.G. and Prasad, A.S.S.S.R.S., 1992, Crustal structure of the west Bengal el eon deep seismic sounding investigations. Geophys. J. Int., 1,45-66.

REVIEW PROCESS:

All manuscripts submitted to the journal are peer-reviewed. It is advisable to send the contact details of 4 potential reviewers along with the manuscript to expedite the review process. Editor has the option to select reviewers from the list or choose different reviewers. The review process usually takes about 3 months. All enquiries regarding the manuscript may be addressed to the Chief Editor.

GALLEY PROOF:

Technical editing of manuscripts is performed by the editorial board. The author is asked to check the galley proof for typographical errors and to answer queries from the editor. Authors are requested to return the corrected proof within two days of its receipt to ensure uninterrupted proceedings The editor will not accept new material in proof unless permission from the editorial board has been obtained for the addition of a "note added in proof". Authors are liable to be charged for excessive alterations to galley proof.

PUBLICATION CHARGES:

There are no page charges for publication. The corresponding author will receive a soft copy (pdf format) of his/her published article. Should the author desire to purchase reprints of his/her publication, he/she must send the duly signed Reprint Order Form (accompanies the galley proof and contains price details) along with the corrected galley proof to the Editor. The reprint charges must be paid within one month of sending the Reprint Order Form.

Any payment related to printing or purchase of reprints should be made in the form of a Demand Draft in the name of Treasurer, Indian Geophysical Union, payable at Hyderabad.

You may download the pdf file from:
http://iguonline.in/journal/instructions.php